



Title	Control of Formation and Magnetic Domain Structures in Selectively-Grown MnAs Nanostructures
Author(s)	堀口, 竜麻
Citation	北海道大学. 博士(工学) 甲第14589号
Issue Date	2021-03-25
DOI	10.14943/doctoral.k14589
Doc URL	http://hdl.handle.net/2115/81591
Type	theses (doctoral)
File Information	Ryoma_Horiguchi.pdf



[Instructions for use](#)

Doctoral Dissertation

博士論文

Control of Formation and Magnetic Domain Structures in Selectively-Grown MnAs Nanostructures

(選択成長した MnAs ナノ構造の形成及び磁区構造制御に関する研究)

Graduate School of Information Science and Technology,

Hokkaido University

北海道大学大学院情報科学研究科

Ryoma Horiguchi

堀口 竜麻



© 2021 Ryoma Horiguchi

A dissertation submitted in partial fulfillment
of the requirements for the degree of Doctor of
Philosophy (Engineering)
in Hokkaido University, February, 2021.

Dissertation Supervisor
Associate Professor Shinjiro Hara

Acknowledgements

This dissertation describes a part of research work carried out at Research Center for Integrated Quantum Electronics (RCIQE), Hokkaido University, under the supervision of Prof. Shinjiro Hara, while I was graduate student at the Graduate School of Information Science Technology, Hokkaido University.

I especially wish to express my sincere appreciation to Supervisor, Prof. Shinjiro Hara. This work would never be accomplished without his invaluable support, guidance, and encouragement. I am greatly happy to study and research for six years under his supervision.

I would like to express my sincere thanks to Prof. Junichi Motohisa, Prof. Tamotsu Hashizume and Prof. Tetsuya Uemura for their continual support and insightful comments.

I would like to express my appreciation to Prof. Takashi Fukui, Prof. Eiichi Sano, Prof. Seiya Kasai, Prof. Masayuki Ikebe, Prof. Masamichi Akazawa, Prof. Taketomo Sato, and Prof. Katsuhiro Tomioka, for their encouragement and fruitful discussions.

I would like to say thanks to the member of our research group, Dr. Shinya Sakita, Dr. Ryutaro Kodaira, Mr. Kyohei Kabamoto, Mr. Yoshito. Sakakibara, Mr. Tetsuro Kadowaki, Mr. Masaya Iida, Mr. Yuki Kitazawa, Mr. Kozaburo Suzuki, Mr. Keigo Teramoto, Mr. Daiki Goto, Mr. Wei Dai, Mr. Hiroaki Kato and Mr. Kohei Morita for their technical supports, valuable discussions and encouragement.

I wish to say thanks for RCIQE researchers and students, Dr. Zenji Yatabe, Dr. Roman Stoklas, Dr. Maciek Matys, Dr. Masaki Sato, Dr. Xiang Yin, Dr. Ryota Kuroda, Dr. Fumiya Ishizaka, Dr. Yusuke Kumazaki, Dr. Kenya Nishiguchi, Mr. Kentaro Sasaki, Mr. Kohei Kamada, Mr. Kento Shirata, Mr. Muyi Chen, Mr. Yoshihiro Hiraya, Mr. Ryo Wakamiya, Mr. Jyoji Ohira, Mr. Takehiro Kawauchi, Mr. Taro Itatsu, Mr. Tomohide Yoshikawa, Mr. Akihito Sonoda, Mr. Shoma Okamoto, Mr. Yuki Inden, Ms. Sayaka Ohmi, Mr. Hirofumi Kida, Mr. Masaaki Edamoto, Mr. Naoto Tamaki, Mr. Atsushi Seino, Mr. Takuya Miyajima, Mr. Yukinori Wakita, Mr. Shun Takayashiki, Mr. Shota Kaneki, Mr. Shota Toiya, Mr. Keisuke Ito, Mr. Kenta Saito, Mr. Koki Abe, Mr. Satoru Matsumoto, Mr. Dai Hasegawa, Mr. Naoshige Yokota, Mr. Taito Hasezaki, Mr. Shota Hiramatsu, Mr. Kohei Chiba, Mr. Akinobu Yoshida, Mr. Yuji Ando, Mr. Tatsuya Oyobiki, Mr. Katsuma Shimizu, Mr. Keisuke Uemura, Mr. Kazuki Inada, Mr. Masachika Toguchi, Mr. Shohei Kitajima, Mr. Kei Uetake, Mr. Masahiro Sasaki, Mr. Yusuke Minami, Mr. Yuya Yamamoto, Mr. Kim Minchan, Mr. Shota Sasaki, Mr. Kentaro Takeda, Mr. Naoki Suefuji, Mr. Koichi Tajima, Mr. Yuto Kojima, Mr. Ryo Kamoshida, Mr. Kazuki Isobe, Mr. Michihito Shimauchi, Mr. Tomoya Akamatsu, Mr. Hironori Gamo and I also express thank to the all RCIQE students for their friendship.

I would like to extend my deepest gratitude to Mr. Kenji Takada, Mr. Kiyotake Nagakura, Ms. Mizuho Tanaka, and Ms. Chieko Akiyama for their businesslike supports and encouragements.

I would like to express my sincere thanks to Prof. Peter J. Klar, Dr. Matthias T. Elm, Dr. Martin. Fischer, Dr. Lars Ostheim, Mr. Fabian Alexander, and Dr. Patrick Uredat for invaluable discussions, support, encouragement and their kind hospitality during my stay in Gießen,

Germany. I had a precious time with them, and I really like German food and culture. I am so thankful to have met them.

Finally, I am particularly grateful to my parents and grandparents, Yasuhiro Horiguchi, Shigeko Horiguchi, Benishi Horiguchi, and Masako Horiguchi who have always provided heartfelt support and encouragement. Thank you from the bottom of my heart.

February 2021

Ryoma Horiguchi

Table of Contents

Acknowledgements	i
Contents	iv
List of Figures	viii
List of Tables	xvii

Chapter 1

Introduction	1
1.1 Background	1
1.1.1 Semiconductor spintronics	1
1.1.2 Manganese Arsenide.....	2
1.2 Objective	5
1.3 Outline of this thesis	5
Bibliography	8

Chapter 2

Magnetic domain structures in ferromagnetic materials	13
2.1 Introduction	13
2.2 Magnetic domain structure	13
2.3 Magnetocrystalline anisotropy	16
2.4 Shape anisotropy	17

2.5 Magnetic tunnel junction	19
Bibliography	20

Chapter 3

Experimental Techniques	22
3.1 Introduction	22
3.2 Overview of SA-MOVPE	22
3.3 Growth system for MOVPE	23
3.4 Preparation of substrates for MOVPE growth	25
3.5 Characterizations	26
3.5.1 Scanning electron microscopy	26
3.5.2 Magnetic force microscopy	30
Bibliography	31

Chapter 4

Selective-area growth of ferromagnetic MnAs nanodisks on Si (111) substrates covered with multiple types of dielectric masks	32
4.1 Introduction	33
4.2 Experimental procedure	34
4.3 Results and discussion	37
4.4 Conclusions	46

Bibliography	47
--------------------	----

Chapter 5

Characterization of magnetic domain structure and domain wall analysis in MnAs nanodisks selectively-grown on Si (111) substrates	52
---	----

5.1 Introduction	53
------------------------	----

5.2 Experimental procedure	55
----------------------------------	----

5.3 Results and discussion	56
----------------------------------	----

5.3.1 Structural characterization of MnAs nanodisks	56
---	----

5.3.2 Characterization of magnetic domain and domain wall analysis of MnAs nanodisks under as-grown condition	58
---	----

5.3.3 Applied magnetic field dependence of magnetic domain structure and magnetization switching of MnAs nanodisks	65
--	----

5.4 Conclusions	75
-----------------------	----

Bibliography	77
--------------------	----

Chapter 6

Structural and magnetic domain characterization of lateral MnAs/AlGaAs nanowires selectively-grown on GaAs (111)B substrates	85
--	----

6.1 Introduction	85
------------------------	----

6.2 Experimental procedure	87
6.3 Results and discussion	88
6.3.1 Structural characterization of lateral MnAs/AlGaAs NWs by BSE imaging	88
6.3.2 Magnetization switching and magnetic domain analyses by MFM imaging	91
6.4 Conclusions	98
Bibliography	99
 Chapter 7	
Conclusion	105
 List of Publications/Conferences/Awards	108

List of Figures

Figure 1-1	Schematic illustration of spin-based FET structure: (a) spin-FET, (b) spin-MOSFET, and (c) pseudo spin-MOSFET.	1
Figure 1-2	The crystal structure of MnAs: (a) hexagonal NiAs-type structure, (b) orthorhombic MnP-type structure, and (c) zinc-blende type structure.	3
Figure 2-1	Schematic illustration of magnetic domain structures and domain walls: (a) Closure magnetic domain, (b) Bloch wall, and (c) Néel wall.	14
Figure 2-2	The energy of a uniaxial magnetic anisotropy required for the magnetization to tilt from <11-20> to <0001> orientation. The angle of $\theta = 0$ degree is corresponding to the <11-20> orientation of hexagonal MnAs.	17
Figure 2-3	The demagnetizing factor for (a) spherical body, (b) infinity expanded thin layer in x-y plane, and (c) infinity elongated wire.	18
Figure 2-4	Schematic illustration of MTJ structure: (a) When the magnetization in free layer is parallel to that in fixed layer, MTJ structure has a relatively low resistance. On the other hand, (b) when the magnetization of free layer is anti-parallel to that in fixed layer, MTJ structure has a relatively high resistance.	19
Figure 3-1	Schematic illustration of catalyst-free SA-MOVPE growth. (a) SiO ₂ thin film	

is deposited on the GaAs (111)B substrates. (b) Initial rectangular opening is fabricated in the SiO ₂ thin film by lithography and etching. (c) Nucleation occurs on the substrate surface within the mask opening region, and then lateral MnAs NW begins to grow.	23
Figure 3-2 Schematic illustration of growth system for MOVPE.	24
Figure 3-3 Schematic illustration of bubbler. When the MO source is provided, the red (blue) valves are opened (closed).	25
Figure 3-4 Schematic illustration of SEM systems. SEM system consists of an EB gun, condenser lenses, apertures, polarized coils, an objective lens and a specimen chamber.	27
Figure 3-5 Measurement principle of MFM observation.	29
Figure 3-6 Shift of phase curve by stray magnetic fields from specimen.	30
Figure 4-1 Schematic illustrations of mask patterns (I) and (II) for the selective-area growth: (a) SiO ₂ or SiON films outside 100 × 100 μm ² square regions with periodical circular openings were removed, which are referred to as “mask pattern (I)”, and (b) SiO ₂ or SiON films were removed only for the periodical circular openings within the 100 × 100 μm ² square regions, which are referred to as “mask pattern (II)”.	35

- Figure 4-2 (a) Secondary electron image of MnAs directly grown on Si (111) substrates with the mask pattern (I) of SiO₂. (b) Bird's-eye view of a secondary electron image by SEM and cross-sectional TEM image of AlGaAs NP buffers with a high degree of uniformity grown on Si (111) substrates with the mask pattern (I) of SiO₂ at the growth temperature of 800°C for 10 min. The layer thickness from the mask surface and the width from the mask edge were estimated to be 125 and 55 nm, respectively 36
- Figure 4-3 Bird's-eye view of a secondary electron image by SEM: (a) overall and (b) highly-magnified views, and (c) a cross-sectional TEM image of MnAs/AlGaAs NDs grown on Si (111) substrate with the mask pattern (I) of SiO₂. The growth temperature and time were 800°C and 10 min for the AlGaAs and MnAs growth, respectively. Unintentional growth of MnSi alloy in Si substrates and MnAs alloy with approximately 17% of Si atoms on NDs was observed, as shown by the circle "a" of broken line and the circle "b" of dot-dash line in (b) and (c), respectively. 39
- Figure 4-4 (a) Bird's-eye view of a secondary electron image by SEM and (b) a cross-sectional TEM image of MnAs/AlGaAs NDs grown on Si (111) substrates with the mask pattern (II) of SiON. The growth temperature and time were 800°C and 20 sec for the AlGaAs growth and 1 min for the MnAs growth, respectively. The tilted ND was due to the tilted (111) plane of Si substrates. It was confirmed that the (111) planes of Si substrates were parallel to the

(0001) planes of hexagonal NiAs-type MnAs. The inset of (b) shows a lattice image near the interface between MnAs layer and AlGaAs layer. The dislocations were observed in the circles of broken line, and the mean period of dislocations was approximately 3.6 nm.41

Figure 4-5 Acceleration voltage dependence of BSE images of MnAs/AlGaAs NDs grown on Si (111) substrates with the mask pattern (II) of SiO_2 : (a) 0.5 and (b) 2.5 kV. In (a), relatively dark contrasts in ND-A and brighter contrasts in the NC-B than the contrast of ND-A were observed. The different level of contrasts brighter than those of Si substrates near the NDs was observed, as in the circle of broken line in (b). These brighter contrasts were due to MnSi alloys.42

Figure 5-1 Acceleration voltage dependence of BSE images of MnAs NDs on AlGaAs NP buffers: (a) 0.5 and (b) 1.5 kV. In (a), a relatively bright image contrast of ND-A and an image contrast of ND-B darker than the one of ND-A are observed. In (b), almost no significant difference in the image contrasts between ND-A and ND-B is observed. (c) MFM image of the corresponding MnAs NDs. The MFM observations were carried out at room temperature without any application of an external magnetic field. Most of the MnAs NDs show a spontaneous magnetization. A single magnetic domain is observed in ND-B, and multiple magnetic domains are observed in ND-C and ND-D. The white arrows in (c) indicate the directions of the magnetic moments (\mathbf{m}) in the NDs. No well-defined contrast is observed in the MFM image of ND-

E.....	57	
Figure 5-2	Size dependence of magnetic domain structures of MnAs NDs. (a) The two-dimensional distributions of single and multiple magnetic domains as a function of area and an aspect ratio of MnAs NDs. The aspect ratios were defined as the ratios of the longest length of <11-20> direction divided by the shortest length of <1-100> direction of MnAs NDs. (b) The ratio of domain structures as a function of area of MnAs NDs. The number of data is 100. Single magnetic domain structures were mainly observed in the NDs with $4 \times 10^4 \text{ nm}^2$ or less, and multiple magnetic domain structures were observed in the NDs with $6 \times 10^4 \text{ nm}^2$ or more.	60
Figure 5-3	Schematic illustrations of the magnetic domain structures and the domain walls assumed by the contrasts of MFM images in (a) ND-D and (b) ND-C. Bloch and Néel wall widths were estimated to be approximately 26 nm for ND-D and 35 nm for ND-C, respectively, by the image contrasts and the intensity gradient of contrasts in the MFM images of (c) ND-D and (d) ND-C.	62
Figure 5-4	Calculated wall energy density per unit area of domain walls as a function of the MnAs thickness. The Bloch wall energy was equal to the Néel wall energy at the ND thickness of approximately 22 nm, which was nearly consistent with the thickness of 20 nm roughly estimated from the acceleration voltage dependence of BSE images of MnAs NDs.	65

Figure 5-5	Applied external magnetic field, \mathbf{B} , dependence of the ratio, or percentage, of a single magnetic domain observed in MnAs NDs. The open triangle and closed triangles are for the NDs with an area of $4 \times 10^4 \text{ nm}^2$ or smaller, i.e., Group S, and the open square and closed squares for the NDs with an area of $4 \times 10^4 \text{ nm}^2$ or larger, i.e., Group L. The solid triangles and squares indicate the results obtained for the sweep direction of the \mathbf{B} applied from 0 to -4.0 kG, and the open triangles and squares indicate those from -4.0 to +4.0 kG. The dashed lines are a guide to the eye. The data on the dotted line are for a spontaneous magnetization under as-grown condition. The inset shows a BSE image of a MnAs ND on an AlGaAs NP buffer. The white two-head arrow in the inset indicates the directions of an applied magnetic fields, \mathbf{B} . The ratio of a single magnetic domain is markedly minimized at $\mathbf{B} = -1.5 \text{ kG}$ in the case of Group S.....	66
------------	--	----

Figure 5-6	Applied external magnetic field, \mathbf{B} , dependence of magnetic domain structures in MnAs NDs. The change from a single magnetic domain to a multiple magnetic domain in the NDs at (a) $\mathbf{B} = -1.0$ and (b) -0.5 kG is observed. Insets in (a) and (b) show the magnetization directions under as-grown condition and the definition of the aspect ratio. The aspect ratio of NDs is defined as the ratio of the length parallel to the magnetization direction divided by that perpendicular to the magnetization direction of the NDs, i.e., L/W , as illustrated in the insets. The images also show the aspect ratio dependence of magnetic domains in the NDs. ND-F has low aspect ratio of 1.03, i.e., a small
------------	---

shape anisotropy, and the magnetization in opposite direction to the B direction. ND-B has a relatively high aspect ratio of 1.14, i.e., a larger shape anisotropy than that of ND-F, and the magnetization with a component in the same direction as the B direction. ND-F and ND-B are categorized in Group L. No dependence of magnetic domain switching on the aspect ratio of the NDs has been observed.	68
Figure 5-7 Applied magnetic field, B , dependence of an angle of a magnetization direction in MnAs NDs at the B applied from +0.5 to +2.0 kG for both Group S and Group L. The dotted line represents the boundary between Group S and Group L. The inset shows the schematic definition of an angle of magnetization direction, θ . The angle of $\theta = 0$ degree is corresponding to the <11-20> orientation of MnAs NDs.	72
Figure 5-8 The radar charts of the number of NDs in terms of the angle of magnetization directions in steps of 30 degrees, which are summarized for B = (a) 0 (i.e., as-grown condition), (b) -4.0, (c) +0.5, and (d) +1.5 kG. The angle of $\theta = 0$ degree is corresponding to the <11-20> orientation of MnAs NDs. At $B = +1.5$ kG, the magnetization switching is observed in some of the NDs, indicating that the mean coercive force is estimated approximately to be 1.5 kOe.	73
Figure 6-1 Acceleration voltage dependence of BSE images of lateral MnAs NWs: (a) 1.0 and (b) 2.0 kV. In (a), two relatively dark regions, i.e., NW-A and NW-C,	

are observed, and a brighter area, i.e., gap region B, than the two dark regions is confirmed between the two dark regions of NWs. In (b), almost no significant brightness difference among NW-A, gap region B, and NW-C is observed. The crystallographic relationship between a GaAs (111)B substrate and the lateral MnAs NWs is depicted below the BSE images.89

Figure 6-2 Bird's-eye view of secondary electron image by SEM and cross-sectional illustration of MnAs NWs with the measured length, height, and width of the NWs. The angle between top and sidewall facets was estimated to be 60 degrees.....90

Figure 6-3 MFM images after the application of the external magnetic field of 2.0 kG in the directions (a) the same as and (b) opposite to the observed magnetization directions of the MnAs NWs at room temperature. In (a) and (b), the thick and white arrows represent the applied magnetic field directions, and the magnetization directions are oriented from bright to dark regions in the images, as indicated by the long and short thin white arrows. (c) Cross-sectional line profile of the MnAs NWs observed by AFM.93

Figure 6-4 MFM images after the application of 4.0 kG in the direction opposite to the observed magnetization directions of NWs at room temperature: (a) Whole image and (b) highly magnified image for the sudden changes in the contrasts from bright to dark at one of the ends of NW-C. In (a), the thick and white arrow represents the applied magnetic field direction, and the magnetization

directions are indicated by long and short thin white arrows. (c) Possible explanation for the magnetization switching of MFM tips themselves during the observations at one of the ends of NW-A and NW-C under the applied magnetic fields of 3.0 kG or more.94

Figure 6-5 Schematic illustration of the simple magnetic dipole model, which is used to estimate the effective stray magnetic fields along the z-axis from the NW-A and NW-C at the tip height h for the MFM observations of the NWs.95

List of Tables

Table 3-1	The summary of the relationship of force gradient, shift direction of phase curve, and change in phase, ϕ , and image contrast.	30
Table 4-1	The summary of characterization results for the key issues A and B in the selective-area growth of MnAs NDs using the mask patterns (I) and (II) of SiO ₂ and SiON.	44

Chapter 1

Introduction

1.1 Background

1.1.1 Semiconductor spintronics

Recently, device performance has been improved by the miniaturization of electronic devices in conventional Si complementary metal-oxide semiconductor (CMOS)-based integrated circuits [1, 2]. However, because of the physical limitation on device dimensions and the increase of power consumption, a realization of electronic devices based on new functions and operating principles is required. A spin-based field-effect transistor (FET) has been one of the most promising candidates among such newly-functionalized devices, and is expected to have low power consumption and high-speed operation [2–4]. A spin-FET were proposed by S. Datta and B. Das in 1990 [5], and consists of semiconductor two-dimensional electron gas (2DEG) channel with a gate electrode and the ferromagnetic electrodes as shown in Fig. 1-1(a). In such spin-FET, the spin-polarized electrons injected from the ferromagnetic source electrode start to rotate because an effective magnetic field is created by the spin-orbit interaction in the 2DEG channel.

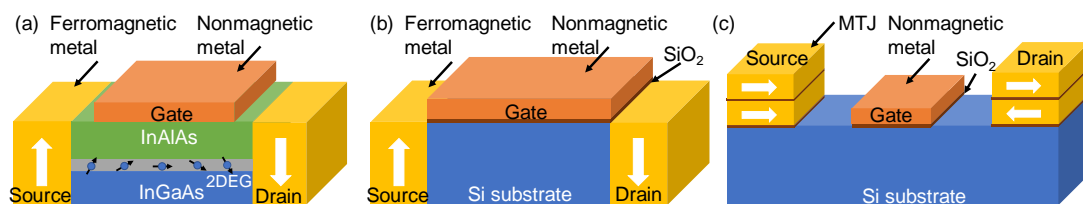


Figure 1-1. Schematic illustration of general spin-based FET structure: (a) spin-FET, (b) spin-MOSFET, and (c) pseudo spin-MOSFET.

The spin precession angle can be controlled by the gate voltage since the spin-orbit interaction is modified by the gate voltage. If the spin orientation in the 2DEG channel is aligned to the ferromagnetic drain electrode, the electrons can flow into the ferromagnetic drain electrode. On the other hand, when the spin orientation is flipped in the 2DEG, the electrons cannot enter the drain electrode. Therefore, the materials with a large spin-orbit interaction such as GaAs and InAs are used for 2DEG channel in spin-FET. As another type of spin-based FET, a spin-MOSFET was proposed by S. Sugahara and M. Tanaka in 2004 [6] and demonstrated by some researchers [7, 8] at room temperature. The general structure of spin-MOSFET consists of a Si-MOSFET and ferromagnetic source and drain electrodes as shown in Fig. 1-1(b). In the case of spin-MOSFET, the resistance can be controlled by the magnetization configuration in source and drain electrodes. Since the spin-MOSFET requires no spin precession of spin-polarized electrons in the channel, the materials with a small spin-orbit interaction such as Si and Ge are used for the channel materials. In addition, magnetic tunnel junctions (MTJs) are used for source and drain electrodes in spin-MOSFET. Such spin-MOSFET are called pseudo-spin-MOSFET or spin-transfer-torque MOSFET (STS-MOSFET) and demonstrated by some researchers [9, 10]. Since the resistance of spin-based FET can be controlled by the magnetization configuration in source and drain electrodes, the control of magnetic domain structure and the magnetization switching are much necessary.

1.1.2 Manganese arsenide

MnAs thin films and nanostructures had grown on III-V compound semiconducting substrates by epitaxial growth such as molecular beam epitaxy (MBE) [11–13] or selective-area

metal-organic vapor phase epitaxy (SA-MOVPE) [14–20]. The crystal structure of such MnAs thin films and nanostructures exhibiting ferromagnetism almost have a hexagonal NiAs-type structure as shown in Fig. 1-2(a). As described in Sec. 2-3, NiAs-type MnAs has a uniaxial magnetic anisotropy along c-axis and six-fold magnetic anisotropy in c-plane. The saturation magnetization of NiAs-type MnAs is $3.4 \mu_B/\text{Mn}$ under the magnetic field of 5 T [21, 22]. In addition, A MnAs bulk crystal shows a first-order structural phase transition between orthorhombic MnAs shown in Fig. 1-2(b) and NiAs-type MnAs at temperatures between 317 and 319 K, i.e., the Curie-temperature of NiAs-type MnAs is 317 to 319 K [23, 24]. In the case of thin films with the thickness of 60 nm, the phase coexistence of NiAs-type MnAs and MnP-type MnAs was observed at the temperature from 283 to 313 K. In addition, the enhancement of Curie-temperature up to 340 K was observed in the case of hexagonal NiAs-type MnAs nanostructures grown on InGaAs layers on InP (111)B substrates, possibly owing to the incorporation of a small fraction of Ga atoms into the nanostructures [18].

A zinc-blende (ZB)-type MnAs as shown in Fig. 1-2(c) highly expected to realize nanospintronic devices such as magnetic tunnel junction and spin transistor with high ON/OFF

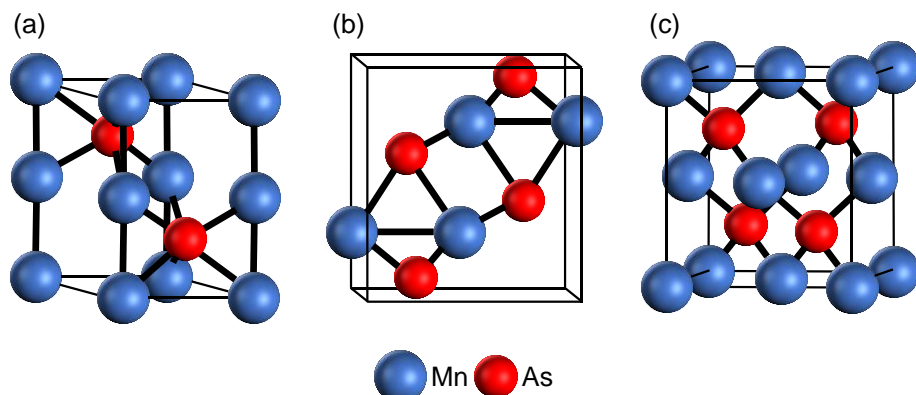


Figure 1-2. The crystal structure of MnAs: (a) hexagonal NiAs-type structure, (b) orthorhombic MnP-type structure, and (c) zinc-blende type structure.

ratio, since a ZB-type MnAs was predicted to be half-metallic from first principle calculation, i.e., spin polarization is 100% at fermi energy [25]. In addition, the Curie-temperature and saturation magnetization of a ZB-type MnAs is much higher than that with NiAs-type structure, and approximately to 350 K and $4.0 \mu_B/\text{Mn}$, respectively [26]. The fabrication of ZB-type MnAs is difficult since the NiAs-type structure is thermodynamically stable, while ZB-type structure is thermodynamically unstable [27, 28]. In 2002, MnAs nanodots with ZB-type structure are grown on sulfur-passivated GaAs (001) substrates by MBE [29]. In addition, ZB-type MnAs nanoclusters were formed in GaAs thin films by annealing (Mn, Ga)As diluted materials grown on GaAs (001) substrates using MBE method in same in the same year [30]. And then, ZB-type MnAs thin films are grown on GaAs (001) substrates after InAs buffer layer growth by MBE in 2005 [31].

Among the MTJs in combination with semiconducting materials, intensive studies on the MTJ structures using MnAs and III-V compound semiconductors have been reported [32, 33]. A huge magnetoresistance up to 100,000% has been demonstrated in the MTJs with granular GaAs:MnAs hybrid nanomaterials system consisting of ferromagnetic MnAs nanoclusters embedded in semiconducting GaAs layers [33]. Such a MTJ structure has been mainly fabricated by conventional top-down-type microfabrication technologies. However, in the fabrication of such devices in nanometer scale, these conventional approaches may possibly result in deterioration in device performance owing to process-induced damages and a relatively poor size-uniformity.

1.2 Objective

To solve possible problems, we have developed a bottom-up-type fabrication method, which is based on selective-area MOVPE (SA-MOVPE), of ferromagnetic MnAs nanostructures on semiconducting GaAs (111)B and Si (111) substrates [14–20]. This technique enables us to control the size, density, position, and shape of nanostructures without any process-induced damage and contamination for the fabrication of nanospintronic devices such as STS-MOSFET using MTJs as the source and drain electrodes. For example, the vertical-type MTJs are fabricated by lithography processes after the deposition of oxide interlayers such as MgO and Al₂O₃, and ferromagnetic thin films on the MnAs NDs grown by our SA-MOVPE. For the lateral-type MTJs, we believe that the use of elongated MnAs ND composites is promising, as demonstrated on GaAs (111)B substrates. In general, the magnetic domain structure depends on the size and shape of the ferromagnetic nanomaterials and nanostructures. In this study, therefore, we characterized the magnetic domain structure characterization of MnAs nanodisks and nanowires to control the magnetic properties such as coercive force and magnetic domain structure by tuned the size and shape of the MnAs nanostructure for application of spintronics devices.

1.3 Outline of this thesis

This thesis describes the structural and magnetic domain structure characterization of MnAs NDs and lateral NWs selectively grown on Si (111) or GaAs (111)B substrates after AlGaAs layer growth for controlling the magnetic properties such as coercive force and magnetic domain structure by tuned the size and shape of the MnAs nanostructure for application of

spintronics devices. This thesis is divided into 7 chapters.

In chapter 2, the magnetic domain structure in ferromagnetic materials is described. In addition, magnetocrystalline anisotropy and shape magnetic anisotropy are explained.

In chapter 3, the principle of our MOVPE systems, which is utilized to grow the MnAs nanostructures in this study, are explained. In addition, the preparation of substrates for nanostructure growth are described. Finally, the characterization methods and equipment used in this study are also introduced.

In chapter 4, growth and structural characterizations of ferromagnetic MnAs ND after the AlGaAs nanopillar (NP) buffer growth on Si (111) substrates using multiple types of mask materials and designs is described. The results of structural characterizations show that two key issues, which are the unintentional growth of MnSi alloy in Si substrates and MnAs alloy with approximately 17% of Si atoms on NDs, are typically observed in the case of Si substrates with SiO_2 mask pattern removing the SiO_2 outside $100 \times 100 \mu\text{m}^2$ square regions with periodical circular openings.

In chapter 5, characterization of magnetic domain structure and magnetization switching in ferromagnetic MnAs NDs by magnetic force microscopy at room temperature without the application of an external magnetic field are described. A spontaneous magnetization is observed in most of MnAs NDs, and the direction of magnetization is parallel to <11-20> orientations of MnAs NDs, i.e., the easy magnetization axis of hexagonal NiAs-type MnAs. A single domain is predominant in the MnAs NDs with an area of approximately $4 \times 10^4 \text{ nm}^2$ or less. In addition, the

magnetization switching are observed after application of applied magnetic fields of 1.5 kGauss.

In chapter 6, structural and magnetic domain characterization of lateral MnAs/AlGaAs NWs are described. The lateral MnAs nanowires observed by backscattered and secondary electron microscopies have a high aspect ratio and well-defined crystal facets. The external magnetic field dependence in magnetic force microscopy observations of the lateral nanowires reveals that single and multiple magnetic domains were formed in the lateral nanowires.

Bibliography

- [1] G. E. Moore, Cramming more components onto integrated circuits, *Electronics* **38**, 114 (1965).
- [2] International Technology Roadmap for Semiconductors (ITRS) 2.0 (2015 Edition), Executive Report
- [3] H. Ohno, Making nonmagnetic semiconductors ferromagnetic, *Science* **281**, 951 (1998).
- [4] B. T. Jonker, Progress toward electrical injection of spin-polarized electrons into semiconductors, *Proc. IEEE* **91**, 727 (2003).
- [5] S. Datta and B. Das, Electronic analog of the electro-optic modulator, *Appl. Phys. Lett.* **56**, 665 (1990).
- [6] S. Sugahara, M. Tanaka, A spin metal–oxide–semiconductor field-effect transistor using half-metallic-ferromagnet contacts for the source and drain, *Appl. Phys. Lett.* **84**, 2307 (2004).
- [7] T. Sasaki, Y. Ando, M. Kameno, T. Tahara, H. Koike, T. Oikawa, T. Suzuki, and M. Shiraishi, Spin Transport in Nondegenerate Si with a Spin MOSFET Structure at Room Temperature, *Phys. Rev. Appl.* **2**, 034005 (2014).

-
- [8] T. Tahara, H. Koike, M. Kameno, T. Sasaki, Y. Ando, K. Tanaka, S. Miwa, Y. Suzuki, and M. Shiraishi, Room-temperature operation of Si spin MOSFET with high on/off spin signal ratio, *Appl. Phys. Express* **8**, 113004 (2015).
- [9] Y. Shuto, R. Nakane, W. Wang, H. Sukegawa, S. Yamamoto, M. Tanaka, K. Inomata, and S. Sugahara, A New Spin-Functional Metal–Oxide–Semiconductor Field-Effect Transistor Based on Magnetic Tunnel Junction Technology: Pseudo-Spin-MOSFET, *Appl. Phys. Express* **3**, 013003 (2010).
- [10] Y. Saito, T. Inokuchi, M. Ishikawa, H. Sugiyama, T. Marukame, and T. Tanamoto, Spin-based MOSFET and its applications, *J. Electrochem. Soc.* **158**, H1068 (2011).
- [11] F. Schippan, G. Behme, L. Daweritz, and K. H. Ploog, Magnetic structure of epitaxially grown on GaAs(001), *J. Appl. Phys.* **88**, 2766 (2000).
- [12] L. B. Steren and J. Milano, V. Garcia, M. Marangolo, M. Eddrief, and V. H. Etgens, Magnetization reversal and anomalous dependence of the coercive field with temperature in MnAs epilayers grown on GaAs, *Phys. Rev. B* **72**, 144402 (2006).
- [13] A. K. Das, C. Pampuch, A. Ney, T. Hesjedal, L. Däweritz, R. Koch, and K. H. Ploog, ferromagnetism of MnAs studied by heteroepitaxial films on GaAs(001), *Phys. Rev. Lett.* **91**, 087203 (2003).
- [14] S. Hara and T. Fukui, Hexagonal ferromagnetic MnAs nanocluster formation on GaInAs/InP

- (111)B layers by metal-organic vapor phase epitaxy, *Appl. Phys. Lett.* **89**, 113111 (2006).
- [15] S. Hara, D. Kawamura, H. Iguchi, J. Motohisa, and T. Fukui, Self-assembly and selective-area formation of ferromagnetic MnAs nanoclusters on lattice-mismatched semiconductor surfaces by MOVPE, *J. Cryst. Growth* **310**, 2390 (2008).
- [16] S. Ito, S. Hara, T. Wakatsuki, and T. Fukui, Magnetic domain characterizations of anisotropic-shaped MnAs nanoclusters position-controlled by selective-area metal-organic vapor phase epitaxy, *Appl. Phys. Lett.* **94**, 243117 (2009).
- [17] T. Wakatsuki, S. Hara, S. Ito, D. Kawamura, and T. Fukui, Growth Direction Control of Ferromagnetic MnAs Grown by Selective-Area Metal–Organic Vapor Phase Epitaxy, *Jpn. J. Appl. Phys.* **48**, 04C137 (2009).
- [18] M. T. Elm, C. Michel, J. Stehr, D. M. Hofmann, P. J. Klar, S. Ito, S. Hara, and H.-A. Krug von Nidda, Comparison of the magnetic properties of GaInAs/MnAs and GaAs/MnAs hybrids with random and ordered arrangements of MnAs nanoclusters, *J. Appl. Phys.* **107**, 013701 (2010).
- [19] M. T. Elm and S. Hara, Transport properties of hybrids with ferromagnetic MnAs nanoclusters and their potential for new magnetoelectronic devices, *Adv. Mater.* **26**, 8079 (2014).

-
- [20] S. Hara and K. Komagata, Selective-area growth and magnetic reversals of ferromagnetic nanoclusters on semiconducting substrate for magnetic logic applications, *Phys. Status Solidi B* **252**, 1925 (2015).
- [21] C. Guillaud, Transformation point of the compounds MnAs and MnBi in relation to a possible mechanism of antiferromagnetism, *J. Phys. Radium* **12**, 223 (1951).
- [22] M. Arejdal, L. Bahmad, and A. Benyoussef, The calculated magnetic properties and magneto-caloric effect in compound MnAs, *J. Supercond. Nov. Magn.* **30**, 1565 (2017).
- [23] J. B. Goodenough and J. A. Kafalas, High-pressure study of the first-order phase transition in MnAs, *Phys. Rev.* **157**, 389 (1967).
- [24] F. Ishikawa, K. Koyama, K. Watanabe, and H. Wada, Field induced structural transformation in MnAs, *Jpn. J. Appl. Phys.* **42**, L918 (2003).
- [25] M. Shirai, T. Ogawa, I. Kitagawa, and N. Suzuki, Band structures of zinc-blend-type MnAs and $(\text{MnAs})_1(\text{GaAs})_1$ superlattice, *J. Magn. Magn. Mater.* **177**, 1387 (1998).
- [26] M. Yokoyama, H. Yamaguchi, T. Ogawa, and M. Tanaka, Zinc-blend-type MnAs nanoclusters embedded in GaAs, *J. Appl. Phys.* **97**, 10D317 (2005).
- [27] S. Sanvito, H. A. Hill, Grand states of half-metallic zinc-blende MnAs, *Phys. Rev. B* **62**, 15553 (2000).

- [28] B. Sanyal, L. Bergqvist, and O. Eriksson, Ferromagnetic materials in zinc-blende structure, *Phys. Rev. B* **68**, 054417 (2003).
- [29] K. Ono, J. Okabayashi, M. Mizuguchi, M. Oshima, A. Fujimori, and H. Akinaga, Fabrication, magnetic properties, and electronic structures of nanoscale zinc-blende MnAs dots, *J. Appl. Phys.* **91**, 8088 (2002).
- [30] M. Moreno, A. Trampert, B. Jenichen, L. Daueritz, and K. H. Ploog, Correlation of structure and magnetism in GaAs with embedded (Mn, Ga)As magnetic nanoclusters, *J. Appl. Phys.* **92**, 4672, (2002).
- [31] T. W. Kim, H. C. Jeon, T. W. Kang, H. S. Lee, J. Y. Lee, and S. Jin, Microstructural and magnetic properties of zinc-blende MnAs films with half metallic characteristics grown on GaAs (100) substrates, *Appl. Phys. Lett.* **88**, 021915, (2006).
- [32] P. N. Hai, M. Yokoyama, S. Ohya, and M. Tanaka, Spin polarized tunneling in III–V-based heterostructures with a ferromagnetic MnAs thin film and GaAs:MnAs nanoclusters, *Physica E* **32**, 416 (2006).
- [33] P. N. Hai, S. Ohya, M. Tanaka, S. E. Barnes, and S. Maekawa, Electromotive force and huge magnetoresistance in magnetic tunnel junctions, *Nature* **458**, 489 (2009).

Chapter 2

Magnetic domain structures in ferromagnetic materials

2.1 Introduction

IDC predicts that the summation of all data, which is created, captured, or replicated, in the world will grow from 33 ZB in 2018 to 175 ZB in 2025 [1]. New-generation memory devices are required to have a large capacity and multiple functions. Therefore, Spin-based transistor and racetrack memory have attracted much attention and are expected as a new-generation memory using the ferromagnetic materials. In such devices, the control of the magnetic domain structure and magnetic properties such as coercive force is much crucial. This chapter explains the magnetic domain structures and magnetic anisotropies in solid. In addition, we describe and the structural and magnetic properties of MnAs.

2.2 Magnetic domain structure

In ferromagnetic materials, magnetic moments are aligned in parallel to each other, which results in a spontaneous magnetization below a certain temperature characterized as Curie-Temperature T_c . If the temperature exceeding the T_c , the material exhibits a paramagnetic behavior since the thermal energy is large enough to let the momentums become disordered. In an initial

magnetization state, bulk ferromagnetic materials spontaneously divide into magnetic domains, which is fine region aligned the magnetic moments in parallel to each other as shown in figure 2-1(a), since the magnetic dipolar appear at the surface of the materials and magnetostatic energy increase when if all magnetic moments are completely align in ferromagnetic materials. Between the magnetic domains, there is a region, in which the magnetic moments continuously change, i.e., domain wall. When the magnetization directions with adjacent two magnetic domains are anti-parallel, this domain wall is called 180° domain wall. A Bloch wall and Néel wall are typical 180° domain wall.

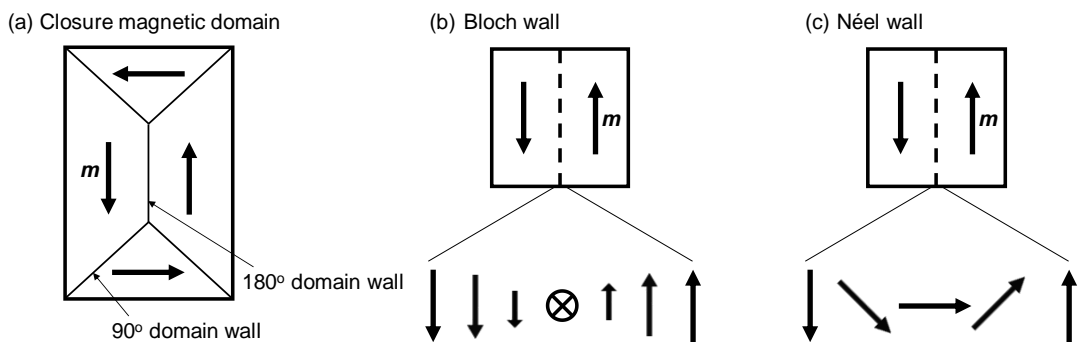


Figure 2-1. Schematic illustration of magnetic domain structures and domain walls: (a) Closure magnetic domain, (b) Bloch wall, and (c) Néel wall.

Bloch wall

A Bloch wall is mainly observed a relatively thick ferromagnetic films, or bulk ferromagnetic material. The magnetic moments in the Bloch wall continuously rotate in planes perpendicular to the film surface, and finally connect to those at the adjacent magnetic domain with opposite magnetization as shown in figure 2-1(b). The energy of Bloch wall is calculated as

functions of the film thickness and the angle through which the magnetization turns in the wall.

According to S. Middelhoek [2], the energy of Bloch wall per unit area of the wall, γ_B , is express as follow:

$$\gamma_B = A(\pi/a)^2 a + \frac{1}{2} aK + \frac{\pi a^2}{a+D} M_s^2. \quad (2-1)$$

Where, a is the wall width, D is the film thickness, M_s is the saturation magnetization, A is the exchange stiffness constant, K is the crystallographic anisotropy energy. The Bloch wall width, a , is determined to minimize this energy, a is determined to satisfy the following equation:

$$\frac{\partial \gamma_B}{\partial a} = -A(\pi/a)^2 + \frac{1}{2} K + \frac{\pi(a^2 + 2aD)}{(a+D)^2} M_s^2 = 0. \quad (2-2)$$

Néel wall

In ferromagnetic thin films, a Néel wall is dominant, since the magnetic energy due to the magnetic dipolar generated at film surface in Bloch wall increase with decreasing the film thickness. The magnetic moments in the Néel wall parallel to the film surface continuously rotate in planes parallel to the film surface, and connect to those of the adjacent domain with the opposite magnetization as shown in figure 2-1(c). In Ref. 2, the energy of Néel wall per unit area of the wall, γ_N , is express as follow:

$$\gamma_N = A(\pi/a)^2 a + \frac{1}{2} aK + \frac{\pi aD}{a+D} M_s^2. \quad (2-3)$$

In addition, the Néel wall width, a , is determined to minimize this energy, a is determined to satisfy the following equation:

$$\frac{\partial \gamma_N}{\partial a} = -A(\pi/a)^2 + \frac{1}{2} K + \frac{\pi D^2}{(a+D)^2} M_s^2 = 0. \quad (2-4)$$

The number of magnetic domains is decreasing with miniaturizing the ferromagnetic materials since the magnetostatic energy is proportion to volume of the ferromagnetic materials. In the small ferromagnetic materials, the domain wall energy generated by dividing a single domain into two magnetic domains is higher than the magneto-static energy in a single domain state. On the other hand, in the ferromagnetic materials with a comparatively large size, this domain wall energy is lower than the magneto-static energy in a single domain state. Therefore, the number of magnetic domains is decreasing with miniaturizing the ferromagnetic materials. The magnetization direction strongly depends on crystallographic orientation and shape of ferromagnetic materials, i.e., ferromagnetic materials have magnetocrystalline anisotropy and shape anisotropy.

2.3 Magnetocrystalline anisotropy

The direction of magnetization in ferromagnetic material depend on the crystallographic orientation of the material, i.e., the magnetic moments in the material are preferentially aligned along to energetically favorable orientation, or magnetization easy axes of materials. Unfavorable orientations are referred to as hard magnetic axes. A magnetocrystalline anisotropy is mainly induced by spin-orbit interactions in addition to the anisotropic crystal field. A hexagonal NiAs-type MnAs has a uniaxial magnetic anisotropy where the $<0001>$ orientation present a hard axis of magnetization [3, 4]. In addition, an easy axis of magnetization is parallel to $<11-20>$ orientation, a six-fold magnetic anisotropy is observed in (0001) plane [3–5]. The energy, which is required for the magnetization to tilt from $<11-20>$ to $<0001>$ orientation, E_{crys} , is given as follow:

$$E_{crys} = K_u \sin^2 \theta. \quad (2-5)$$

Where, K_u is the uniaxial magnetic anisotropy constant, θ is the angle between the magnetization direction and $<11-20>$ orientation. A schematic drawing of this magnetocrystalline anisotropy energy is shown in figure 2-2.

2.4 Shape anisotropy

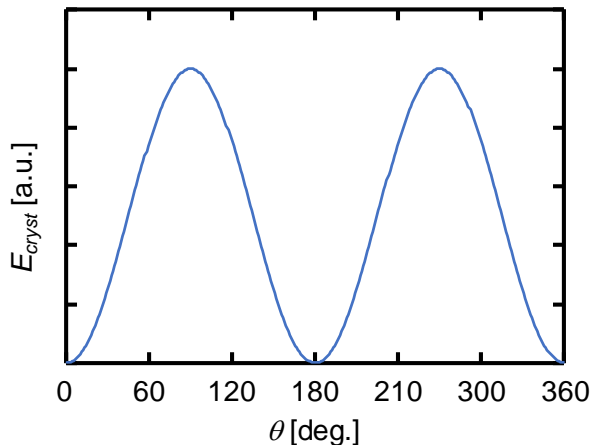


Figure 2-2. The energy of a uniaxial magnetic anisotropy required for the magnetization to tilt from $<11-20>$ to $<0001>$ orientation. The angle of $\theta = 0$ degree is corresponding to the $<11-20>$ orientation of hexagonal MnAs.

The direction of magnetization in ferromagnetic material also depend on the shape of the material. The demagnetizing magnetic field or stray magnetic field, \mathbf{H}_d , is generated by the magnetization, \mathbf{M} , within the specimen, and can express as following equation:

$$\mathbf{H}_d = \mathbf{NM}. \quad (2-6)$$

Where, \mathbf{N} is demagnetizing factor. In addition, the energy for the strain magnetic field, E_s , can calculate by following equation:

$$E_s = \int_V \mu_0 \mathbf{M} \mathbf{H}_d dV = \frac{1}{2} V \mu_0 \mathbf{M} \mathbf{N} \mathbf{M} \quad (2-7)$$

In general, the \mathbf{N} is written as a tensor \mathbf{N} . In the case of an ellipsoidal shape, it has the diagonalized form

$$\mathbf{N} = \begin{pmatrix} N_x & 0 & 0 \\ 0 & N_y & 0 \\ 0 & 0 & N_z \end{pmatrix}. \quad (2-8)$$

Where the diagonal elements, N_x , N_y , and N_z are defined by the three principal axes of an ellipsoid. There are some symmetric shapes which can be described with a diagonalized \mathbf{N} as shown in figure 2-3: For a spherical body, N_x , N_y , N_z are equal to 1/3. For an infinitely expanded thin layer in x-y plane, N_z is equal to 1 while N_x and N_y are equal to 0. For an infinitely elongated wire along z-axis, N_z is equal to 0 while N_x and N_y are equal to 0.5.

In this study, we roughly estimated the demagnetizing factor, \mathbf{N} , using the expressed equation in Ref. 6 to calculate the magnetostatic energy of MnAs nanostructures, which were approximated as ellipsoidal structure.

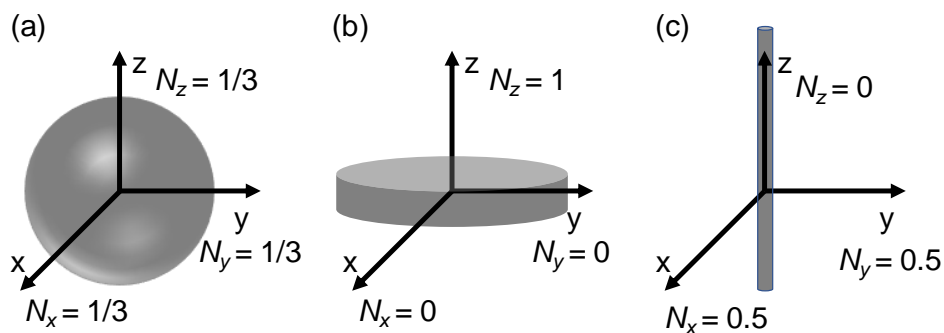


Figure 2-3. The demagnetizing factor for (a) spherical body, (b) infinity expanded thin layer in x-y plane, and (c) infinity elongated wire.

2.5 Magnetic tunnel junction

The magnetic tunnel junctions (MTJs) are highly expected to realize nonvolatile memories and spintronic devices because ferromagnetic materials are used as electrodes in the MTJs, in which the spin states are kept without any energy consumption. Figure 2-4 shows the schematic illustrations of MTJ structure. MTJ structure consist of two ferromagnetic layers and a insulating tunnel barrier layer. The resistance of MTJ structure depends on magnetization configuration of ferromagnetic layers. MTJs exhibit qualitatively the same features in spite of different mechanisms, i.e., a low resistance is achieved in parallel magnetization and it becomes low in antiparallel magnetization. This phenomenon is called the tunneling magnetoresistance effect. The magnetoresistance ratio is defined by

$$\text{TMR ratio} = \frac{R_{\text{anti-para}} - R_{\text{para}}}{R_{\text{para}}} = \frac{2P_1 P_2}{1 - P_1 P_2}. \quad (2-9)$$

Where, $R_{\text{anti-para}}$ and R_{para} are the resistance in the parallel and antiparallel magnetization configurations, respectively. P_1 and P_2 are spin polarizations ratio of the two ferromagnetic layers. Therefore, the spin polarizations ratio of two ferromagnetic layers is also important for MTJs.



Figure 2-4. Schematic illustrations of MTJ structure: (a) When the magnetization in free layer is parallel to that in fixed layer, MTJ structure has a relatively low resistance. On the other hand, (b) when the magnetization of free layer is anti-parallel to that in fixed layer, MTJ structure has a relatively high resistance.

Bibliography

- [1] David Reinsel – John Gantz – John Rydning, The digitization of the world from edge to core, Framingham: International Data Corporation (2018).
- [2] S. Middelhoek, Domain walls in thin Ni–Fe films, *J. Appl. Phys.* **34**, 1054 (1963).
- [3] F. Schippan, G. Behme, L. Daweritz, and K. H. Ploog, Magnetic structure of epitaxially grown on GaAs(001), *J. Appl. Phys.* **88**, 2766 (2000).
- [4] V. Garcia, M. Marangolo, M. Eddrief, and V. H. Etgens, Magnetization reversal and anomalous dependence of the coercive field with temperature in MnAs epilayers grown on GaAs, *Phys. Rev. B* **72**, 144402 (2006).
- [5] S. Hara and T. Fukui, Hexagonal MnAs nanocluster formation on GaInAs/InP (111)B layers by metal-organic vapor phase epitaxy, *Appl. Phys. Lett.* **89**, 113111 (2006).
- [6] J. A. Osborn, Demagnetizing factors of the general ellipsoid, *Phys. Rev.* **67**, 351 (1945).
- [7] A. K. Das, C. Pampuch, A. Ney, T. Hesjedal, L. Däweritz, R. Koch, and K. H. Ploog, ferromagnetism of MnAs studied by heteroepitaxial films on GaAs(001), *Phys. Rev. Lett.* **91**, 087203 (2003).
- [8] M. T. Elm, C. Michel, J. Stehr, D. M. Hofmann, P. J. Klar, S. Ito, S. Hara, and H.-A. Krug

von Nidda, Comparison of the magnetic properties of GaInAs/MnAs and GaAs/MnAs hybrids with random and ordered arrangements of MnAs nanoclusters, *J. Appl. Phys.* **107**, 013701 (2010).

[9] C. Guillaud, Transformation point of the compounds MnAs and MnBi in relation to a possible mechanism of antiferromagnetism, *J. Phys. Radium* **12**, 223 (1951).

[10] M. Arejdal, L. Bahmad, and A. Benyoussef, The calculated magnetic properties and magneto-caloric effect in compound MnAs, *J. Supercond. Nov. Magn.* **30**, 1565 (2017).

[11] J. B. Goodenough and J. A. Kafalas, High-pressure study of the first-order phase transition in MnAs, *Phys. Rev.* **157**, 389 (1967).

[12] F. Ishikawa, K. Koyama, K. Watanabe, and H. Wada, Field induced structural transformation in MnAs, *Jpn. J. Appl. Phys.* **42**, L918 (2003).

[13] M. Shirai, T. Ogawa, I. Kitagawa, and N. Suzuki, Band structures of zinc-blend-type MnAs and $(\text{MnAs})_1(\text{GaAs})_1$ superlattice, *J. Magn. Magn. Mater.* **177**, 1387 (1998).

[14] M. Yokoyama, H. Yamaguchi, T. Ogawa, and M. Tanaka, Zinc-blend-type MnAs nanoclusters embedded in GaAs, *J. Appl. Phys.* **97**, 10D317 (2005).

Chapter 3

Experimental techniques

3.1 Introduction

This chapter describes the growth of MnAs nanodisks and lateral nanowires, and characterization methods used in this study. The MnAs nanostructures are continuously grown by selective-area metal-organic vapor phase epitaxy (SA-MOVPE) after growth of AlGaAs nanopillar (NP) buffers. In this chapter, first, the overview of MOVPE are briefly explained, and then the characterization methods are described.

3.2 Overview of SA-MOVPE

Nanospintronic devices using ferromagnetic nanostructures have been mainly fabricated by top-down fabrication techniques, that is, etching process after ferromagnetic metal deposition. However, such ferromagnetic nanostructures have some problems, which lead to deterioration of the device performance, such as process-induced damage to surface of nanostructure and relatively poor size uniformity. To solve such problems, we use SA-MOVPE for fabrication of MnAs nanostructures on semiconducting substrates. SA-MOVPE is one of the bottom-up crystal growth techniques using metal-organic (MO) source and no catalyst using partially SiO₂-masked semiconducting substrates, which has enabled us to control the size, aspect ratio, position, and

density of nanostructures on various semiconducting substrates. Figure 3-1 shows a schematic illustration of lateral MnAs nanowire (NW) growth process of the SA-MOVPE method. First, SiO_2 thin films are deposited on the semiconducting substrates. Initial rectangular openings in the SiO_2 thin films are next fabricated by lithography and etching techniques. Finally, nucleation occurs on the substrate surface within the mask opening regions, and then the lateral NW begins to grow by supplying organometallic and hydride sources.

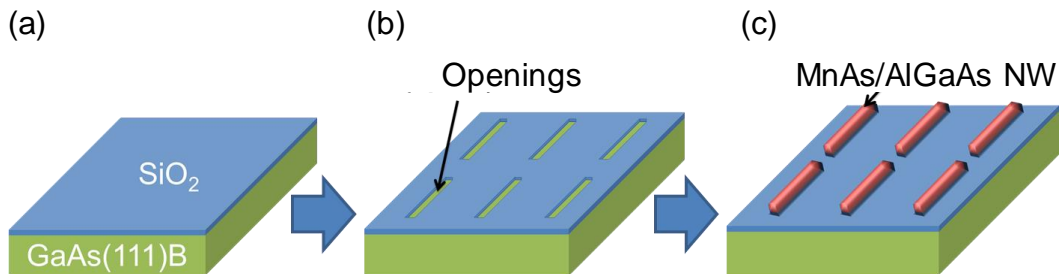


Figure 3-1. Schematic illustration of catalyst-free SA-MOVPE growth. (a) SiO_2 thin film is deposited on the GaAs (111)B substrates. (b) Initial rectangular opening is fabricated in the SiO_2 thin film by lithography and etching. (c) Nucleation occurs on the substrate surface within the mask opening region, and then lateral MnAs NW begins to grow.

3.3 Growth system for MOVPE

Figure 3-2 shows schematic illustration of the MOVPE system utilized in this study. This MOVPE system consists of the gas delivery system, the horizontal reactor with a radio frequency (RF) coil, which is used as a heating the semiconducting substrates, and the pump

system for decompression. Pure hydrogen (H_2) is purified by H_2 purifier with palladium alloy membrane, and used as a carrier gas, which transports the source materials into the reactor. The gas such as arsine (AsH_3) and MO sources such as trimethylgallium (TMG) are provided from the gas cylinders and bubblers, respectively, and its partial pressure is controlled by mass-flow controllers. Figure 3-3 shows schematic illustration of the bubblers. In the bubbler, the temperature is kept at a constant value to control the amount of supplied materials, and the pressure is controlled by pressure control valves. The total gas flow rate in the reactor is maintained at 3.00 SLM. The working pressure is automatically controlled at 0.1 atm, i.e., 76 Torr, by an automatic pressure controller and a vacuum pumping during the MOVPE growth. For the growth of the MnAs nanostructure in this study, bis(methyl- η^5 -cyclopentadienyl)manganese ($(MeCp)_2Mn$) and 20%- AsH_3 diluted in H_2 are used. In addition, for the growth of AlGaAs NP buffers, trimethylaluminum (TMAI), TMG, and 20%- AsH_3 diluted in H_2 are used.

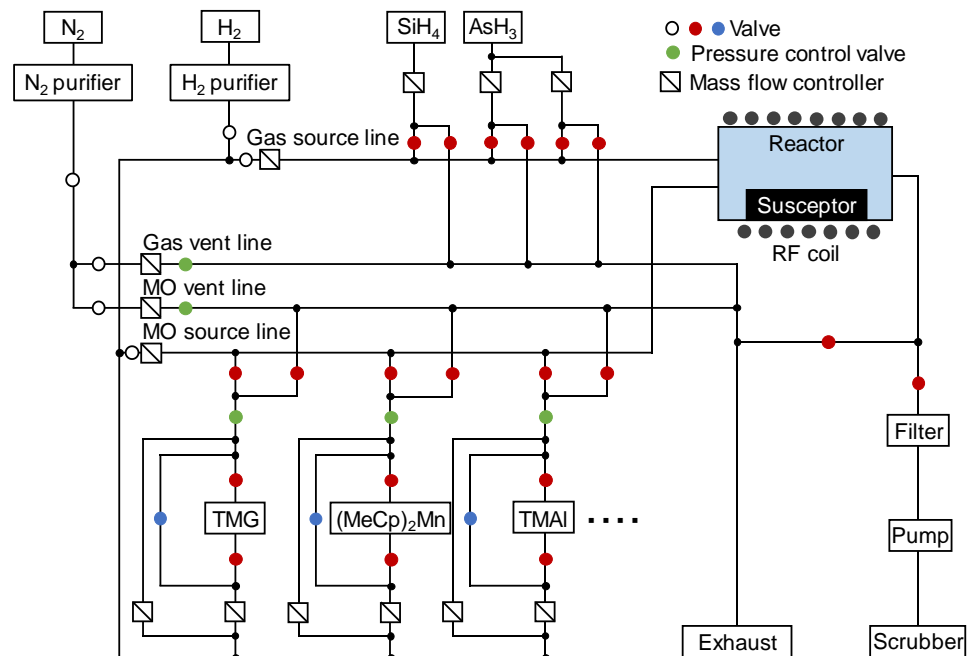


Figure 3-2. Schematic illustration of growth system for MOVPE.

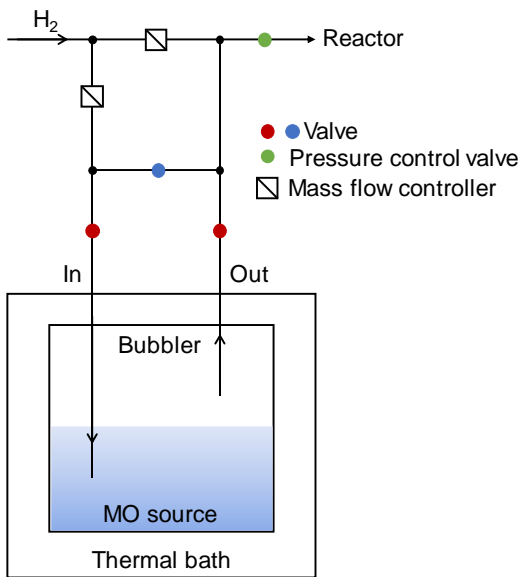


Figure 3-3. Schematic illustration of bubbler. When the MO source is provided, the red (blue) valves are opened (closed).

3.4 Preparation of substrates for MOVPE growth

The preparation of the substrates for the growth of MnAs nanostructure is as follows.

First, SiO₂ and SiON thin films were deposited on Si (111) substrates as a mask material by thermal oxidation and chemical vapor deposition, respectively. In addition, SiO₂ thin films were deposited on GaAs (111)B substrates by plasma sputtering system (CFS-4EP-LL, Shibaura Mechatronics Corporation). The thickness of SiO₂ and SiON thin films were estimated to be approximately 30 nm. After ultrasonic cleaning in acetone, ethanol, and ultrapure water for 5 min in each, an electron beam (EB) resist (ZEP520A-7, Nippon Zeon) was coated on the substrates by a spin coater, and then, the substrates were pre-baked at 170 °C for 2 min and 90 °C for 5 min. Next, the EB resist are exposed by EB lithography system (JBX-6300SF, JEOL) at an accelerating

voltage of 100 kV for making periodical mask opening patterns in the EB resist. After EB exposure, the EB resist are developed with ZED-N50 solution for 90 sec, and rinsed with isopropyl alcohol (IPA) for 60 sec. The substrates are then post-baked at 140 °C for 10 min and cooled at room temperature. To form the periodical mask openings formed in SiO₂ and SiON thin films, dry etching and wet etching are carried out by reactive ion etching system with CF₄ and buffered hydrogen fluoride, respectively, and the EB resist films are removed by methyl-ethyl-ketone (MEK). Before loading samples into the reactor, the substrates are cleaned with organic solvents in an ultrasonic bath, and the unintentional native oxide on the surface of the substrates are removed by alkali solution (Semico Clean 23, Furuuchi Chemical) for 10 min in an ultrasonic bath.

3.5 Characterization methods

3.5.1 Scanning electron microscopy

For structural characterization of MnAs nanostructures, secondary electron images by scanning electron microscopy (SEM), S-4100 and SU-8010, Hitachi, are observed. The SEM system consists of an EB gun, condenser lenses, apertures, scanning coils, an objective lens and a specimen chamber as shown in figure 3-4. In addition, to estimate the size of the nanostructures and roughly obtain the information of solid composition, the backscattered electron (BSE) images by SEM are observed.

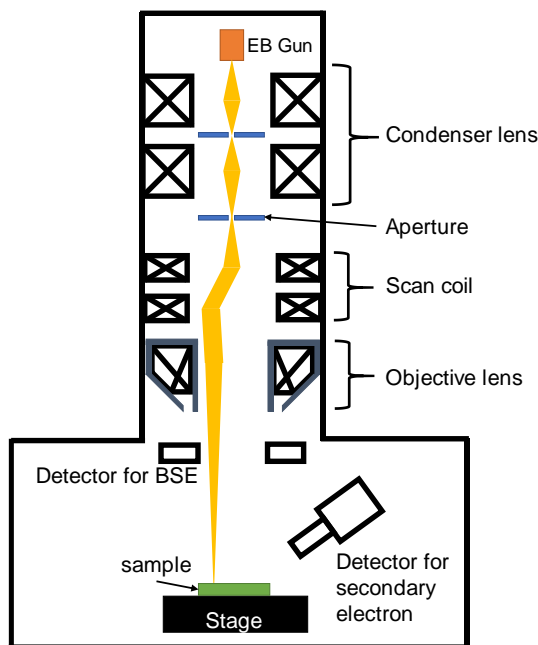


Figure 3-4. Schematic illustration of SEM systems. SEM consists of an EB gun, condenser lenses, apertures, polarized coils, an objective lens and a specimen chamber.

Secondary electron image

For structural characterization, secondary electron images of MnAs nanostructures and AlGaAs NP buffers grown on semiconducting substrates in this study are observed to characterize the shape and surface morphologies of the nanostructures. Secondary electron image is formed by detecting secondary electrons, which are generated from the atoms in sample by in elastic scattered incident electrons, i.e., primary electrons. Since the energy of the secondary electrons are several 10 eV, only secondary electrons, which are generated within about 10 nm from the surface of the sample, are emitted in vacuum. Therefore, secondary electron image is highly sensitive to the surface structure of the sample. In this study, when we observed BSE image, the accelerating voltage of 5.0 and 30.0 kV in SU-8010 and S-4100, respectively.

BSE image

To estimate the size and roughly obtain the information of solid composition, the BSE images by SEM are observed. BSE image is formed by electrons, which are scattered backward against the primary electron in the electron-scattered process. BSE image is highly sensitive to a solid composition of materials since BSE emission increases with increasing mean atomic number of materials [1]. In addition, the penetration length of electrons from the surface increases with increasing an acceleration voltage of electrons [2]. To estimate the maximum penetration length, L_p , of electrons for MnAs, we use following equation:

$$L_p = \frac{2.76 \times 10^{-11} A E_0^{5/3}}{\rho Z^{8/9}} \frac{(1 + 0.978 \times 10^{-6} E_0)^{5/3}}{(1 + 1.957 \times 10^{-6} E_0)^{4/3}} \quad (3-1)$$

Where, A is atomic weight (g), ρ is atomic density (g/cm^3), Z is atomic number, and E_0 is incident energy (eV). In this study, when we observed BSE image, the accelerating voltage of 0.5 to 5.0 kV is used for the estimation of the thickness of MnAs nanostructures.

3.5.2 Magnetic force microscopy

For characterization of magnetic domain structure, we use magnetic force microscopy (MFM) combined with tapping mode atomic force microscopy (AFM) in a Nanoscope IIIa system, Digital Instruments at room temperature using a high-resolution-type MFM tip of Si coated with a Co/Cr alloy (Bruker MESP-HR10). The coercivity of the MFM tip used is 950 Oe according to the specification sheet published by Bruker AXS. The cantilever is magnetized by permanent

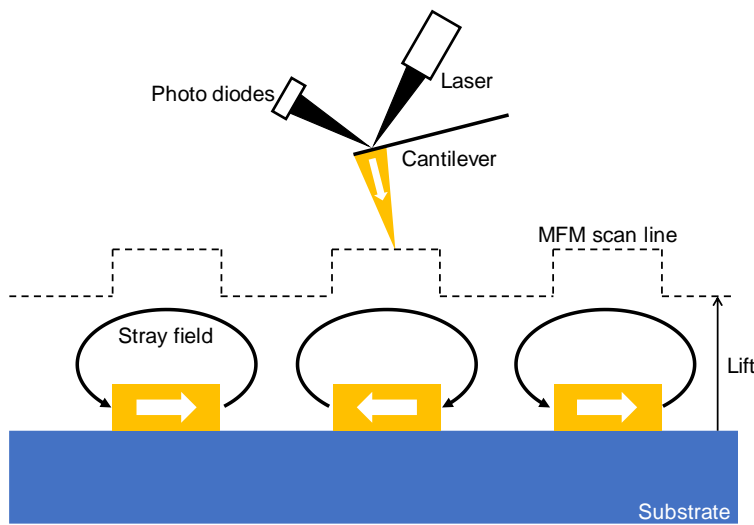


Figure 3-5. Measurement principle of MFM observation.

magnet and oscillating at its resonance frequency during AFM and MFM measurement. Figure 3-5 shows the principle of MFM. To separate the information of the surface morphologies and magnetic information, first, AFM measurement are carried out before MFM observations. During the MFM observation, the cantilever is lifted off from the sample surface, and sense the stray magnetic fields from the sample. In this study, we use phase detection mode to obtain the MFM images. A repulsive magnetic force gradient will cause the resonance curve to shift to a higher frequency, accompanied by an increase in phase shift. On the other hand, an attractive magnetic force gradient will cause the resonance curve to shift to a lower frequency, accompanied by a decrease in phase shift as shown in figure 3-6. The relationship of force gradients and shift direction of resonance and phase curve is summarized in Table 3-1. We usually observed the same ferromagnetic MnAs nanostructure again after switching the magnetization direction of MFM cantilever to confirm that the obtained image contrasts are due to magnetic information.

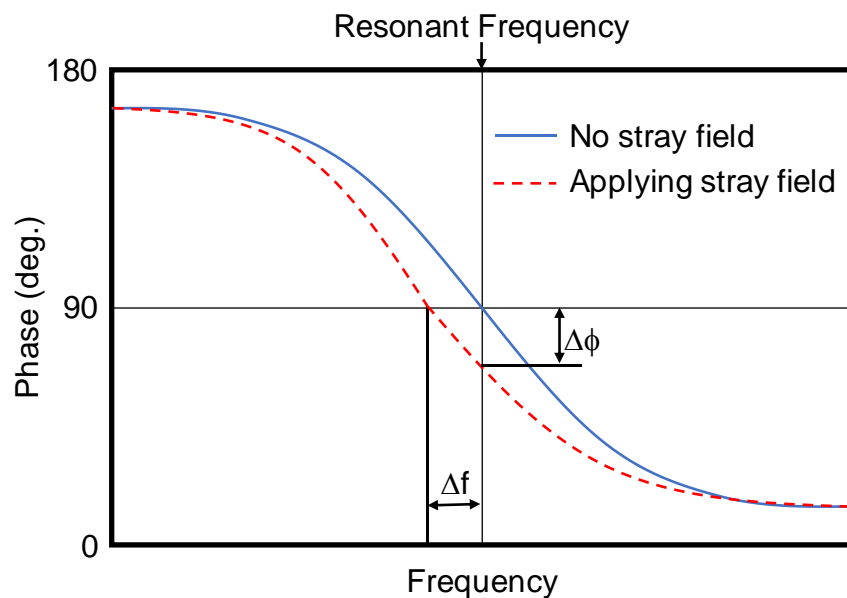


Figure 3-6. Shift of phase curve by stray magnetic fields from specimen.

Table 3-1 The summary of the relationship of force gradient, shift direction of phase curve, and

change in phase, ϕ , and image contrast.

Force gradient	Shift direction of Phase curve	Change in $\Delta\phi$	Image contrast
Attractive force	Lower frequency	Decrease	Darkness
Repulsive force	Higher Frequency	Increase	Brightness

Bibliography

- [1] K. Kanaya, S. Okayama, Penetration and energy-loss theory of electrons in solid targets, *J. Phys. D* **5**, 43 (1972).
- [2] E. Sánchez, M. T. Deluigi, G. Castellano, Mean atomic number quantitative assessment in backscattered electron imaging, *Microsc. Microanal.* **18**, 1355 (2012).

Chapter 4

Selective-area growth of ferromagnetic MnAs nanodisks on Si (111) substrates covered with multiple types of dielectric masks

In this chapter, we report on selective-area metal-organic vapor phase epitaxy (SA-MOVPE) and structural characterizations of MnAs nanodisk (ND) structures after the AlGaAs nanopillar (NP) buffer growth on Si (111) substrates using multiple types of mask materials and designs, which are mask patterns (I) and (II) of SiO_2 and SiON removing (I) the mask materials outside $100 \times 100 \mu\text{m}^2$ square regions with periodical circular openings and (II) only the periodical circular openings within the $100 \times 100 \mu\text{m}^2$ square regions. The results of structural characterizations show that two key issues, which are the unintentional growth of MnSi alloy in Si substrates and MnAs alloy with approximately 17% of Si atoms on NDs, are typically observed in the case of Si substrates with mask pattern (I) of SiO_2 . On the other hand, these two key issues are not observed in the case of Si substrates with mask pattern (II) of SiON . These results suggest that mask pattern (II) of SiON are effective to prevent the unintentional reactions of Mn atoms with Si substrates for growing MnAs NDs with a high degree of uniformity. (This chapter is described mainly based on our previous study in Ref. 1)

4.1 Introduction

Recently, the research on magnetic tunnel junctions (MTJs) has attracted considerable attention [2–7]. The MTJs are highly expected to realize nonvolatile memories because ferromagnetic materials are used as electrodes in the MTJs, in which the spin states are kept without any energy consumption. In addition, racetrack memory cell arrays integrated on Si substrates with MTJ read elements and complementary metal-oxide semiconductor field-effect transistors have been intensively demonstrated [8, 9]. In magnetic memories, in general, thermal stability factor, i.e., $KV/k_B T$, must exceed 60 to ensure that the magnetization direction of magnetic materials remains stable for archiving in 10 years at least, where K , V , k_B , T are the magnetic anisotropy constant, the volume of magnetic materials, Boltzmann constant, and temperature, respectively. To miniaturize magnetic memories, a high magnetic anisotropy constant is required. The fabrication of MTJs using MnAs has been actively performed as a different approach [6, 7] because bulk MnAs shows ferromagnetism at room temperature and has a relatively high uniaxial magnetic anisotropy energy [10]. MTJs using MnAs have been demonstrated in the combination with III-V compound semiconductors, such as GaAs and AlAs, mainly by low temperature molecular beam epitaxy and conventional top-down-type fabrication methods. However, the performance of devices fabricated by such conventional methods possibly deteriorates owing to process-induced damages and a relatively low size uniformity, in particular, on the way towards a further device miniaturization. To solve such a possible problem, we have investigated a bottom-up-type fabrication of ferromagnetic MnAs nanostructures on GaAs (111)B substrates by SA-MOVPE [11–14]. It enables us to control the size, density, position, and shape of nanostructures without any process-induced damage and contamination. Spin-transfer-torque-switching metal-oxide-semiconductor field effect transistors (STS-MOSFET) using MTJ electrodes as source and

drain electrodes have been proposed as a novel spin-based MOSFET [15], and the materials with a long spin life time is required as the channel materials in STS-MOSFET. Si has a relatively long spin lifetime of approximately 1.3 nsec at 300 K [16]. In the case of GaAs, on the other hand, the spin lifetime is reported to be approximately 60 psec at 300 K [17]. In this paper, for realizing magnetic memories using MTJs with ferromagnetic MnAs nanostructures, we report on SA-MOVPE and structural characterizations of MnAs NDs on Si (111) substrates. Multiple types of mask materials and designs as a growth inhibiting mask were investigated for the optimization of selective-area growth of MnAs on Si.

4.2 Experimental procedure

Two types of thin film amorphous materials were chosen as a growth inhabiting mask materials for SA-MOVPE since the lateral over-growth rate depends on surface activation energy of mask materials for nucleation: One was SiO_2 , which was formed by thermal oxidation on Si (111) substrates, and the other was SiON , which was deposited on Si (111) substrates by plasma enhanced chemical vapor deposition. The film thickness was about 30 nm. In current work, we used SiON instead of SiN_x since the etching rate of SiN_x by wet chemical etching using a buffered hydrofluoric acid is too slow. For the deposition of SiON thin films, SiH_4 , NH_3 , and N_2O gases were used as a source at the flow rates of 0.6, 4.0, and 1.5 slm, respectively. The content of nitrogen in the SiON thin films, therefore, is supposed to be high, although no detailed information on the solid composition of SiON is obtained. Subsequently, we formed periodical circular openings, whose diameters were designed to be approximately 230, 245, and 270 nm, in the films as a mask for the selective-area growth of magnetic nanostructures by electron beam

lithography and wet chemical etching. The periods of circular openings were approximately 0.5, 1.5, and 3.0 μm . As shown in Fig. 4-1, we prepared two types of mask patterns using SiO_2 and SiON : (I) The mask pattern of one type was the one that the films outside $100 \times 100 \mu\text{m}^2$ square regions with periodical circular openings were removed (Fig. 4-1(a)). (II) That of another type was the one that the films were removed only for the periodical circular openings within the $100 \times 100 \mu\text{m}^2$ square regions (Fig. 4-1(b)). Hereafter, these two patterns are referred to as mask pattern (I) and (II), respectively.

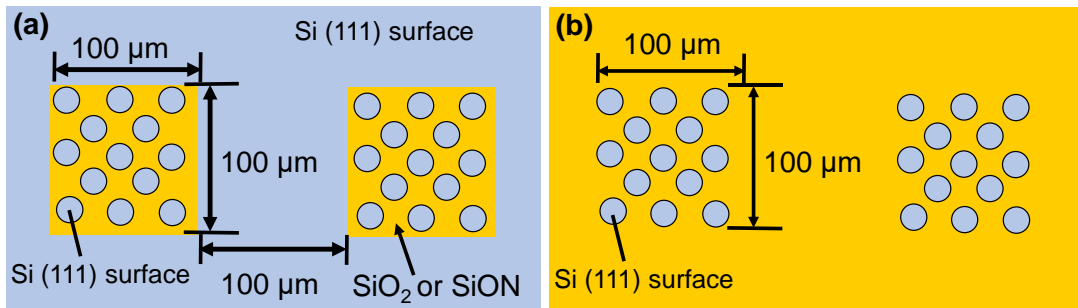


Figure 4-1. Schematic illustrations of mask patterns (I) and (II) for the selective-area growth: (a) SiO_2 or SiON films outside $100 \times 100 \mu\text{m}^2$ square regions with periodical circular openings were removed, which are referred to as “mask pattern (I)”, and (b) SiO_2 or SiON films were removed only for the periodical circular openings within the $100 \times 100 \mu\text{m}^2$ square regions, which are referred to as “mask pattern (II)”.

First of all, we had tried to grow MnAs nanostructures directly on Si (111) substrates with the mask pattern (I) of SiO_2 by SA-MOVPE. $(\text{CH}_3\text{C}_5\text{H}_4)_2\text{Mn}$ and 20%- AsH_3 diluted in H_2 were used as source materials for the MnAs growth, and their partial pressures were 5.2×10^{-7} and 5.8×10^{-4} atm, respectively. In all the SA-MOVPE growth, the total pressure in the reactor was 0.1 atm. The growth temperature was 800°C. In our previous study [18], the unintentional deposition of MnAs nanoparticles were observed on SiO_2 mask surfaces at the growth temperature of 750°C. Therefore, a relatively high growth temperature of 800°C was required to enhance the

surface migration of ad-atoms on SiO_2 mask surfaces as well as the thermal decomposition of $(\text{CH}_3\text{C}_5\text{H}_4)_2\text{Mn}$ source materials. It was extremely difficult to grow MnAs directly on Si substrates possibly owing to high reactivity between Mn and Si under the standard SA-MOVPE conditions for the MnAs growth without an interlayer, as shown in Fig. 4-2(a). We reported on one of the solutions to this problem, in which we used crystallized Al_2O_3 interlayers before the MnAs/AlGaAs nanostructure growth to prevent unintentional Mn diffusion into Si substrates [19]. Since we still have a difficulty in the growth of MnAs nanostructures with a high degree of uniformity mainly owing to the incomplete crystallization of Al_2O_3 interlayers, however, we have investigated the designs and materials of mask patterns on Si (111) substrates for SA-MOVPE in the current work to offer other solutions to the high reactivity problem. In the case of the direct growth of MnAs on GaAs (111)B substrates partially covered with SiO_2 mask, unintentional GaAs layers were formed under MnAs nanostructures possibly owing to the re-evaporation of Ga atoms from GaAs (111)B substrates, which were due to the gas etching by Mn precursors [18]. The mask pattern (II), therefore, was introduced to prevent the possible unintentional re-

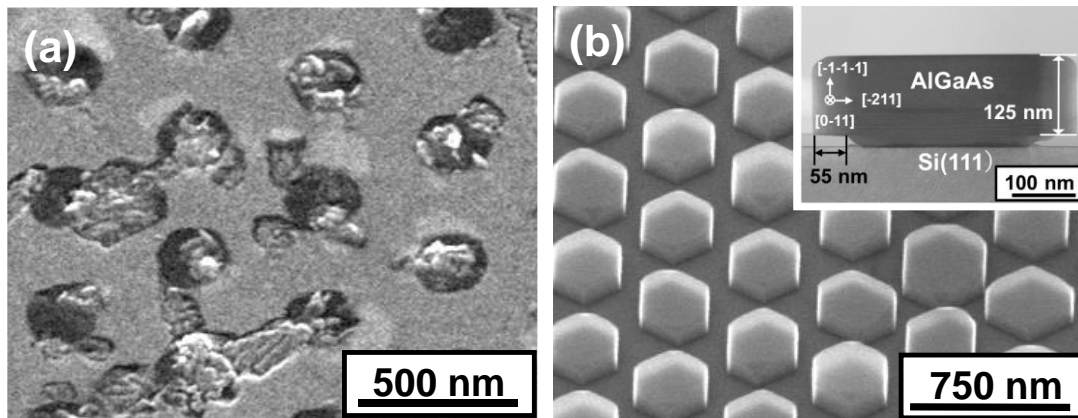


Figure 4-2. (a) Secondary electron image of MnAs directly grown on Si (111) substrates with the mask pattern (I) of SiO_2 . (b) Bird's-eye view of a secondary electron image by SEM and cross-sectional TEM image of AlGaAs NP buffers with a high degree of uniformity grown on Si (111) substrates with the mask pattern (I) of SiO_2 at the growth temperature of 800°C for 10 min. The layer thickness from the mask surface and the width from the mask edge were estimated to be 125 and 55 nm, respectively.

evaporation of Si atoms from the outside of $100 \times 100 \mu\text{m}^2$ square regions. $(\text{CH}_3)_3\text{Ga}$, $(\text{CH}_3)_3\text{Al}$, and 20%- AsH_3 diluted in H_2 were used as source materials for the AlGaAs growth at the partial pressures of 1.8×10^{-6} , 3.2×10^{-7} , and 8.0×10^{-4} atm, respectively. The growth time was 10 min for the mask pattern (I) and 20 sec for (II), respectively, and the growth temperature was 800°C. MnAs NDs were continuously formed after the AlGaAs NP buffer growth at the same partial pressures and growth temperature for the MnAs growth directly on Si (111) substrates. The growth time was 10 min for the mask pattern (I) and 1 min for (II), respectively.

For structural characterizations, secondary electron images were observed by scanning electron microscopy (SEM), S-4100 and SU-8010, Hitachi, to characterize the shape and surface morphologies of NDs. Cross-sectional images of AlGaAs NP buffers and NDs were observed by transmission electron microscopy (TEM). Energy dispersive x-ray (EDX) spectroscopy analysis and electron-beam diffraction measurement were carried out for the compositional and crystallographic characterizations of NDs. To roughly obtain the information of solid compositions, an acceleration voltage dependence of back scattered electron (BSE) images was characterized by SEM. Atomic force microscopy (AFM) was used to estimate the mean thickness of AlGaAs NP buffers from the mask surfaces.

4.3 Results and discussion

Figure 4-2(b) shows a bird's-eye view of secondary electron image of AlGaAs NP buffers grown on Si (111) substrates with the mask pattern (I) of SiO_2 . We confirmed that hexagonal AlGaAs ND structures with a high degree of uniformity were formed. Cross-sectional

TEM observation results showed that atomically flat crystal facets were formed as a top and side wall facet, as shown in the inset of Fig. 4-2(b). The observed layer thickness from the SiO_2 mask surface and the over-growth width from the mask edge were estimated to be 125 and 55 nm, respectively. In the outside of $100 \times 100 \mu\text{m}^2$ square regions, the AlGaAs NP buffers covered mostly Si substrate surface, but, had small voids or spatial gaps (not shown here). In the case of mask pattern (II) of SiO_2 , the circular openings in the mask were not fully covered with AlGaAs NP buffers (the coverage by AlGaAs NP buffers was roughly estimated to be 58%), and the mean thickness of AlGaAs NP buffers from the SiO_2 mask surface was estimated to be 66 nm by AFM. In the case of mask pattern (II) of SiON , the mean thickness of AlGaAs NP buffers from the SiON mask surface was estimated to be 78 and 79 nm at the center and edge of $100 \times 100 \mu\text{m}^2$ square regions, respectively, by AFM, and the mean lateral over-growth width from the mask edge of circular openings was estimated to be 55 nm for the center and 52 nm for the edge of $100 \times 100 \mu\text{m}^2$ square regions by SEM images. The standard deviation of the mean thickness of AlGaAs NP buffers at the center and edge of $100 \times 100 \mu\text{m}^2$ square regions was calculated to be 12 and 15 nm, respectively. These results show that there is no significant difference in the AlGaAs growth between the center and edge of $100 \times 100 \mu\text{m}^2$ square regions. In the mask patterns (II) of SiO_2 and SiON , no unintentional AlGaAs nanoprecipitate deposited on the mask surfaces were observed outside the $100 \times 100 \mu\text{m}^2$ square regions.

Figure 4-3 shows bird's-eye views of secondary electron images by SEM and a cross-sectional TEM image of the typical MnAs/AlGaAs NDs grown on Si (111) substrates with the mask pattern (I) of SiO_2 . We concluded from electron beam diffraction measurements by TEM that the crystallographic structure of all the MnAs NDs observed in the current work was hexagonal NiAs-type, and that the <0001> direction of hexagonal NiAs-type MnAs was parallel

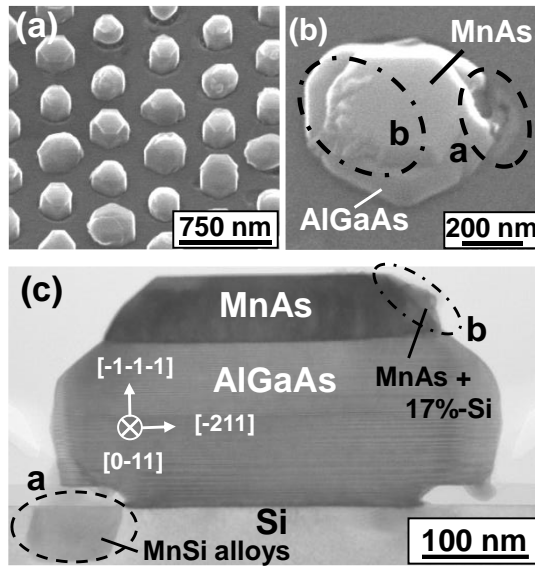


Figure 4-3. Bird's-eye view of a secondary electron image by SEM: (a) overall and (b) highly-magnified views, and (c) a cross-sectional TEM image of MnAs/AlGaAs NDs grown on Si (111) substrate with the mask pattern (I) of SiO_2 . The growth temperature and time were 800°C and 10 min for the AlGaAs and MnAs growth, respectively. Unintentional growth of MnSi alloy in Si substrates and MnAs alloy with approximately 17% of Si atoms on NDs was observed, as shown by the circle “a” of broken line and the circle “b” of dot-dash line in (b) and (c), respectively.

to both the $<111>\text{B}$ direction of zinc-blende-type AlGaAs NP buffers and the $<111>$ direction of diamond-type Si substrates. In addition, the relationships of in-plane orientations between MnAs and AlGaAs were MnAs $<11-20>$ // AlGaAs $<0-11>$ and MnAs $<1-100>$ // AlGaAs $<-211>$. As shown by the circle “a” of broken line in Figs. 4-3(b) and 4-3(c), it seemed that unintentional reactions with Si substrates were observed under the mask at around the bottom of AlGaAs NP buffers of NDs. Hereafter, this typically-observed phenomenon is referred to as “key issue A”. The other of typical phenomena we observed, which is referred to as “key issue B”, was the partially-contaminated or destroyed crystal facets of MnAs NDs, as shown by the circle “b” of dot-dash line. EDX analyses revealed that MnSi alloys were grown at the regions in the circle “a” of broken line, and that MnAs alloys with approximately 17% of Si atoms were grown at the

regions in the circle “b” of dot-dash line. No crystal structure of MnAs alloys with approximately 17% of Si atoms has been characterized. However, from the EDX results, the As content in the MnAs alloys with Si atoms was smaller than that in hexagonal NiAs-type MnAs NDs. The electron beam diffraction measurements by TEM showed that the MnSi alloys had a diamond-type structure. Therefore, the MnAs alloys with Si atoms are supposed to have hexagonal NiAs-type or diamond-type crystal structure. The dislocations were observed only in one or two monolayers of MnAs NDs near the interfaces between MnAs and AlGaAs layers. The mean period of dislocations was estimated to be approximately 4.1 nm. These dislocations could be misfit dislocations owing to the lattice mismatch between MnAs NDs and AlGaAs NP buffers since the lattice mismatch between the c-plane of MnAs and the {111}B plane of GaAs was calculated to be approximately 6.8% or higher. (From the EDX results, the Al contents of AlGaAs NP buffers were estimated to be approximately 10% at most.) Secondary, we changed mask materials from SiO_2 to SiON using the same mask pattern (I). The key issue A was still observed at around the bottom of AlGaAs NP buffers. However, it seemed that Si substrate surfaces were less exposed, comparing to the case shown by the circle “a” of broken line in Fig. 4-3(b). This was possibly because AlGaAs NP buffers grew much more predominantly in lateral direction on the SiON mask surfaces than on the SiO_2 ones, judging from the difference in secondary electron observation results of AlGaAs NP buffers using SiON and SiO_2 . We observed no key issue B, i.e., well-defined crystal facets were obtained on MnAs NDs, in the case of mask pattern (I) of SiON.

In the case of mask pattern (II) of SiO_2 , next, key issue A was still observed, whereas no key issue B was observed, similarly to the case of mask pattern (I) of SiON. Subsequently, to study the dependence on mask materials for the mask pattern (II), we only changed mask materials from SiO_2 to SiON. Figure 4-4 shows a bird’s-eye view of secondary electron image by SEM and

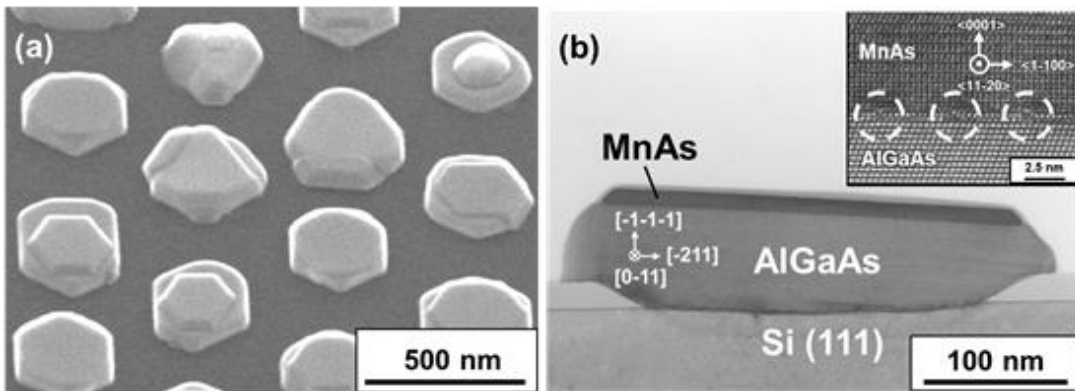


Figure 4-4. (a) Bird's-eye view of a secondary electron image by SEM and (b) a cross-sectional TEM image of MnAs/AlGaAs NDs grown on Si (111) substrates with the mask pattern (II) of SiON. The growth temperature and time were 800°C and 20 sec for the AlGaAs growth and 1 min for the MnAs growth, respectively. The tilted ND was due to the tilted (111) plane of Si substrates. It was confirmed that the (111) planes of Si substrates were parallel to the (0001) planes of hexagonal NiAs-type MnAs. The inset of (b) shows a lattice image near the interface between MnAs layer and AlGaAs layer. The dislocations were observed in the circles of broken line, and the mean period of dislocations was approximately 3.6 nm.

cross-sectional TEM images of typical NDs with the MnAs thickness of approximately 10 nm.

No key issue A and B was observed, judging from these observation results. Well-defined crystal facets were obtained for the MnAs NDs without any damage in AlGaAs NP buffers. As shown in the inset of Fig. 4(b), the dislocations were observed only in one or two monolayers of MnAs NDs near the interfaces between MnAs and AlGaAs layers. The mean period of dislocations owing to the lattice mismatch between MnAs NDs and AlGaAs NP buffers was estimated to be approximately 3.6 nm. We concluded from electron beam diffraction measurements by TEM that the crystallographic structure of all the MnAs NDs observed in the current work was hexagonal NiAs-type, and that the <0001> direction of hexagonal NiAs-type MnAs was parallel to both the <111>B direction of zinc-blende-type AlGaAs NP buffers and the <111> direction of diamond-type Si substrates. The relationships of in-plane orientations between MnAs and AlGaAs were MnAs <11-20> // AlGaAs <0-11>, and MnAs <1-100> // AlGaAs <-211>. In

addition, we confirmed from the cross-sectional analyses by TEM that the top tilted facets observed on all the NDs were due to the tilted (111) planes of Si substrates themselves, i.e., the Si (111) substrates actually have the off-angle of approximately 3 to 4 degrees. The MnAs NDs in the current work showed spontaneous magnetization at room temperature. We have observed marked magnetic domains in the NDs. Detailed analyses of magnetization and magnetic domains in the NDs are described in Chapter 5 or Ref. [20].

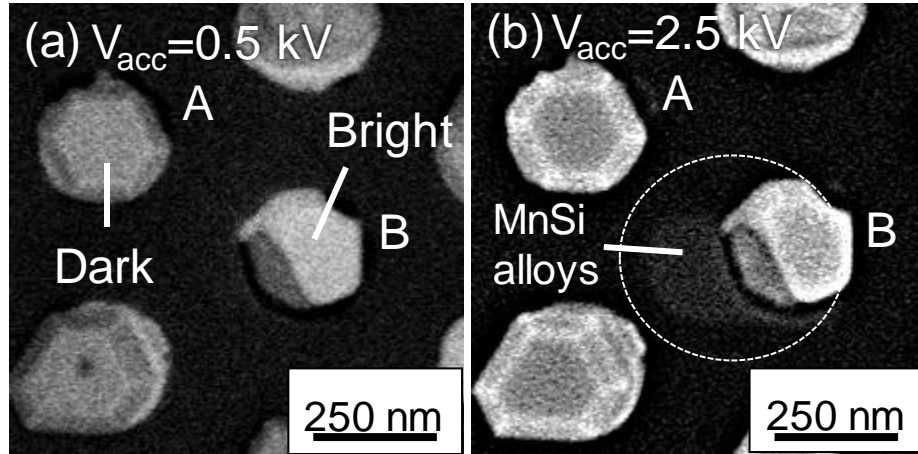


Figure 4-5. Acceleration voltage dependence of BSE images of MnAs/AlGaAs NDs grown on Si (111) substrates with the mask pattern (II) of SiO_2 : (a) 0.5 and (b) 2.5 kV. In (a), relatively dark contrasts in ND-A and brighter contrasts in the NC-B than the contrast of ND-A were observed. The different level of contrasts brighter than those of Si substrates near the NDs was observed, as in the circle of broken line in (b). These brighter contrasts were due to MnSi alloys.

Figure 4-5 shows a dependence of top views of MnAs/AlGaAs NDs grown on Si substrates with the mask pattern (II) of SiO_2 on acceleration voltage of BSE images. At the acceleration voltage of 0.5 kV, first, as shown in Fig. 4-5(a), we observed relatively dark contrasts in the ND marked by “A” and brighter contrasts than the contrast of ND-A in the ND marked by “B”. BSE images are highly sensitive to a solid composition of materials since BSE emission increases with increasing mean atomic number of materials [21]. The mean atomic number of

AlGaAs is larger than that of MnAs in the current work. Therefore, the BSE images of AlGaAs buffer layers should be brighter than those of MnAs layers. We judged in Fig. 4-5(a) that the dark and bright contrasts were due to MnAs and AlGaAs buffer layers in NDs, respectively. At the acceleration voltage of 2.5 kV or higher, we observed a different level of contrast near the NDs, which seemed to be under the mask patterns, brighter than the contrasts of SiO₂, SiON, and Si substrates in the cases of the mask patterns (I) of SiO₂ and SiON and (II) of SiO₂, as shown in the circle of broken line in Fig. 4-5(b) as an example. The penetration length of electrons from the surface increases with increasing an acceleration voltage of electrons [22]. We observed this contrast near the NDs by increasing the penetration length of electrons. The penetration lengths of electrons, for the 30-nm-thick SiO₂ mask in the case of Fig. 4-5, were calculated to be approximately 10 and 148 nm at the acceleration voltages of 0.5 and 2.5 kV, respectively, using the equation given in Ref. 22. Combining the BSE observations here with the EDX analyses and cross-sectional TEM observations in Fig. 4-3(c), we concluded that MnSi alloys, whose contrast in the BSE images should be the brightest among Si, SiO₂, SiON, and MnSi, were formed near the Si substrate surface owing to unintentional Mn diffusion into the substrates during the ND growth. In the case of mask pattern (II) of SiON, the bright contrast owing to MnSi alloys has never been observed.

From all the results obtained so far, we discuss a possible explanation for the two typically-observed phenomena, i.e., key issues A and B. The characterization results for the key issues A and B in the selective-area growth of MnAs NDs using the mask patterns (I) and (II) of SiO₂ and SiON were summarized in Table 4-1. It was likely that, at relatively high growth temperature, 800°C, of the NDs, small pin holes in SiO₂ films and/or spatial gaps at the interface between AlGaAs buffer layers and the SiO₂ mask were formed owing to relatively long growth

Table 4-1. The summary of characterization results for the key issues A and B in the selective-area growth of MnAs NDs using the mask patterns (I) and (II) of SiO₂ and SiON.

		Key issue A	Key issue B
Mask pattern (I)	SiO ₂	NG	NG
	SiON	NG	Good
Mask pattern (II)	SiO ₂	NG	Good
	SiON	Good	Good

NG: observed or not solved, Good: solved or not observed

time, 10 min, for the MnAs NDs. As a result, Mn precursors possibly reacted with Si atoms of the substrates through the pin holes and/or the spatial gaps during the MnAs growth, and then, MnSi alloys were formed near the Si substrate surfaces. The spatial gaps at the interface between AlGaAs buffer layers and the SiO₂ masks might be formed by a difference in the activation energies of mask materials. The ad-atoms, which are supplied and physically adsorbed to the substrate surfaces, migrate the substrate surface. After the ad-atoms migrate on the substrate surface, the ad-atoms chemically react with other ad-atoms and form atomic clusters on the surfaces, or re-evaporate at a certain thermodynamic probability. The atomic clusters lead to the nucleation for the crystal growth, when the energy for desorption of ad-atoms from the clusters is higher than that for bonding to other ad-atoms. These energies depend on the surface activation energy of substrate materials. As reported by Claassen and Bloem [23], in the chemical vapor deposition of Si clusters on SiO₂ and Si₃N₄ substrates, the saturation cluster density of Si deposited on Si₃N₄ substrates was higher than that on SiO₂ substrates since the activation energy for formation of Si clusters on Si₃N₄ was smaller than that on SiO₂. In the current work, we have not

determined the activation energy of SiON mask since we had no detailed information on the solid composition of SiON mask used here. However, the activation energy of SiON mask for desorption should be higher than that of SiO₂ mask because the solid composition of SiON mask should be in between SiO₂ and SiN_x. The surface diffusion of ad-atoms on the masks depends on the activation energy for desorption. The desorption rate of ad-atoms from the substrates decreases exponentially with increasing the activation energy for desorption according to the Arrhenius equation. Therefore, in the case of SiON mask, it was highly possible that the circular mask openings could thoroughly be covered with AlGaAs NP buffers because the AlGaAs nucleation could easily occur comparing to the case of SiO₂ mask. These phenomena might be one of the highly-possible reasons for the key issue A. Si atoms were presumably desorbed from the Si substrates through the pin holes and/or the spatial gaps possibly owing to gas etching effects by Mn precursors and relatively-long growth time for the MnAs NDs. The change in the shape, in particular, the edges, of AlGaAs NP buffers of NDs owing to gas etching effect by Mn precursors was markedly observed in Figs. 4-3(c) and 4-4(b), comparing to the case shown in the inset of Fig. 4-2(b). Since the enthalpies for formation of Mn₇Al and MnGa were reported to be -15 and -32 kJ/mol at room temperature, respectively [24, 25], the reactivity of Mn with Ga should be higher than that of Mn with Al. Therefore, AlGaAs with higher Al contents should have a higher tolerance in terms of the gas etching by Mn precursors. From the EDX analysis results, no change in the Al content between before and after the MnAs growth was observed, and no significant difference of Al contents between the mask pattern (I) of SiO₂ and the mask pattern (II) of SiON was confirmed. (AlGaAs NP buffers include Al atoms of approximately 10% at most in the current work.) Therefore, the gas etching rate for the mask pattern (I) of SiO₂ should be almost equal to that for mask pattern (II) of SiON. For the mask pattern (I) of SiO₂ and mask pattern (II) of SiON, the differences of AlGaAs NP buffer widths before and after MnAs growth were estimated to be

approximately 74 and 7.4 nm, respectively. For both of the mask patterns, therefore, the lateral gas etching rate was estimated to be approximately 7.4 nm/min. In our previous study [18], we observed the unintentional formation of GaAs layers under MnAs nanostructures owing to gas etching effects by Mn precursors during the direct MnAs growth on GaAs (111)B substrates. Desorption of Si atoms from the substrates, in particular, in the case of mask pattern (I), i.e., from the substrate surfaces outside $100 \times 100 \mu\text{m}^2$ square regions, occurred as well possibly owing to the gas etching effects by Mn precursors. This leaded to the Si incorporation occasionally into MnAs NDs, and then, MnAs alloy with approximately 17% of Si atoms was formed on NDs. All these possible discussions suggest that mask pattern (II) of SiON is effective to prevent unintentional reactions of Mn atoms with Si substrates for growing MnAs NDs with a high degree of uniformity.

4.3 Conclusion

We reported on SA-MOVPE and structural characterization results of magnetic MnAs NDs after the AlGaAs NP buffer growth on Si (111) substrates using multiple types of mask materials and designs, which were mask patterns (I) and (II) of SiO₂ and SiON. The results of structural characterizations showed that two key issues, which were the unintentional growth of MnSi alloy in Si substrates and MnAs alloy with approximately 17% of Si atoms on NDs, were typically observed in the case of Si substrates with mask pattern (I) of SiO₂. On the other hand, these two key issues are not observed in the case of Si substrates with mask pattern (II) of SiON. These results suggested that mask pattern (II) of SiON was effective to prevent the unintentional reactions of Mn atoms with Si substrates for growing MnAs NDs with a high degree of uniformity.

Bibliography

- [1] R. Horiguchi, S. Hara, M. Iida, and K. Morita, Selective-area growth of magnetic MnAs nanodisks on Si (111) substrates using multiple types of dielectric masks, *J. Cryst. Growth* **507**, 226 (2019).
- [2] S. Ikeda, K. Miura, H. Yamamoto, K. Mizunuma, H. D. Gan, M. Endo, S. Kanai, J. Hayakawa, F. Matsukura, H. Ohno, A perpendicular-anisotropy CoFeB-MgO magnetic tunnel junction, *Nat. Mater.* **9**, 721 (2009).
- [3] M. Yamanouchi, A. Jander, P. Dhagat, S. Ikeda, F. Matsukura, H. Ohno, Domain structure in CoFeB thin films with perpendicular magnetic anisotropy, *IEEE Magn. Lett.* **2**, 3000304 (2011).
- [4] D. D. Djayaprawira, K. Tsunekawa, M. Nagai, H. Maehara, S. Yamagata, N. Watanabe, 230% room-temperature magnetoresistance in CoFeB/MgO/CoFeB magnetic tunnel junctions, *Appl. Phys. Lett.* **86**, 092502 (2005).
- [5] K. Yakushiji, T. Saruya, H. Kubota, A. Fukushima, T. Nagahama, S. Yuasa, K. Ando, Ultrathin Co/Pt and Co/Pd superlattice films for MgO-based perpendicular magnetic tunnel junctions, *Appl. Phys. Lett.* **97**, 232508 (2010).

- [6] S. Sugahara, M. Tanaka, Tunneling magnetoresistance in fully epitaxial MnAs/AlAs/MnAs ferromagnetic tunnel junctions grown on vicinal GaAs (111)B substrates, *Appl. Phys. Lett.* **80**, 1969 (2002).
- [7] P. N. Hai, M. Yokoyama, S. Ohya, M. Tanaka, Spin polarized tunneling in III-V-based heterostructures with a ferromagnetic MnAs thin film and GaAs:MnAs nanoclusters, *Physica E* **32**, 416 (2006).
- [8] L. Thomas, S.-H. Yang, K.-S. Ryu, B. Hughes, C. Rettner, D.-S. Wang, C.-H. Tsai, K.-H. Shen, S. S. P. Parkin, Racetrack memory: a high-performance, low-cost, non-volatile memory based on magnetic domain walls, in: Proceedings of the 2011 International Electron Devices Meeting (IEDM 2011), December 5-7, 2011, Washington, DC, 24.2.1.
- [9] A. J. Annunziata, M. C. Gaidis, L. Thomas, C. W. Chien, C. C. Hung, P. Chevalier, E. J. O' Sullivan, J. P. Hummel, E. A. Joseph, Y. Zhu, T. Topuria, E. Delenia, P. M. Rice, S. S. P. Parkin, W. J. Gallagher, Racetrack memory cell array with integrated magnetic tunnel junction readout, in: Proceedings of the 2011 International Electron Devices Meeting (IEDM 2011), December 5-7, 2011, Washington, DC, 24.3.1.
- [10] R. W. De Blois, D. S. Rodbell, Magnetic first-order phase transition in single-crystal MnAs, *J. Appl. Phys.* **34**, 1101 (1963).

- [11] S. Hara, D. Kawamura, H. Iguchi, J. Motohisa, T. Fukui, Self-assembly and selective-area formation of ferromagnetic MnAs nanoclusters on lattice-mismatched semiconductor surfaces by MOVPE, *J. Cryst. Growth* **310**, 2390 (2008).
- [12] M. T. Elm, S. Hara, Transport properties of hybrids with ferromagnetic MnAs nanoclusters and their potential for new magnetoelectronic devices, *Adv. Mater.* **26**, 8079 (2014).
- [13] S. Ito, S. Hara, T. Wakatsuki, T. Fukui, Magnetic domain characterizations of anisotropic-shaped MnAs nanoclusters position-controlled by selective-area metal-organic vapor phase epitaxy, *Appl. Phys. Lett.* **94**, 243117 (2009).
- [14] S. Hara, K. Komagata, Selective-area growth and magnetic reversals of ferromagnetic nanoclusters on semiconducting substrate for magnetic logic applications, *Phys. Status Solidi B* **252**, 1925 (2015).
- [15] Y. Saito, T. Inokuchi, M. Ishikawa, H. Sugiyama, T. Marukame, T. Tanamoto, Spin-based MOSFET and its applications, *J. Electrochem. Soc.* **158**, H1068 (2011).
- [16] T. Suzuki, T. Sasaki, T. Oikawa, M. Shiraishi, Y. Suzuki, K. Noguchi, Room-temperature electron spin transport in a highly doped Si channel, *Appl. Phys. Express* **4**, 023003 (2011).
- [17] S. Oertel, J. Hübner, M. Oestreich, High temperature electron spin relaxation in bulk GaAs, *Appl. Phys. Lett.* **93**, 132112 (2008).

- [18] T. Wakatsuki, S. Hara, S. Ito, D. Kawamura, T. Fukui, Growth direction control of ferromagnetic MnAs grown by selective-area metal-organic vapor phase epitaxy, *Jpn. J. Appl. Phys.* **48**, 04C137 (2009).
- [19] S. Sakita, S. Hara, M. T. Elm, P. J. Klar, Selective-area growth and magnetic characterization of MnAs/AlGaAs nanoclusters on insulating Al₂O₃ layers crystallized on Si (111) substrates, *Appl. Phys. Lett.* **108**, 043108 (2016).
- [20] R. Horiguchi, S. Hara, and M. Iida, Magnetic domain structure and domain wall analysis of ferromagnetic MnAs nanodisks selectively-grown on Si (111) substrates for spintronic applications, *J. Appl. Phys.* **124**, 153905 (2018).
- [21] E. Sánchez, M. T. Deluigi, G. Castellano, Mean atomic number quantitative assessment in backscattered electron imaging, *Microsc. Microanal.* **18**, 1355 (2012).
- [22] K. Kanaya, S. Okayama, Penetration and energy-loss theory of electrons in solid targets, *J. Phys. D* **5**, 43 (1972).
- [23] W. A. P. Claassen, J. Bloem, The nucleation of CVD silicon on SiO₂ and Si₃N₄ substrates: I. The SiH₄-HCl-H₂ system at high temperatures, *J. Electrochem. Soc.* **127**, 194 (1980).
- [24] R. F. de Boer, R. Boom, A. R. Miedema, Enthalpies of formation of liquid and solid binary alloys based on 3d metals: II alloys of chromium and manganese, *Physica B+C* **113**, 18 (1982).

- [25] A. Shukia, A. D. Pelton, Thermodynamic assessment of the Al-Mn and Mg-Al-Mn systems, *J. Phase Equilib. Diffus.* **30**, 28 (2009).

Chapter 5

Characterization of magnetic domain structure and domain wall analysis in MnAs nanodisks selectively-grown on Si (111) substrates

This chapter describes the experimental and analytic results on magnetic domain and domain wall structures of MnAs nanodisks (NDs) on AlGaAs nanopillar buffers selectively grown on Si (111) substrates partially covered with dielectric SiO_2 thin film mask patterns using selective-area metal-organic vapor phase epitaxy. The results on the size dependence of the magnetic domain structure in MnAs NDs investigated by magnetic force microscopy show that a single domain is predominant in the MnAs NDs with an area of approximately $4 \times 10^4 \text{ nm}^2$ or less. It is also indicated that in the NDs with an area of approximately $6 \times 10^4 \text{ nm}^2$ or more multiple domains, in particular, two magnetic domain structures with a 180° domain wall are predominant. In addition, in the case of NDs with multiple domains, not only Néel walls but also Bloch walls are possibly formed, according to the detailed analyses of the magnetic force microscope images obtained. In addition, we report on the applied external magnetic field, \mathbf{B} , dependence of a magnetic domain structure and magnetization switching in MnAs NDs. The results on the \mathbf{B} dependence of magnetic domain structures observed by magnetic force microscopy show that the ratio, or percentage, of a single magnetic domain is minimized at $\mathbf{B} = -1.5 \text{ kG}$ in the NDs with an area of $4 \times 10^4 \text{ nm}^2$ or smaller, although the decrease to the minimum of the ratio is markedly small in the case of the NDs with an area of $4 \times 10^4 \text{ nm}^2$ or larger at $\mathbf{B} = -0.5 \text{ kG}$. The angle distribution of magnetization directions shows that the magnetization directions markedly tend to be parallel to the ridge directions of the hexagonal NDs, i.e., distribute in steps of approximately

60 degrees corresponding to the magnetic easy axes of the hexagonal NiAs-type crystal structure. The results suggest that the magnetic domains and coercive force can be tuned by controlling the MnAs ND size. (This chapter is described mainly based on our previous studies in Refs. 1 and 2.)

5.1 Introduction

Recently, device performance has been improved by the miniaturization of electronic devices in conventional Si complementary metal-oxide semiconductor (CMOS)-based integrated circuits. However, because of the physical limitation on device dimensions and the increase of power consumption, a realization of electronic devices based on new functions and operating principles is required. A so-called nanospintronic device has been one of the most promising candidates among such newly-functionalized electronic devices [3, 4]. In particular, magnetic tunnel junctions (MTJs) in combination with semiconducting materials are highly expected to create such nanospintronic devices because of large magnetoresistance effects and zero stand-by power consumption [5–7]. In addition, spin-transfer-torque-switching metal-oxide semiconductor field-effect transistors (STS-MOSFETs) using MTJ electrodes as source and drain electrodes, and racetrack-type memory cell arrays fabricated on Si substrates with MTJ read elements and CMOS-FETs have been proposed and intensively investigated [8–10]. Among the MTJs in combination with semiconducting materials, intensive studies on the MTJ structures using MnAs and III-V compound semiconductors have been reported [6, 7]. A huge magnetoresistance up to 100,000% has been demonstrated in the MTJs with granular GaAs:MnAs hybrid nanomaterials system consisting of ferromagnetic MnAs nanoclusters embedded in semiconducting GaAs layers [7]. Such a MTJ structure has been mainly fabricated by conventional top-down-type

microfabrication technologies. However, in the fabrication of such devices in nanometer scale, these conventional approaches may possibly result in deterioration in device performance owing to process-induced damages and a relatively poor size-uniformity.

To elude such possible problems, we have developed a bottom-up-type fabrication method, which is based on selective-area metal-organic vapor phase epitaxy (SA-MOVPE), of ferromagnetic MnAs nanostructures on semiconducting GaAs (111)B and Si (111) substrates [1, 2, 11–17]. This technique enables us to control the size, density, position, and shape of nanostructures without any process-induced damage and contamination for the fabrication of nanospintronic devices such as magnetic memories created by MTJs using ferromagnetic MnAs nanostructures. For example, the vertical-type MTJs are fabricated by lithography processes after the deposition of oxide interlayers such as MgO and Al₂O₃, and ferromagnetic thin films on the MnAs NDs grown by our SA-MOVPE. For the lateral-type MTJs, we believe that the use of elongated MnAs ND composites is promising, as demonstrated on GaAs (111)B substrates in our previous study [13]. In general, the magnetic domain structure depends on the size and shape of the magnetic nanomaterials and nanostructures. We have investigated the selective-area growth and characterized the structural properties of ferromagnetic MnAs ND structures after the growth of AlGaAs nanopillar (NP) buffers on Si (111) substrates using multiple types of mask materials and designs in Chapter 4 and Ref. 16. In this chapter, therefore, we characterize and analyze the magnetic domains and domain walls in ferromagnetic MnAs NDs. Moreover, we report an applied external magnetic field dependence of magnetic domain structures and magnetization switching in ferromagnetic MnAs NDs at room temperature in detail. We believe that the results obtained in the current work lead to the control in the magnetic domain structures and a magnetization direction by tuning the ND size on Si substrates.

5.2 Experimental procedures

The sample preparation process for the MnAs NDs used in the current work is described in Chapter 2 and 4. To be brief, we formed the MnAs NDs after the selective-area growth of AlGaAs NP buffers on Si (111) substrates covered with a 30-nm-thick SiO₂ mask pattern, in which the dielectric SiO₂ thin film is removed in part to form periodically arranged circular openings within 100 x 100 μm² square regions. Here, the SiO₂ thin film mask pattern with these circular openings prohibits the growth of both the AlGaAs NP buffers and the MnAs NDs. Eventually, we obtain the periodical arrays of single heterojunctions between a MnAs ND and an AlGaAs NP buffer on Si substrates. For the magnetic domain characterization of NDs, we summarize the complete magnetic field and temperature history of the samples in the current work as follows: During the MnAs growth and the cooling down process after the growth, our samples were possibly exposed to alternating magnetic fields generated by the radiofrequency (RF) coil of the heater used in our metal-organic vapor phase epitaxy system. (Other possibility of stray magnetic fields is geomagnetism, since the reactor of our growth system is made of glass.) The alternating magnetic fields by the RF coil were decreased to zero with decreasing gradually the substrate temperature from the growth temperature of 800°C for the growth of MnAs NDs to room temperature (i.e., at 25°C, or 298 K, in the air-conditioned clean room). Therefore, an equivalent process decreasing temperature and magnetic fields to the demagnetization protocol was carried out after the growth of MnAs NDs. And then, all the samples had been stored in the air-conditioned clean room at room temperature before the measurements. Hereafter, we call this condition of the samples as “as-grown condition” at room temperature in the current work. We estimated the size of MnAs NDs using backscattered electron (BSE) observations by scanning electron microscopy, SU-8010 system, Hitachi High-Tech. The BSE imaging is sensitive to solid

compositions of the observed material because the BSE emission increases with increasing mean atomic number of the material [18]. The acceleration voltage dependence of the BSE images was analyzed to estimate roughly the thickness of the MnAs NDs on the AlGaAs NP buffers. For the magnetic domain characterization of the NDs, magnetic force microscopy (MFM) in a Nanoscope IIIa system, Digital Instruments, was performed at room temperature using a high-resolution-type MFM tip of Si coated with a Co/Cr alloy (Bruker MESP-HR10). To investigate the detailed magnetic switching behavior in the NDs in this current work, a magnetic domain structure was investigated before and after applying an external magnetic field, \mathbf{B} , using a conventional stand-alone electromagnet. The \mathbf{B} was applied approximately along the direction perpendicular to the orientation flat of a Si (111) wafer. However, owing to the visual alignments between the \mathbf{B} and the substrate edge directions, the \mathbf{B} directions, or the angles, in the current work may possibly include a misalignment of ± 3 degrees at most. No external magnetic field was applied during the MFM measurements.

5.3 Results and discussion

5.3.1 Structural characterization of MnAs nanodisks

For the size estimation of the MnAs NDs, first, we carried out BSE observations. Figures 5-1(a) and 5-1(b) show the dependence of top view images of MnAs NDs grown on AlGaAs NP buffers on the acceleration voltage for the BSE observations. In the case of an acceleration voltage of 0.5 kV, we observe a relatively bright image contrast in the ND marked by “A” (hereafter, it is referred to as ND-A) and a darker image contrast in the ND marked by “B” (ND-B) than the image contrast in ND-A, as shown in Fig. 5-1(a). BSE images are highly sensitive to the solid

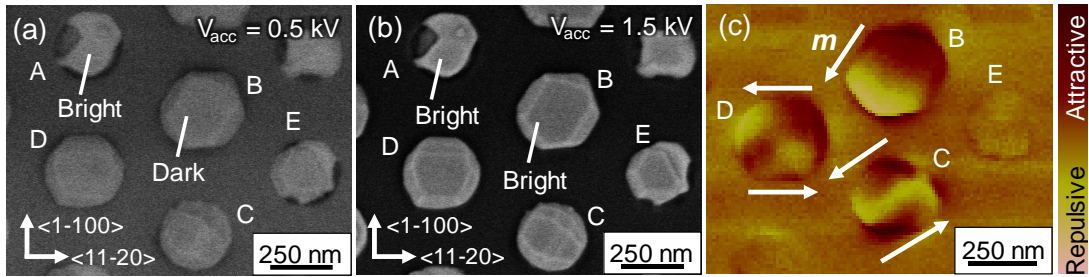


Figure 5-1. Acceleration voltage dependence of BSE images of MnAs NDs on AlGaAs NP buffers: (a) 0.5 and (b) 1.5 kV. In (a), a relatively bright image contrast of ND-A and an image contrast of ND-B darker than the one of ND-A are observed. In (b), almost no significant difference in the image contrasts between ND-A and ND-B is observed. (c) MFM image of the corresponding MnAs NDs. The MFM observations were carried out at room temperature without any application of an external magnetic field. Most of the MnAs NDs show a spontaneous magnetization. A single magnetic domain is observed in ND-B, and multiple magnetic domains are observed in ND-C and ND-D. The white arrows in (c) indicate the directions of the magnetic moments (\mathbf{m}) in the NDs. No well-defined contrast is observed in the MFM image of ND-E.

composition of a material since the BSE emission increases with increasing the mean atomic number of the material [18]. Since the mean atomic number of AlGaAs is larger than that of MnAs, BSE images of the AlGaAs NP buffers should be brighter than those of the MnAs NDs. Therefore, we conclude that the dark and bright image contrasts are due to MnAs NDs and AlGaAs NP buffers grown under the MnAs NDs, respectively. Increasing the acceleration voltage for the BSE images to 1.5 kV, almost no significant difference in the image contrasts between ND-A and ND-B are observed, i.e., the image contrast of ND-B became almost the same as that of ND-A, as shown in Fig. 5-1(b). The penetration length of electrons depends on an acceleration voltage of electrons in scanning electron microscopy. Therefore, in the case of an acceleration voltage of 1.5 kV, the bright image contrasts observed in most of the positions, where the MnAs NDs are located, are mainly due to the AlGaAs NP buffers grown under the MnAs NDs, as shown in Figs. 5-1(a) and 5-1(b). (However, no MnAs ND but only the AlGaAs NP buffer was grown

actually in “ND-A”, finally judging from the BSE and MFM analyses in Fig. 5-1.) The penetration length of electrons into MnAs NDs was calculated to be approximately 14 nm at 1.0 kV and 27 nm at 1.5 kV using the equation given in Ref. 19. Therefore, we roughly estimate a MnAs ND thickness of 20 nm in the observed NDs. In the result in Chapter 4 and Ref. [16], the thickness of MnAs NDs grown on Si (111) substrates covered with SiON mask patterns under the same growth conditions was estimated to be approximately 10 nm by transmission electron microscopy (TEM). The thickness estimated from the TEM images for a comparable structure is smaller than that roughly estimated by the BSE imaging, but of the same order of magnitude. It is difficult to estimate the thickness of MnAs NDs by AFM since the measured thickness is the total thickness of a MnAs ND and an AlGaAs NP buffer. However, the mean thickness of some MnAs NDs partially grown on AlGaAs NP buffers, which were unintentionally and occasionally observed, was estimated to be 22.2 nm by AFM. This mean thickness estimated by AFM is in good agreement with the above-mentioned thickness estimated from the BSE images, i.e., approximately 20 nm. From electron beam diffraction measurements by TEM, we conclude that the crystallographic structure of all MnAs NDs observed in the current work is a hexagonal NiAs-type structure, and that the <0001> direction of hexagonal NiAs-type MnAs is parallel to both the <111>B direction of the zinc-blende-type AlGaAs NP buffers and the <111> direction of the diamond-type Si substrates.

5.3.2 Characterization of Magnetic domain and domain wall analysis of MnAs nanodisks under as-grown condition

First of all, we conducted MFM observations at room temperature without the

application of an external magnetic field to characterize the magnetic domain structure of the MnAs NDs. Figure 5-1(c) shows an MFM image of the MnAs NDs shown in Figs. 5-1(a) and 5-1(b). Well-defined image contrasts are observed for most of the NDs. Therefore, the MnAs NDs in Fig. 5-1 show a spontaneous magnetization at room temperature. A single magnetic domain is markedly confirmed in ND-B in Fig. 5-1(c). In addition, multiple magnetic domains are observed in the NDs marked by “C” (ND-C) and “D” (ND-D). The white arrows in the image represent the directions of the magnetic moment (\mathbf{m}) in the MnAs NDs. On the other hand, no well-defined contrast is observed in the MFM images for some of the NDs, although relatively dark contrasts are confirmed in the BSE images owing to the MnAs NDs, e.g., as in the case of the ND marked by “E” (ND-E) in Fig. 5-1. These results may suggest that the MnAs NDs with ferromagnetic hexagonal α -phase (α -MnAs, NiAs-type) and paramagnetic orthorhombic β -phase (β -MnAs, MnP-type) are possibly coexisted in the current work. A MnAs bulk crystal shows a first-order structural phase transition between MnP-type and NiAs-type MnAs at temperatures between 317 and 319 K [20, 21]. Some researchers have actually observed a phase coexistence of MnP-type and NiAs-type MnAs in the case of MnAs thin films hetero-epitaxially grown on GaAs (001) [22–25] and (111)B substrates [26]. In Ref. 25, this phase coexistence was observed at the temperature from 283 to 313 K. In addition, the enhancement of Curie-temperature up to 340 K was observed in the case of hexagonal NiAs-type MnAs nanostructures grown on InGaAs layers on InP (111)B substrates, possibly owing to the incorporation of a small fraction of Ga atoms into the nanostructures [14]. The possible existence of MnP-type MnAs NDs has thus far not yet been excluded even in the current work, although all the MnAs NDs with well-defined crystal facets observed by TEM were a ferromagnetic hexagonal α -phase [16]. Based on the results of Ref. 25, however, a phase coexistence of MnP-type and NiAs-type MnAs should be observed for the NDs in the current work at room temperature, although we observed that the Curie-temperature of

MnAs nanostructures was enhanced in our previous study, Ref. 14. Therefore, the NDs, such as ND-E, without any well-defined image contrast could have the MnP-type crystal structure.

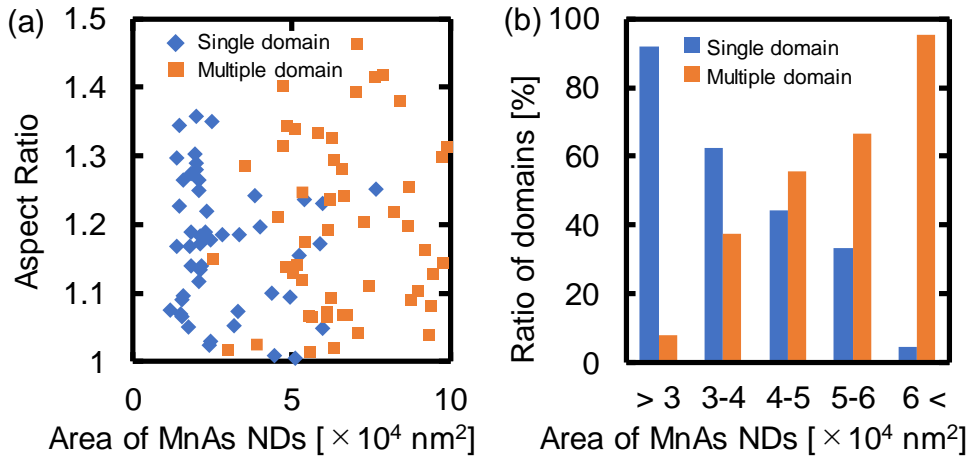


Figure 5-2. Size dependence of magnetic domain structures of MnAs NDs. (a) The two-dimensional distributions of single and multiple magnetic domains as a function of area and an aspect ratio of MnAs NDs. The aspect ratios were defined as the ratios of the longest length of $<11-20>$ direction divided by the shortest length of $<1-100>$ direction of MnAs NDs. (b) The ratio of domain structures as a function of area of MnAs NDs. The number of data is 100. Single magnetic domain structures were mainly observed in the NDs with $4 \times 10^4 \text{ nm}^2$ or less, and multiple magnetic domain structures were observed in the NDs with $6 \times 10^4 \text{ nm}^2$ or more.

Figure 5-2 shows the size dependence of the magnetic domain structures in our MnAs NDs. The aspect ratios and the areas of the MnAs NDs were estimated from the top views of the BSE images. The aspect ratio is defined as the ratio of the length along the $<11-20>$ direction divided by that along the $<1-100>$ direction of the MnAs NDs. The number of analyzed NDs is 100 in Fig. 5-2(b). Single and multiple magnetic domains are observed in most of the MnAs NDs with an area of $3 \times 10^4 \text{ nm}^2$ or less and $6 \times 10^4 \text{ nm}^2$ or more, respectively. In the small NDs, the domain wall energy generated by dividing a single domain into two magnetic domains is higher than the magneto-static energy in a single domain state. On the other hand, in the NDs with a

comparatively large size, this domain wall energy is lower than the magneto-static energy in a single domain state. Therefore, it is reasonable that single and multiple domain structures are formed in the small and large NDs, respectively.

A 180° domain wall is mainly confirmed for the multiple domain structures, such as ND-C and ND-D shown in the schematic illustrations of Figs. 5-3(a) and 5-3(b). In the part corresponding to the domain wall of ND-C illustrated in Fig. 5-3(a), strong repulsive forces between the magnetic moment at the possible domain wall center and the magnetization of the MFM tip, i.e., large effective stray magnetic fields in the direction perpendicular to the substrate plane, are observed, as shown in Fig. 5-3(c). On the other hand, in the case of ND-D illustrated in Fig. 5-3(b), the observed repulsive forces at the possible domain wall center was not as strong as those in the case of ND-C shown in Fig. 5-3(d). In MnAs thin films with Bloch walls, the image contrast pattern similar to the one obtained in ND-C was observed by other research groups [27]. Therefore, it is highly possible that ND-C and ND-D exhibit Bloch and Néel walls, respectively. Subsequently, we estimated the domain wall widths of ND-C and ND-D from the contrast patterns, or contrast distributions, of the MFM images shown in Fig. 5-1. The estimation of the domain wall widths from the MFM image contrast has been reported by several other groups [28–30]. In the papers published, in general including the articles, Refs. 28 to 30, the domain wall widths, i.e., Bloch or Néel wall widths, were estimated as the widths between the maximum and minimum peaks of the MFM image contrast generated by the stray magnetic fields from the magnetizations in two magnetic domains. Therefore, it seemed that these estimated widths were overestimated to some extent because the actual domain wall width should not be the distance between two magnetic domain centers, i.e., not between the maximum and minimum peaks of the MFM image contrast. In addition, the stray magnetic fields away from the sample surfaces were detected and

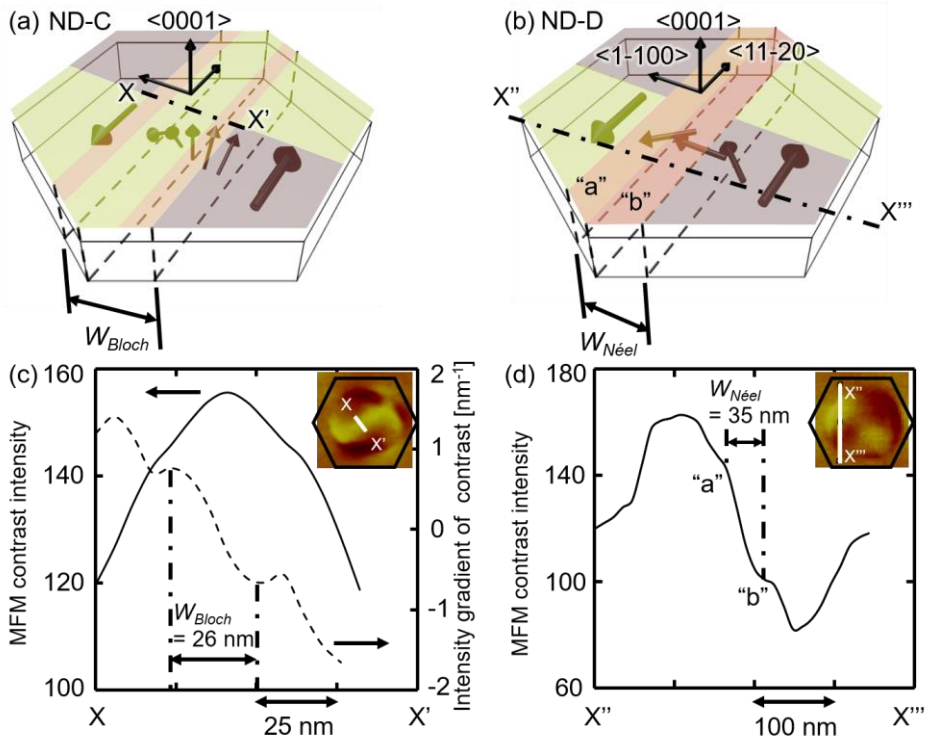


Figure 5-3. Schematic illustrations of the magnetic domain structures and the domain walls assumed by the contrasts of MFM images in (a) ND-D and (b) ND-C. Bloch and Néel wall widths were estimated to be approximately 26 nm for ND-D and 35 nm for ND-C, respectively, by the image contrasts and the intensity gradient of contrasts in the MFM images of (c) ND-D and (d) ND-C.

imaged by the MFM tip as the tip was somewhat lifted up from the sample surfaces during the MFM scans. However, the experimental domain wall widths estimated from the MFM observation results were well-described by the simulated domain wall widths, as discussed in Ref. 28. Therefore, the overestimation of a domain wall width does not seem to be a major problem for magnetic structures on the micrometer scale [28, 29] since the tip height during the MFM observations is probably negligible compared to the size of the magnetic microstructure. However, we believe that the overestimation of the domain wall width in MFM images may become a major issue to take care of for structures on the nanometer scale. In the current work, the stray magnetic

fields from the MnAs NDs were detected at a tip height of 30 nm during all the MFM observations. The radius of the NDs estimated from the MFM images is approximately 7 to 10% larger than that estimated from the AFM images. When estimating the Bloch wall width, W_{Bloch} , in ND-C, we assumed that the perpendicular component of the magnetic moments changes according to a sine curve along the Bloch wall. Thus, the intensity gradient of the image contrasts should change according to a sine curve along the Bloch wall, as observed in the calculated intensity gradient indicated by the dashed line in Fig. 5-3(c). From this, a width of approximately 26 nm is estimated as the Bloch wall width, i.e., $W_{Bloch} = 26$ nm. Subsequently, we also estimated the width of the Néel wall, $W_{Néel}$, in ND-D. Two kinks marked by “a” and “b” are observed in the intensity distribution curve of image contrasts, as shown in Fig. 5-3(d). These two kinks, a and b, can be attributed to additional repulsive and attractive forces detected by the MFM tip, which are generated by the sum of all the effective magnetic moments during the in-plane rotation in the Néel wall. Therefore, we determined the width between the two kinks, resulting in an estimated Néel wall width of approximately 35 nm, i.e., $W_{Néel} = 35$ nm. When neglecting the influence of the stray field energy density, the theoretical wall widths for Bloch and Néel walls in MnAs can be calculated using the following equations, Eqs. (5-1) and (5-2), given in Ref. 31:

$$W_{Bloch} = \sqrt{2}\pi \sqrt{\frac{A}{K_{<0001>}}} , \quad (5-1)$$

$$W_{Néel} = \sqrt{2}\pi \sqrt{\frac{A}{K_{<1-100>}}} , \quad (5-2)$$

where A is the exchange stiffness constant, and $K_{<0001>}$ and $K_{<1-100>}$ are the anisotropy energies in the $<0001>$ and $<1-100>$ directions of hexagonal NiAs-type MnAs, respectively. With the reported values, $A = 1.0 \times 10^{-6}$ erg/cm [23], $K_{<0001>} = 5.2 \times 10^6$ erg/cm³ [32], and $K_{<1-100>} = 2.2 \times 10^6$ erg/cm³ [32], the theoretical domain wall widths are calculated to be approximately 19 nm for

the Bloch wall and 30 nm for the Néel wall. Thus, the calculated domain wall widths are to some extent smaller than those estimated by the contrasts in MFM images, but, of the same order of magnitude.

In general, the formation of a Néel wall is preferred in thin films since the magneto-static energy increases with decreasing film thickness for magnetic moments oriented along the direction perpendicular to the plane surface. To discuss the probability for the formation of Bloch and Néel walls in the NDs, we calculated the domain wall energies. Here, we assumed that the shape of the NDs was discoid for simplification. The thickness dependence of the Bloch and Néel wall energies calculated in Ni-Fe thin films was reported by other research groups [33–35]. As reported by Middelhoek,[31] the energies per unit areas for a Bloch wall, γ_{Bloch} , and a Néel wall, $\gamma_{Néel}$, were obtained by adding the exchange, the anisotropy, and the stray field energy densities, i.e.,

$$\gamma_{Bloch} = A \left(\frac{\pi}{W_{Bloch}} \right)^2 W_{Bloch} + \frac{K_{<0001>}}{2} W_{Bloch} + \frac{\pi W_{Bloch}^2 M_s^2}{W_{Bloch} + D}, \quad (5-3)$$

$$\gamma_{Néel} = A \left(\frac{\pi}{W_{Néel}} \right)^2 W_{Néel} + \frac{K_{<1-100>}}{2} W_{Néel} + \frac{\pi W_{Néel} D M_s^2}{W_{Néel} + D}, \quad (5-4)$$

where M_s is the saturation magnetization, and D is the thickness of the thin films, i.e., MnAs NDs in the current work. Using Eqs. (5-3) and (5-4), the energies of the Bloch and Néel walls were calculated, and the results are plotted in Fig. 5-4. Here, $M_s = 400$ emu/m³ [23] was used to calculate the domain wall energies. The calculations reveal that the energy of a Bloch wall is equal to that of a Néel wall when the thickness of MnAs NDs is approximately 22 nm, which is in good agreement with the thickness estimated from the BSE images, i.e., approximately 20 nm. Therefore, we concluded that it is reasonable to observe not only MnAs NDs with Néel walls but also with Bloch walls in the current work. These results suggest that the magnetic domains and

the type of domain walls can be tuned by the size of the MnAs NDs.

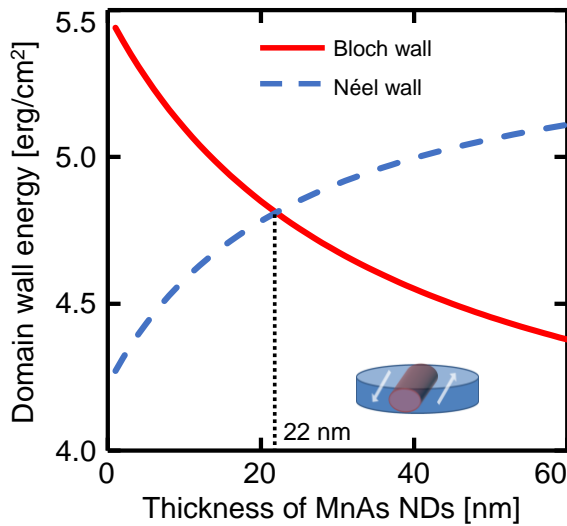


Figure 5-4. Calculated wall energy density per unit area of domain walls as a function of the MnAs thickness. The Bloch wall energy was equal to the Néel wall energy at the ND thickness of approximately 22 nm, which was nearly consistent with the thickness of 20 nm roughly estimated from the acceleration voltage dependence of BSE images of MnAs NDs.

5.3.3 Applied magnetic field dependence of magnetic domain structure and magnetization switching of MnAs nanodisks

Figure 5-5 shows the applied magnetic field, \mathbf{B} , dependence of the ratio, or percentage (%), of a single magnetic domain in MnAs NDs. Here, the ratio of a single magnetic domain is defined as the percentage when we divide the number of NDs with a single magnetic domain by the number of NDs with a well-defined image contrast, i.e., including multiple magnetic domains, markedly observed by MFM at each of the \mathbf{B} . In order to characterize the ratio of a single magnetic domain in Fig. 5-5, the number of NDs which we observed a well-defined image contrast by MFM

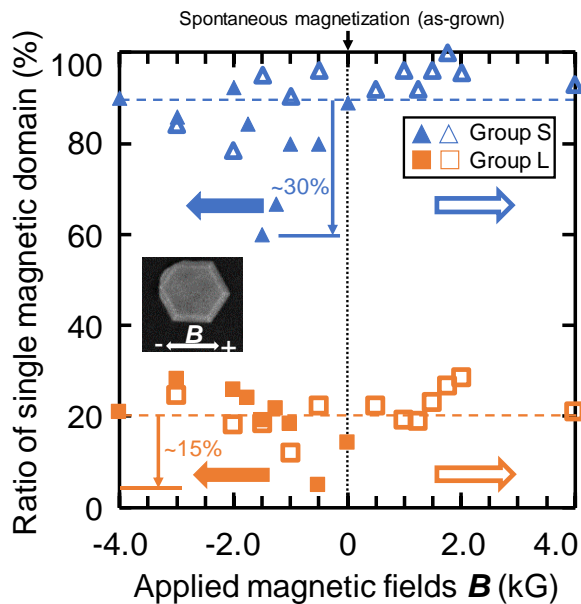


Figure 5-5. Applied external magnetic field, \mathbf{B} , dependence of the ratio, or percentage, of a single magnetic domain observed in MnAs NDs. The open triangle and closed triangles are for the NDs with an area of $4 \times 10^4 \text{ nm}^2$ or smaller, i.e., Group S, and the open square and closed squares for the NDs with an area of $4 \times 10^4 \text{ nm}^2$ or larger, i.e., Group L. The solid triangles and squares indicate the results obtained for the sweep direction of the \mathbf{B} applied from 0 to -4.0 kG, and the open triangles and squares indicate those from -4.0 to +4.0 kG. The dashed lines are a guide to the eye. The data on the dotted line are for a spontaneous magnetization under as-grown condition. The inset shows a BSE image of a MnAs ND on an AlGaAs NP buffer. The white two-head arrow in the inset indicates the directions of an applied magnetic fields, \mathbf{B} . The ratio of a single magnetic domain is markedly minimized at $\mathbf{B} = -1.5 \text{ kG}$ in the case of Group S.

was from 44 to 100. The \mathbf{B} direction is as shown in a BSE image of one of the NDs as the inset of Fig. 5-5. The B , first, was applied at room temperature from -0.5 to -4.0 kGauss (kG), and, next, from -4.0 to +4.0 kG. At each of the data points in Fig. 5-5, MFM observations were performed. In Chapter 5.3.2, we have characterized the size dependence of a magnetic domain structure and analyzed domain walls in MnAs NDs under as-grown condition as shown in Fig. 5-2. From these results, single magnetic domain structures were mainly observed in the NDs with an area of $4 \times 10^4 \text{ nm}^2$ or smaller, and multiple magnetic domain structures were predominant in the NDs with an area of $6 \times 10^4 \text{ nm}^2$ or larger. Therefore, in the current work, we define two categories to easily

characterize and discuss an applied \mathbf{B} dependence of magnetic domain structures and magnetization switching in the NDs: (a) the NDs with an area of $4 \times 10^4 \text{ nm}^2$ or smaller is referred to as “Group S”, and (b) the NDs with an area of $4 \times 10^4 \text{ nm}^2$ or larger is referred to as “Group L”. As indicated by the dashed lines as a guide to the eye in Fig. 5-4, the ratios of a single magnetic domain were mostly around 90% and 20% for Group S and Group L, respectively. In the case of Group S, during the sweeping of \mathbf{B} from 0 to -1.5 kG, the marked decrease in the ratio of a single magnetic domain was observed, in particular, at $\mathbf{B} = -1.5 \text{ kG}$. The ratio of a single magnetic domain decreased from 90% to the minimum value of 60% at $\mathbf{B} = -1.5 \text{ kG}$. At the \mathbf{B} applied from -1.5 to -4.0 kG, the marked increase in the ratio was observed again to the maximum value of approximately 90%. This result suggests the mean coercive force of MnAs NDs in Group S is estimated approximately to be 1.5 kOe, as 1 G is approximately 1 Oe in the air. At the \mathbf{B} applied from -4.0 to +4.0 kG, no significant decrease in the ratio of a single magnetic domain was observed. On the other hand, in the case of Group L, during the sweeping of \mathbf{B} from 0 to -4.0 kG, the decrease in the ratio of a single magnetic domain was not as marked as that in Group S. However, the ratio of a single magnetic domain decreased from approximately 20% to the minimum value of 5% at $\mathbf{B} = -0.5 \text{ kG}$. This also means that the possible mean coercive force of MnAs NDs in Group L was estimated approximately to be 0.5 kOe. The mean coercive force of MnAs NDs in Group S, is larger than that of NDs in Group L. It is reasonable that the enhancement of the coercive forces possibly arises from the decrease in the size of MnAs NDs, since an increase of the coercive forces with decreasing a grain size was reported also for other magnetic materials system [36,37]. At the \mathbf{B} applied from 0 to -0.5 kG in Group L and from 0 to -1.5 kG in Group S, we surly confirmed by MFM observations that this decrease in the ratio of a single magnetic domain was markedly due to the change in the magnetic domain structures from a single to a multiple magnetic domain.

Next, we investigate the change in a magnetic domain structure from the viewpoints of the initial magnetization direction under as-grown condition and the shape of NDs. Figure 5-6 shows typical MFM images of the NDs, in which the change from a single magnetic domain to a multiple magnetic domain was observed. As shown in the inset of Fig. 5-6(a), first, the ND marked by “F” (ND-F) has a low aspect ratio of 1.03, i.e., a small shape anisotropy, and the magnetization in the opposite direction to the applied \mathbf{B} direction. And then, the change in a magnetic domain structure was observed under the condition of $\mathbf{B} = -1.0$ kG, as shown in Fig. 5-6(a). Here, the aspect ratio of NDs is defined as the ratio of the length parallel to the magnetization direction divided by that perpendicular to the magnetization direction of the NDs. It was reported that the

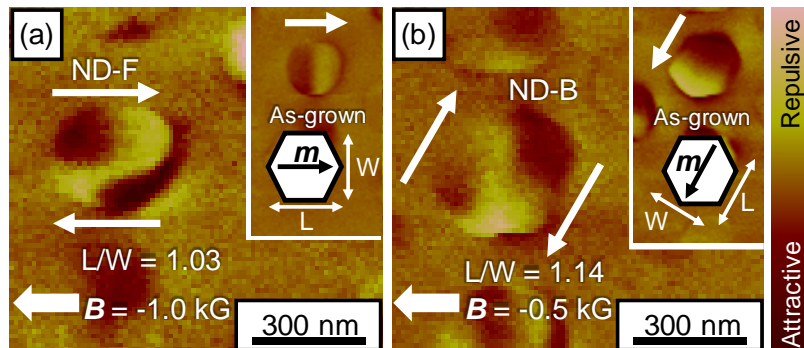


Figure 5-6. Applied external magnetic field, \mathbf{B} , dependence of magnetic domain structures in MnAs NDs. The change from a single magnetic domain to a multiple magnetic domain in the NDs at (a) $\mathbf{B} = -1.0$ and (b) -0.5 kG is observed. Insets in (a) and (b) show the magnetization directions under as-grown condition and the definition of the aspect ratio. The aspect ratio of NDs is defined as the ratio of the length parallel to the magnetization direction divided by that perpendicular to the magnetization direction of the NDs, i.e., L/W , as illustrated in the insets. The images also show the aspect ratio dependence of magnetic domains in the NDs. ND-F has low aspect ratio of 1.03, i.e., a small shape anisotropy, and the magnetization in opposite direction to the \mathbf{B} direction. ND-B has a relatively high aspect ratio of 1.14, i.e., a larger shape anisotropy than that of ND-F, and the magnetization with a component in the same direction as the \mathbf{B} direction. ND-F and ND-B are categorized in Group L. No dependence of magnetic domain switching on the aspect ratio of the NDs has been observed.

nucleation of domain walls occurred at the defects on the particle surfaces, which leaded to the change in a magnetic domain structure, in the case of Fe-Nd-B magnets [38]. In the TEM result shown in Chapter 4, the dislocations, whose mean period was estimated to be approximately 3.6 nm, were observed in one or two monolayers of the MnAs layers at the interfaces between the MnAs NDs and the AlGaAs NP buffers [16]. Therefore, the change in a magnetic domain structure from a single to a multiple magnetic domain would be due to the domain wall creation by applying \mathbf{B} , since these dislocations could act as centers for the domain wall nucleation in the current work. As shown in the inset of Fig. 5-6(b), second, the ND-B has a relatively high aspect ratio of 1.14, i.e., a larger shape anisotropy than that of ND-F, and the magnetization with a component in the same direction as the applied \mathbf{B} direction. And then, the change in a magnetic domain structure was observed at $\mathbf{B} = -0.5$ kG, as shown in Fig. 5-6(b). The results obtained in Fig. 5-6, therefore, would suggest that the change in a magnetic domain structure is independent of the initial magnetization direction under as-grown condition and the shape of NDs with the aspect ratios of 1.03 and 1.14. In the case of lateral MnAs wire described later in Chapter 6, a single magnetic domain was observed in a lateral MnAs wire structure with the length of 2.1 μm and the width of 360 nm, i.e., a relatively large aspect ratio of 5.83, grown by the selective-area growth on GaAs (111)B substrates. It is supposed that a magnetic domain structure should be influenced by the shape of NDs, in general. However, almost no shape dependence of a magnetic domain structure was observed in the current case of NDs with a relatively small aspect ratio. A possible explanation for the change in a magnetic domain structure in the current work would not only be the domain wall creation but also the increase in a magneto-static energy. In the NDs, such as ND-E after the application of $\mathbf{B} = -0.5$ kG in Fig. 5-6, we occasionally observed a multiple magnetic domain, even when the NDs under as-grown condition (as shown in the case of ND-B in the inset of Fig. 5-6) had a single magnetic domain with the magnetization almost aligned to

the \mathbf{B} direction. Even in the case of a single magnetic domain observed by MFM, there would possibly be a small number of tiny magnetic domains with a magnetic moment, \mathbf{m} , in the opposite direction to the magnetization direction observed by MFM, since the magnetization of the NDs, which is detected as a stray magnetic field from the NDs by MFM, represents the sum of all the magnetic moments in magnetic domains in the NDs. If there would be such small pieces of magnetic domains in the NDs, such as ND-B, under as-grown condition with a magnetic moment in the opposite direction to the magnetization direction observed by MFM, a magneto-static energy in the NDs should be increased when the magnetic moments in the small pieces of magnetic domains in the NDs are oriented along the applied \mathbf{B} direction. In ferromagnetic materials, in general, the volume of materials and the magnitude of magnetization can be changed when the state of magnetic moments is changed by applying the \mathbf{B} , which is known as a magnetostriction effect. The change in a magnetic domain structure was observed mainly for the NDs with an area of $4 \times 10^4 \text{ nm}^2$ or larger, i.e., Group L. Therefore, the magnetic domain structure in such a relatively large NDs under as-grown condition could be unstable. (For example, for the NDs with an area between 4×10^4 and $5 \times 10^4 \text{ nm}^2$, the ratio of a single magnetic domain was estimated to be approximately 44% under as-grown condition in Fig. 5-2.) Several reports insist that the increase in the sample length caused by a magnetostriction effect is observed in the MnAs and MnAsSb alloy systems [39–42], and that the amount of a magnetostriction effect depends on the relationship between the crystal and magnetization orientations in MnAs and $\text{La}_{0.8}\text{Sr}_{0.2}\text{CoO}_3$ alloys [41, 42]. However, the sample strain observed in Ref. [40] was estimated to be only $10^{-3}\%$ at most even at $\mathbf{B} = 4.0 \text{ kOe}$. Therefore, we do not believe that a magnetostriction effect in the material system of MnAs could be a major contribution to the increase in a magneto-static energy in the MnAs NDs. During all the MFM observations in the current work, the temperatures of the samples could be changed, since we confirmed that the room temperature during the MFM

observations gradually increased from 20 to 30°C (i.e., from 293 K in the beginning to 303 K at last during the MFM observations for a long time) at most. As mentioned above, a MnAs thin film grown on GaAs (001) substrates show a first-order structural phase transition between MnP-type and NiAs-type MnAs at temperatures between 283 and 313 K [22, 25]. As reported by some other researchers [39, 43, 44], the magnetization and the susceptibility of MnAs drastically changed around the temperatures between 20 and 30°C, which eventually means that a magneto-static energy could markedly be changed. This might be the most presumable and possible explanation to understand the phenomena observed in a magnetic domain structure in Fig. 5-6 in the current work. We repeated the observation of the same ND after switching the magnetization direction of an MFM tip in order to ensure that the obtained image contrasts are due to a magnetic response from the ND. During the MFM measurements using the tip with an opposite magnetized direction at a certain temperature between 20 and 30°C, we have never observed, at least, the transition from a single to multiple magnetic domain. However, further experiments in detail are required to draw a conclusion for the phenomena observed in a magnetic domain structure in Fig. 5-6.

At the \mathbf{B} applied from +0.5 to +4.0 kG, as shown in Fig. 5-5, no significant decrease in the ratio of a single magnetic domain was observed neither in Group S nor Group L. Therefore, we, next, investigate the angle distribution of the magnetization directions in MnAs NDs with a single magnetic domain between $\mathbf{B} = +0.5$ and +4.0 kG. Figure 5-7 summarizes the two-dimensional distributions of the angle, θ , of magnetization directions, \mathbf{m} , in the NDs as a function of the area of NDs for $\mathbf{B} = +0.5$, +1.5, and +2.0 kG. The insert of Fig. 5-7 shows the schematic definition of θ . We observed the difference in the strength of \mathbf{B} for magnetization switching even in the case of NDs with a similar size, or area. This difference may be due to dislocation

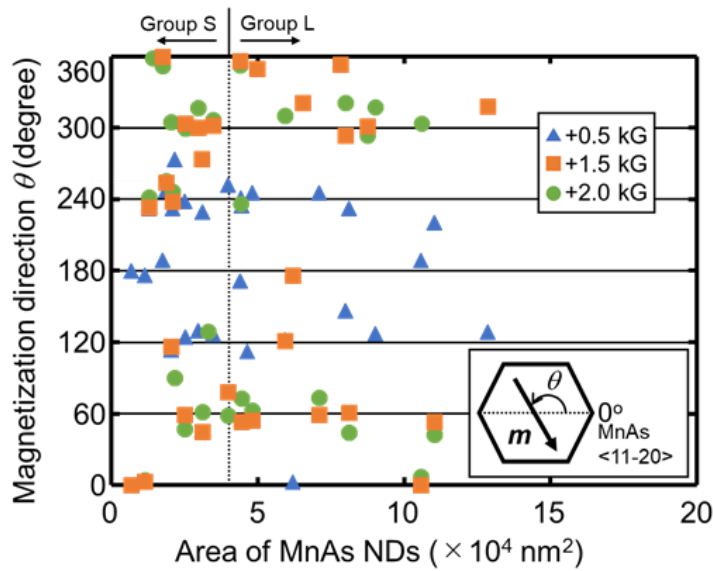


Figure 5-7. Applied magnetic field, B , dependence of an angle of a magnetization direction in MnAs NDs at the B applied from +0.5 to +2.0 kG for both Group S and Group L. The dotted line represents the boundary between Group S and Group L. The inset shows the schematic definition of an angle of magnetization direction, θ . The angle of $\theta = 0$ degree is corresponding to the <11-20> orientation of MnAs NDs.

distribution at the interfaces between the MnAs and AlGaAs layers, since it has been observed by other research groups that a domain wall motion is hindered by dislocations, and that a magnetic domain wall is pinned by them [45–47]. The effect of dislocations on a magnetic domain wall has also been theoretically reported [45, 46]. The influence of dislocations on a domain wall motion has also been investigated in iron by high voltage Lorentz microscopy [47]. In the current work, the two-dimensional locations of dislocations at the interfaces between MnAs and the AlGaAs layers are supposed to be different between the NDs. Therefore, this difference in the strength of B for magnetization switching even in the case of NDs with a similar size, or area, could be due to the difference in the two-dimensional location of dislocations at the interfaces between MnAs and the AlGaAs layers. In addition, the two-dimensional locations of dislocations at the interfaces after the application of B might be slightly changed even by a small amount of magnetostriction

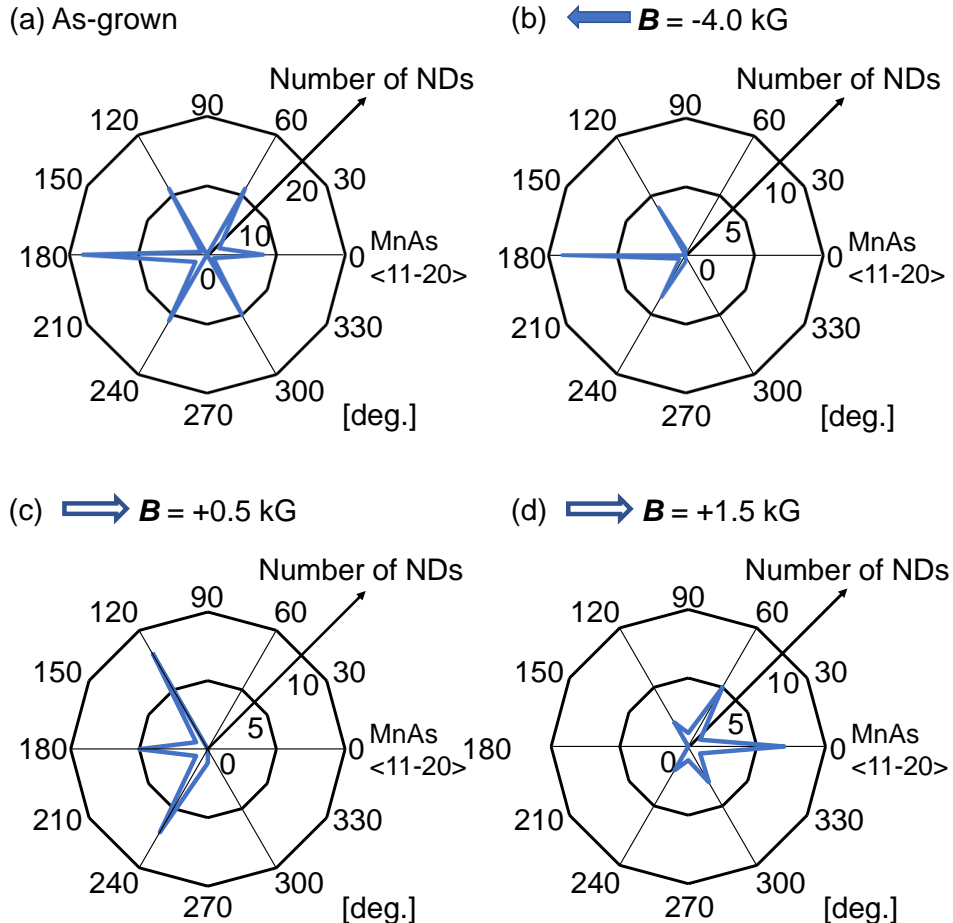


Figure 5-8. The radar charts of the number of NDs in terms of the angle of magnetization directions in steps of 30 degrees, which are summarized for \mathbf{B} = (a) 0 (i.e., as-grown condition), (b) -4.0, (c) +0.5, and (d) +1.5 kG. The angle of $\theta = 0$ degree is corresponding to the $<11\bar{2}0>$ orientation of MnAs NDs. At $\mathbf{B} = +1.5$ kG, the magnetization switching is observed in some of the NDs, indicating that the mean coercive force is estimated approximately to be 1.5 kOe.

effects. The change in two-dimensional locations of dislocations possibly leads to no significant decrease in the ratio of a single magnetic domain between the \mathbf{B} applied from -4.0 to +4.0 kG, since a domain wall motion could be hindered, and since a domain wall could be pinned by dislocations. In addition, as shown in Fig. 5-8, we plot the radar charts for the number of NDs in terms of the angle of magnetization directions in steps of 30 degrees, summarizing the results in Figs. 5-2 and 5-7. When plotting the data, the NDs with an angle of magnetization directions

between the steps of 30 degrees (i.e., not in the exact steps of 30 degrees) were included in the closest one among the angles in steps of 30 degrees. Under as-grown condition, the magnetization direction for most of the NDs was oriented at the angles of 0, 60, 120, 180, 240, or 300 degrees as shown in Fig. 5-8(a). This result suggests that the magnetization directions in the as-grown MnAs NDs was not influenced by the stray magnetic fields, which means that our demagnetization protocol is effective. At $B = -4.0$ kG, the magnetization direction for most of the NDs was oriented at the angles of 120, 180, or 240 degrees as shown in Fig. 5-8(b), i.e., the most of the NDs has the magnetization with a component in the same direction as the applied B direction. At $B = +0.5$ kG, the magnetization direction for most of the NDs was oriented at the angles of 120, 180, or 240 degrees, i.e., no magnetization switching was observed as shown in Fig. 5-8(c). At $B = +1.5$ kG, however, the magnetization direction for most of the NDs was oriented at the angles of 0, 60, or 300 degrees as shown in Fig. 5-8(d), i.e., the marked magnetization switching was observed. In the case of a NiAs-type MnAs crystal, the <11-20> orientation is known as an easy magnetization axis, i.e., an a-axis, and the <0001> orientation is known as a hard magnetization axis, i.e., a c-axis [48,49]. In the current study, as shown in the BSE image for one of the NDs in the inset of Fig. 5-5, hexagonal MnAs NDs with well-defined crystal facets were mostly observed. For the hexagonal NiAs-type crystal structure, the ridge directions of hexagons correspond to the <11-20> orientation, i.e., an easy magnetization axis [16]. Therefore, it is reasonable that the magnetization directions are distributed approximately in steps of 60 degrees, which correspond to three equivalent easy magnetization axes. Even when $B = -4.0$ kG was applied to the NDs, the magnetization direction has not be completely aligned to the applied B direction. Therefore, it may be required to introduce a shape magnetic anisotropy for device applications using the NDs for controlling the magnetization directions in the NDs.

These results obtained in this paper suggest that the magnetic domains and coercive force can be tuned by controlling the MnAs ND size. We believe that the results on magnetization switching in MnAs NDs is crucial to realize the MTJs with the NDs on Si (111) substrates and/or our proposed planar-type magnetic logic devices consisting of elongated MnAs nanostructure composites selectively grown on GaAs (111)B substrates [13].

5.4 Conclusion

We characterized magnetic domain and domain wall structures of MnAs NDs on AlGaAs NP buffers selectively grown on Si (111) substrates partially covered with dielectric SiO_2 thin film mask patterns for SA-MOVPE. The results on the size dependence of magnetic domain structures in MnAs NDs observed by MFM showed that a single domain was predominant in the MnAs NDs with an area of approximately $4 \times 10^4 \text{ nm}^2$ or less. It was also indicated that multiple domains, in particular, the two magnetic domain structures with a 180° domain wall were predominant in the NDs with an area of approximately $6 \times 10^4 \text{ nm}^2$ or more. In addition, in the case of NDs with multiple domains, the NDs not only with Néel wall but also with Bloch wall were possibly formed, judging from the detailed analyses of the MFM images obtained. Moreover, we characterized the applied external magnetic field, \mathbf{B} , dependence of a magnetic domain of MnAs NDs. From the results on the \mathbf{B} dependence of a magnetic domain structure in the MnAs NDs, the ratio of a single magnetic domain was minimized at $\mathbf{B} = -1.5 \text{ kG}$ in the NDs with an area of $4 \times 10^4 \text{ nm}^2$ or smaller, although the decrease to the minimum of the ratio was markedly small in the case of the NDs with an area of $4 \times 10^4 \text{ nm}^2$ or larger at $\mathbf{B} = -0.5 \text{ kG}$. In addition, the angle distribution of magnetization directions showed that the magnetization directions were mostly

parallel to the ridge directions of the hexagonal NDs, i.e., distributed in steps of approximately 60 degrees corresponding to the magnetic easy axes of the hexagonal NiAs-type crystal structure. These results suggested that the magnetic domains and a coercive force can be tuned by controlling the MnAs ND size.

Bibliography

- [1] R. Horiguchi, S. Hara, and M. Iida, Magnetic domain structure and domain wall analysis of ferromagnetic MnAs nanodisks selectively-grown on Si (111) substrates for spintronic applications, *J. Appl. Phys.* **124**, 153905 (2018).
- [2] R. Horiguchi, S. Hara, K. Suzuki, and M. Iida, Magnetization switching depending on magnetic fields applied to ferromagnetic MnAs nanodisks selectively-grown on Si (111) Substrates, *AIP Advances* **124**, 153905 (2020).
- [3] H. Ohno, Making nonmagnetic semiconductors ferromagnetic, *Science* **281**, 951 (1998).
- [4] B. T. Jonker, Progress toward electrical injection of spin-polarized electrons into semiconductors, *Proc. IEEE* **91**, 727 (2003).
- [5] S. Sugahara and M. Tanaka, Tunneling magnetoresistance in fully epitaxial MnAs/AlAs/MnAs ferromagnetic tunnel junctions grown on vicinal GaAs (111)B substrates, *Appl. Phys. Lett.* **80**, 1969 (2002).
- [6] P. N. Hai, M. Yokoyama, S. Ohya, and M. Tanaka, Spin polarized tunneling in III–V-based heterostructures with a ferromagnetic MnAs thin film and GaAs:MnAs nanoclusters, *Physica E* **32**, 416 (2006).

- [7] P. N. Hai, S. Ohya, M. Tanaka, S. E. Barnes, and S. Maekawa, Electromotive force and huge magnetoresistance in magnetic tunnel junctions, *Nature* **458**, 489 (2009).
- [8] Y. Saito, T. Inokuchi, M. Ishikawa, H. Sugiyama, T. Marukame, and T. Tanamoto, Spin-based MOSFET and its applications, *J. Electrochem. Soc.* **158**, H1068 (2011).
- [9] L. Thomas, S.-H. Yang, K.-S. Ryu, B. Hughes, C. Rettner, D.-S. Wang, C.-H. Tsai, K.-H. Shen, and S. S. P. Parkin, Racetrack memory: a high-performance, low-cost, non-volatile memory based on magnetic domain walls, in Proceedings of the 2011 International Electron Devices Meeting (IEDM 2011) (IEEE 2011), 24.2.1 (2011).
- [10] A. J. Annunziata, M. C. Gaidis, L. Thomas, C. W. Chien, C. C. Hung, P. Chevalier, E. J. O' Sullivan, J. P. Hummel, E. A. Joseph, Y. Zhu, T. Topuria, E. Delenia, P. M. Rice, S. S. P. Parkin, and W. J. Gallagher, Racetrack memory cell array with integrated magnetic tunnel junction readout, in Proceedings of the 2011 International Electron Devices Meeting (IEDM 2011) (IEEE 2011), 24.3.1 (2011).
- [11] S. Hara, D. Kawamura, H. Iguchi, J. Motohisa, and T. Fukui, Self-assembly and selective-area formation of ferromagnetic MnAs nanoclusters on lattice-mismatched semiconductor surfaces by MOVPE, *J. Cryst. Growth* **310**, 2390 (2008).
- [12] M. T. Elm and S. Hara, Transport properties of hybrids with ferromagnetic MnAs nanoclusters and their potential for new magnetoelectronic devices, *Adv. Mater.* **26**, 8079 (2014).

- [13] S. Ito, S. Hara, T. Wakatsuki, and T. Fukui, Magnetic domain characterizations of anisotropic-shaped MnAs nanoclusters position-controlled by selective-area metal-organic vapor phase epitaxy, *Appl. Phys. Lett.* **94**, 243117 (2009).
- [14] M. T. Elm, C. Michel, J. Stehr, D. M. Hofmann, P. J. Klar, S. Ito, S. Hara, and H.-A. Krug von Nidda, Comparison of the magnetic properties of GaInAs/MnAs and GaAs/MnAs hybrids with random and ordered arrangements of MnAs nanoclusters, *J. Appl. Phys.* **107**, 013701 (2010).
- [15] S. Hara and K. Komagata, Selective-area growth and magnetic reversals of ferromagnetic nanoclusters on semiconducting substrate for magnetic logic applications, *Phys. Status Solidi B* **252**, 1925 (2015).
- [16] R. Horiguchi, S. Hara, M. Iida, and K. Morita, Selective-area growth of magnetic MnAs nanodisks on Si (111) substrates using multiple types of dielectric masks, *J. Cryst. Growth* **507**, 226 (2019).
- [17] R. Horiguchi, H. Kato, K. Kabamoto, R. Kodaira, and S. Hara, Analyses of magnetization switching and magnetic domains in lateral MnAs nanowires in combination with structural characterization, *Jpn. J. Appl. Phys.* **56**, 06GH05 (2017).
- [18] E. Sánchez, M. T. Deluigi, G. Castellano, Mean atomic number quantitative assessment in backscattered electron imaging, *Microsc. Microanal.* **18**, 1355 (2012).

- [19] K. Kanaya, S. Okayama, Penetration and energy-loss theory of electrons in solid targets, *J. Phys. D* **5**, 43 (1972).
- [20] J. B. Goodenough and J. A. Kafalas, High-pressure study of the first-order phase transition in MnAs, *Phys. Rev.* **157**, 389 (1967).
- [21] F. Ishikawa, K. Koyama, K. Watanabe, and H. Wada, Field induced structural transformation in MnAs, *Jpn. J. Appl. Phys.* **42**, L918 (2003).
- [22] V. M. Kaganer, B. Jenichen, F. Schippen, W. Braun, L. Däweritz, and K. H. Ploog, Strain-mediated phase coexistence in MnAs heteroepitaxial films on GaAs: An x-ray diffraction study, *Phys. Rev. B* **66**, 045305 (2002).
- [23] R. Engel-Herbert, T. Hesjedal, J. Mohanty, D. M. Schaadt, and K. H. Ploog, Magnetization reversal in MnAs films: Magnetic force microscopy, SQUID magnetometry, and micromagnetic simulations, *Phys. Rev. B* **73**, 104441 (2006).
- [24] L. Däweritz, L. Wan, B. Jenichen, C. Herrmann, J. Mohanty, A. Trampert, and K. H. Ploog, Thickness dependence of the magnetic properties of MnAs films on GaAs (001) and GaAs (113)A: Role of a natural array of ferromagnetic stripes, *J. Appl. Phys.* **96**, 5056 (2004).
- [25] A. K. Das, C. Pampuch, A. Ney, T. Hesjedal, L. Däweritz, R. Koch, and K. H. Ploog, Ferromagnetism of MnAs studied by heteroepitaxial films on GaAs (001), *Phys. Rev. Lett.* **91**,

087203 (2003).

[26] R. Engel-Herbert, T. Hesjedal, D. M. Schaad, L. Däweritz, and K. H. Ploog, Micromagnetic properties of MnAs(0001)/GaAs(111) epitaxial films, *Appl. Phys. Lett.* **88**, 052505 (2006).

[27] J. Mohanty, T. Hesjedal, T. Plake, M. Kästner, L. Däweritz, and K. H. Ploog, Variable-temperature micromagnetic study of epitaxially grown MnAs films on GaAs (001), *Appl. Phys. A* **77**, 739 (2003).

[28] Y. Nozaki, K. Matsuyama, T. Ono, and H. Miyajima, Micromagnetic structure analysis of head-on-head-type 180° domain wall in submicron size Co wires, *Jpn. J. Appl. Phys.* **38**, 6282 (1999).

[29] T. G. Pokhil and B. M. Moskowitz, Magnetic domains and domain walls in pseudo-single-domain magnetite studied with magnetic force microscopy, *J. Geophys. Res.* **102**, 22681 (1997).

[30] C. T. Hsieh, J. Q. Liu, and J. T. Lue, Magnetic force microscopy studies of domain walls in nickel and cobalt films, *Appl. Surf. Sci.* **252**, 1899 (2005).

[31] S. Middelhoek, Domain walls in thin Ni–Fe films, *J. Appl. Phys.* **34**, 1054 (1963).

[32] K. H. Ploog, L. Däweritz, R. Engel-Herbert, and T. Hesjedal, Micromagnetic properties of MnAs-on-GaAs(001) films, *Phys. Status Solidi B* **203**, 3574 (2006).

- [33] L. Néel, Bloch wall energy of thin films, Compt. Rend. **241**, 533 (1955).
- [34] H.-D. Dietze and H. Thomas, Bloch- und Néel-Wände in dünnen ferromagnetischen Schichten, Z. Physik **163**, 523 (1961).
- [35] R. E. Behringer and R. S. Smith, The influence of demagnetization and anisotropy energy on Bloch wall thickness and coercive force in thin films, J. Franklin Inst. **272**, 14 (1961).
- [36] F. Phfeifer and C. Radloff, Soft magnetic Ni-Fe and Co-Fe alloys-some physical and metallurgical aspects, J. Magn. Magn. Mater. **19**, 190 (1980).
- [37] G. Herzer, Grain structure and magnetism of nanocrystalline ferromagnets, IEEE Trans. Magn. **25**, 3327 (1989).
- [38] R. Ramesh, G. Thomas, and B. M. Ma, Magnetization reversal in nucleation controlled magnets. II. Effect of grain size and size distribution on intrinsic coercivity of Fe-Nd-B magnets, J. Appl. Phys. **64**, 6416 (1988).
- [39] V. A. Chernenko, L. Wee, P. G. McCormick, and R. Street, Giant magnetoelastic response in MnAs, J. Appl. Phys. **85**, 7833 (1999).
- [40] H. J. Forsyth, I. R. Harris, B. Cockayne, and W. R. MacEwan, Magnetostrictive Behaviour Observed In MnAs And MnAs./sub 0.92/Sb/sub 0.08, in Proceedings of the 1993 IEEE

International Magnetics Conference (INTERMAG), DP-6 (1993).

- [41] H. J. Forsyth, I. R. Harris, B. Cockayne, and W. R. MacEwan, Magnetostrictive behaviour observed in MnAs/sub 0.92/Sb/sub 0.08/over the field range 0 to 850 kA/m, IEEE Trans. Magn. **29**, 3529 (1993).
- [42] K. Sato, K. Minagawa, M. Nakamura, T. Ichikawa, Y. Hara, K. Nakaoka, Y. Kobayashi, and K. Asai, Crystal orientation dependence of magnetostriction of twinned perovskite cobalt oxide, J. Alloy. Comp. **752**, 327 (2018).
- [43] M. E. G. Tilsley, N. A. Smith, B. Cockayne, L. R. Harris, P. A. Lane, P. E. Oliver, and P. J. Wright, Magnetic and electrical characteristics of MnAs films grown by metalorganic chemical vapour deposition, J. Alloy. Compd. **248**, 125 (1997).
- [44] R. Engel-Herbert and T. Hesjedal, Magnetic coupling of ferromagnetic stripe arrays: Analytical model for the α - β -phase coexistence regime of MnAs/GaAs(001), Phys. Rev. B **78**, 235309 (2008).
- [45] K. H. Pfeffer, Zur Theorie der Koerzitivfeldstärke und Anfangssuszeptibilität, Phys. Stat. Sol. **21**, 857 (1967).
- [46] D. C. Jiles, Czech. Dynamics of domain magnetization and the Barkhausen effect, J. Phys. **50**, 893 (2000).

- [47] R. A. Taylor, J. P. Jakubovics, B. Astié, and J. Degauque, Direct observation of the interaction between magnetic domain walls and dislocations in iron, *J. Magn. Magn. Mater.* **31**, 970 (1983).
- [48] F. Schippan, G. Behme, L. Daweritz, and K. H. Ploog, Magnetic structure of epitaxially grown MnAs on GaAs (001), *J. Appl. Phys.* **88**, 2766 (2000).
- [49] V. Garcia, M. Marangolo, M. Eddrief, and V. H. Etgens, Magnetization reversal and anomalous dependence of the coercive field with temperature in MnAs epilayers grown on GaAs, *Phys. Rev. B* **74**, 144402 (2006).

Chapter 6

Structural and magnetic domain characterization of lateral MnAs/AlGaAs nanowires selectively-grown on GaAs (111)B substrates

In this chapter, we describe the structural and the magnetic domain characterization of lateral MnAs/AlGaAs nanowires selectively grown on GaAs (111)B substrates. The lateral MnAs nanowires observed by backscattered and secondary electron microscopies have a high aspect ratio (i.e., 2.6 μm long and 360 nm wide) and well-defined crystal facets. The external magnetic field dependence in magnetic force microscopy observations of the lateral nanowires reveals that single and multiple magnetic domains were formed in the lateral nanowires. This study suggests that magnetic domains are tuned by the structural control of lateral nanowires. However, no magnetization switching is observed under a relatively high external magnetic field of 5.0 kG, which should be enough for the magnetization switching of the lateral nanowires, possibly owing to the magnetization switching of the magnetic force microscope tip itself used in this study during observations. (This chapter is described mainly based on our previous study in Ref. 1.)

6.1 Introduction

Recently, intensive activities addressing magnetic nanowires (NWs) have attracted considerable attention in the field of magneto-nanoelectronics and nanospintronics communities owing to, for example, the demonstration of magnetic memories and shift registers for the

electronic industries in the next generation [2–5]. These devices use current-driven magnetic domain wall motion. Some research groups reported on the control of domain wall motion by electric currents [6–9] as well as magnetic fields [10] in ferromagnetic NWs. Furthermore, other research groups have reported that the switching of the magnetization can be controlled by current-induced domain wall motion in ferromagnetic NWs [11] and diluted magnetic semiconductor layers [12]. The typical approach to realizing such magnetic NWs in the world is a top-down-type fabrication technique, which is typically based on etching processes after the thin film deposition of ferromagnetic metals. However, the performance of a device fabricated by these methods possibly deteriorates owing to process-induced damage and a relatively low size uniformity. To solve such a possible problem caused by device processes, we have proposed and demonstrated a bottom-up-type fabrication method for ferromagnetic nanoclusters (NCs) [13–15] and lateral NWs [16] on semiconducting substrates, for example, GaAs (111)B and Si (111) substrates, by selective-area metal-organic vapor phase epitaxy (SA-MOVPE). This technique enables us to control the size, density, position, and shape of the nanostructures without any process-induced damage and contamination. In our previous studies, we reported on the controllability of magnetic domains in the MnAs NCs grown by SA-MOVPE [17, 18]. By utilizing SA-MOVPE-grown MnAs NCs, we demonstrated angle-dependent magnetoresistance effects in various MnAs NC arrangements consisting of elongated NCs with a single magnetic domain [19]. Furthermore, in a system with two elongated MnAs NCs connected by nonmagnetic metal spacer layers, we observed abrupt jumps in magnetoresistance and a spin-valve-like behavior [20].

In our previous study, we selectively fabricated lateral MnAs NWs with a high aspect ratio after the AlGaAs buffer layer growth on a GaAs (111)B substrate [16]. We also observed

and analyzed the magnetic random telegraph noise of electrical resistance in the lateral NWs [21].

To achieve high performance and reliability in magnetic NW devices, the control of magnetic properties in lateral NW structures is crucial in the future on the way towards a practical use of the lateral NWs. In this work, therefore, for a high degree of size uniformity to control the magnetic properties of the lateral NWs, the detailed structural characterization of the lateral NWs by scanning electron microscopy (SEM) is presented. The analyses of the magnetization switching behavior and magnetic domains of the lateral NWs, in combination with the structural characterization results, are also described and discussed in this chapter.

6.2 Experimental procedures

The pretreatment of the substrate for growth is described in Chapter 3.2.3. We have developed and used the SA-MOVPE method for the fabrication of lateral MnAs NWs after the growth of AlGaAs buffer layers in the initial circular openings of 20-nm-thick SiO₂ mask layers deposited on GaAs (111)B substrates. The fabrication procedures for the lateral NWs used in this study were described and explained in detail elsewhere [16]. For the experiments indicated in this chapter, a relatively long lateral MnAs NW with well-defined crystal facets was chosen from the same sample used in a previous study [16]. For structural characterization, secondary electron images were observed by SEM (SU-8010, Hitachi High-Tech) to characterize the shape and surface morphologies of the lateral NWs. In addition to secondary electron imaging, we utilized backscattered electron (BSE) imaging by SEM since BSE imaging is sensitive to the solid compositions of the observed materials because the BSE emission increases with the mean atomic

number of materials [22]. It is much more effective to identify lateral MnAs NWs on AlGaAs buffer layers by BSE imaging in combination with the observation of crystal facets formed on the lateral NW surface by conventional secondary electron imaging. The acceleration voltage dependence of BSE images was characterized roughly to analyze the thickness of the MnAs layers of the lateral NWs. For the magnetic characterizations of lateral MnAs NWs, we used magnetic force microscopy (MFM) combined with atomic force microscopy (AFM) in a Nanoscope IIIa system, Digital Instruments, at room temperature and without any applied external magnetic field (B) during the observations. Before the MFM observations using the high-resolution MFM tip of Si coated with Co/Cr alloy materials (Bruker MESP-HR10), B of 2.0 to 5.0 kG was applied parallel to the lateral NWs on GaAs (111)B substrates using a conventional stand-alone electromagnet. The coercivity of the MFM tip used is 950 Oe according to the specification sheet published by Bruker AXS.

6.3 Results and discussion

6.3.1 Structural characterization of lateral MnAs/AlGaAs NWs by BSE imaging

Figure 6-1 shows the dependence of the top views of lateral MnAs NWs on the acceleration voltage of BSE images. At an acceleration voltage of 1.0 kV, first, as shown in Fig. 6-1(a), two regions with a relatively dark contrast, which were marked “A” and “C”, were observed. Hereafter, these two elongated structures along the <0-11> direction of the GaAs (111)B substrate are referred to as NW-A and NW-C. We also observed an area marked “B” with a contrast brighter than those of NW-A and NW-C between NW-A and NW-C. BSE images are

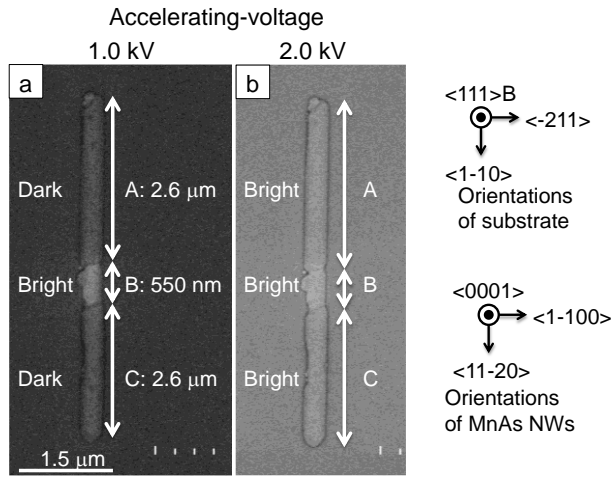


Figure 6-1. Acceleration voltage dependence of BSE images of lateral MnAs NWs: (a) 1.0 and (b) 2.0 kV. In (a), two relatively dark regions, i.e., NW-A and NW-C, are observed, and a brighter area, i.e., gap region B, than the two dark regions is confirmed between the two dark regions of NWs. In (b), almost no significant brightness difference among NW-A, gap region B, and NW-C is observed. The crystallographic relationship between a GaAs (111)B substrate and the lateral MnAs NWs is depicted below the BSE images.

highly sensitive to the solid composition of materials since BSE emission increases with the mean atomic number of materials [22]. In the current work, the mean atomic number of AlGaAs is larger than that of MnAs. Therefore, the BSE images from the AlGaAs buffer layers should be brighter than those from the MnAs layers in the lateral NWs. It was highly possible that the dark regions of NW-A and NW-C in Fig. 6-1(a) are attributable to MnAs layers in the NWs, and that the bright region between the NWs, i.e., the gap region marked B, is due to the AlGaAs buffer layers. Increasing the acceleration voltage for a BSE image to 2.0 kV, almost no significant difference in brightness among the A to C regions was observed, i.e., the brightness of NW-A and NW-C became almost the same as that of the gap region B in the image of Fig. 6-1(b). The penetration length of electrons depends on the acceleration voltage of electrons. Therefore, in the case of the acceleration voltage of 2.0 kV in Fig. 6-1(b), the bright image observed in the whole NW region including the A to C regions was mainly due to the AlGaAs buffer layers grown under

the MnAs layers in the initial mask openings on the substrate. The penetration length of electrons was calculated to be approximately 13 nm at 1.0 kV and 44 nm at 2.0 kV using the equation given in Ref. 23. Therefore, it was highly possible from the calculated penetration lengths that the MnAs layer thickness was approximately 40 nm in the observed lateral NW structure in Fig. 6-1. We also confirmed from the BSE image of Fig. 6-1(a) that NW-A was 2.6 μm in length, and that NW-C was 2.1 μm in length.

Figure 6-2 shows a bird's-eye view of a secondary electron image and a corresponding cross-sectional schematic illustration of the NWs observed in Fig. 6-1. We confirmed from the observed cross section of NW-C in Fig. 6-2(a) that the height and width of NW-C were measured to be 210 and 360 nm, respectively, as depicted in the illustration in Fig. 6-2(b). It seemed that NW-A had similar height and width to NW-C. In addition, we observed that well-defined crystal facets were formed as the top and sidewall facets of NW-A and NW-C. In our previous studies, for example, Ref. 24, we have grown comparable MnAs nanostructures on SiO_2 -masked GaAs (111)B substrates with initial periodical circular openings by SA-MOVPE. The structural

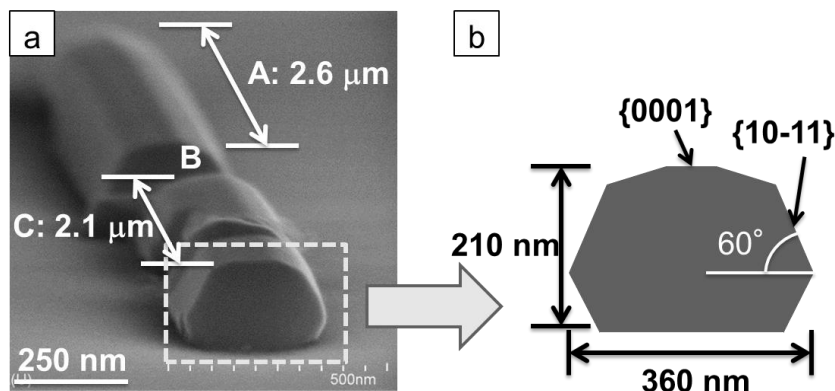


Figure 6-2. Bird's-eye view of secondary electron image by SEM and cross-sectional illustration of MnAs NWs with the measured length, height, and width of the NWs. The angle between top and sidewall facets was estimated to be 60 degrees.

characterizations using electron-beam diffraction measurements in combination with lattice image observations by transmission electron microscopy (TEM) revealed that the MnAs nanostructures had a hexagonal NiAs-type crystal structure [24]. Therefore, assuming that the MnAs layers of the lateral NWs have the same hexagonal NiAs-type crystal structure in the current work, which has been observed in all the comparable MnAs nanostructures [24], it was presumed that the {0001} facet of the NiAs-type crystal structure was formed as the top surface of the NWs, and that {10-11} ones were attributable to the tilted sidewall facets with an angle of 60 degrees with respect to the {0001} plane of the NWs, as illustrated in Fig. 6-2(b) and reported in Ref. 24.

6.3.2 Magnetization switching and magnetic domain analyses by MFM imaging

A MnAs bulk crystal shows the first-order structural phase transition between the paramagnetic orthorhombic β -phase (β -MnAs, MnP-type) and the ferromagnetic hexagonal α -phase (α -MnAs, NiAs-type) at temperatures of 317 - 319 K [25, 26]. It has been reported that the transition temperature from paramagnetism to ferromagnetism, i.e., the Curie-temperature (T_c), shifts owing to the change in exchange interaction between spins caused by strain effects in a crystal lattice [27–29]. The shift in T_c was observed not only in MnAs films [27, 28] but also in other material systems, for example, SrRuO₃ films [28]. In our previous studies, the hysteresis curves [30] at room temperature and the increased T_c of 340 K [31] were observed for the comparable samples of NiAs-type MnAs nanostructures grown on InGaAs layers by MOVPE. We have not determined the T_c of the lateral MnAs NWs in this study. A lattice mismatch between

the c-plane of MnAs and the {111}B plane of GaAs was calculated to be approximately 6.8% or slightly higher. (The Al contents of AlGaAs buffer layers used in this study were approximately 10 - 20% at most [32].) However, the analyses of electron diffraction patterns obtained by TEM (for example, in Ref. 18) showed that all the comparable MnAs nanostructures observed so far had the lattice constant of a NiAs-type MnAs bulk crystal, i.e., the MnAs nanostructures were completely relaxed on zinc-blende-type semiconducting layers, although it seemed that the lattice strain remained only in one or two monolayers of MnAs nanostructures near the interface between MnAs and semiconductors. Therefore, it was reasonable in this study that the lateral MnAs NWs were treated as a MnAs bulk crystal, i.e., no lattice strain was observed in almost all the layers in lateral MnAs NWs. We performed MFM at room temperature, i.e., around 293 - 298 K below the T_c (318 K) of a MnAs bulk crystal, after the application of external magnetic fields for the magnetic characterizations of the lateral MnAs NWs in the current study.

Figures 6-3(a) and 6-3(b) show the MFM images of the same NWs after the application of the external magnetic field of 2.0 kG parallel to the directions of thick white arrows in the images. In Fig. 6-3(a), the magnetizations along the applied magnetic field direction in NW-A and NW-C (represented by long and thin white arrows in the images) are observed. We found that NW-A, in particular, had a single magnetic domain, and that NW-C had multiple magnetic domains. However, after the application of the external magnetic field of 2.0 kG in the direction opposite to that in Fig. 6-3(a), no magnetization switching was observed, as shown in Fig. 6-3(b). The cross-sectional line profile of the lateral NWs observed by AFM is shown in Fig. 6-3(c) to clarify the magnetic domains formed in NW-A and NW-C. The height difference between the gap region B and NW-A was roughly estimated as 70 nm or more, which was slightly larger than the MnAs layer thickness of around 40 nm, estimated from the BSE images in Fig. 6-1, but on the

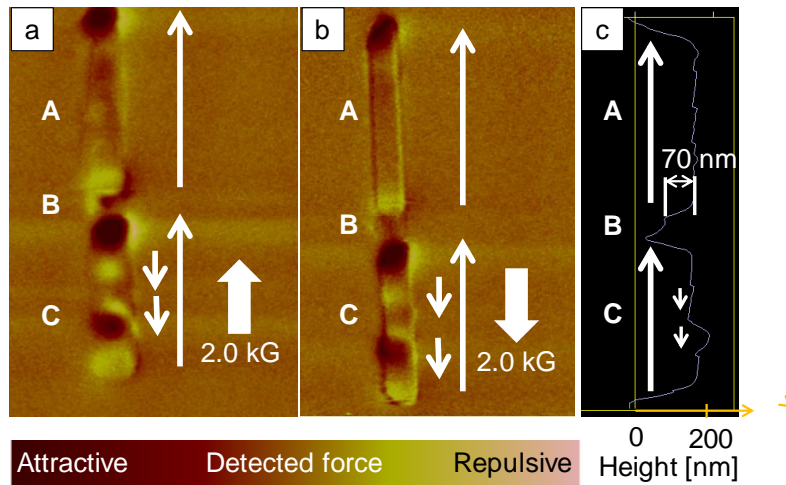


Figure 6-3. MFM images after the application of the external magnetic field of 2.0 kG in the directions (a) the same as and (b) opposite to the observed magnetization directions of the MnAs NWs at room temperature. In (a) and (b), the thick and white arrows represent the applied magnetic field directions, and the magnetization directions are oriented from bright to dark regions in the images, as indicated by the long and short thin white arrows. (c) Cross-sectional line profile of the MnAs NWs observed by AFM.

same order of magnitude. As shown in Figs. 6-2 and 6-3(c), the surface of NW-C was not flat, which might show that MnAs NW-C is polycrystalline. Therefore, judging from the profiles of NW-C, NW-C had also small magnetic domains on top, in which the magnetization directions were indicated by short and thin white arrows in Fig. 6-3. The magnetizations of these small magnetic domains on top and the main body of NW-C presumably have an antiparallel configuration.

Next, we characterized the magnetization switching behavior of the lateral NWs examined in Figs. 6-1 to 6-3. The external magnetic field was set to 3.0, 4.0, and 5.0 kG in this order from 2.0 kG used in Figs. 6-3(a) and 6-3(b), and the applied directions were the same as those in Figs. 6-3(a) and 6-3(b). However, no magnetization switching was observed even in the case of relatively high magnetic fields up to 5.0 kG applied in the directions opposite to the

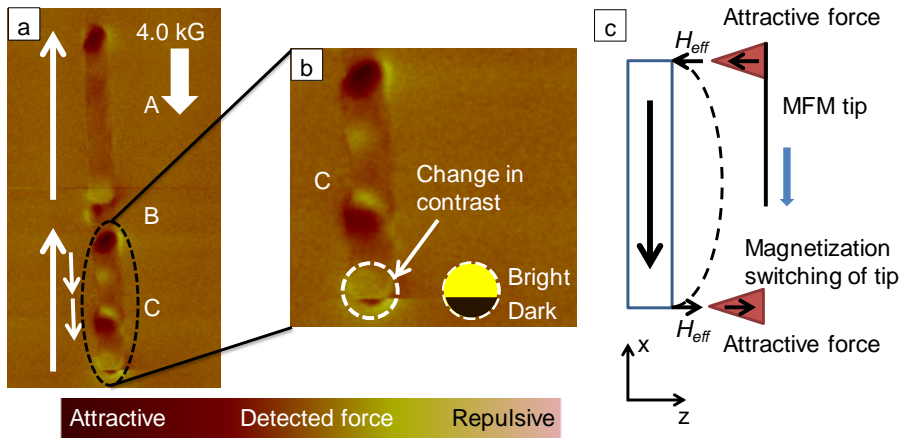


Figure 6-4. MFM images after the application of 4.0 kG in the direction opposite to the observed magnetization directions of NWs at room temperature: (a) Whole image and (b) highly magnified image for the sudden changes in the contrasts from bright to dark at one of the ends of NW-C. In (a), the thick and white arrow represents the applied magnetic field direction, and the magnetization directions are indicated by long and short thin white arrows. (c) Possible explanation for the magnetization switching of MFM tips themselves during the observations at one of the ends of NW-A and NW-C under the applied magnetic fields of 3.0 kG or more.

magnetization directions of NW-A and NW-C, as shown, for example, in the case of 4.0 kG in Fig. 6-4(a). (Other images, for example, for the applied external magnetic field of 5.0 kG, are not shown here.) To analyze this magnetization switching behavior, therefore, the coercivity of, for example, NW-A, was calculated. We used here the Stoner-Wohlfarth model to estimate the magnetic fields required for magnetization switching [33]. According to this model, the coercivity H_c can be calculated as

$$H_c = \frac{2K_u}{M_s} - NM_s \quad (6-1)$$

Where K_u is the uniaxial magnetic anisotropy constant, M_s is the saturation magnetization, and N is the effective demagnetization factor. From the calculations, the coercivity was estimated to be approximately 2200 Oe. Here, $K_u = 7.6 \times 10^6$ erg/cm³ [34], $M_s = 630$ emu/cm³ [35], and N was roughly approximated here as an ellipsoidal structure to use the demagnetization coefficient

determined in Ref. 36 to calculate the coercivity of NW-A, and NW-C. It was found from the rough calculation here that magnetization switching in NW-A should have been observed at the applied external magnetic fields of 3.0 kG or more when the relative permeability is assumed to be 1.0. No magnetization switching was actually observed in the NWs even when the external magnetic fields of 3.0 kG or more were applied, as shown in Fig. 6-4(a). When we applied the external magnetic fields of 3.0 kG or more, however, the sudden changes in the contrasts from bright to dark were detected during the observations at one of the ends of NW-A and NW-C under most of the applied magnetic fields of 3.0 kG or more, as seen in an example shown in Fig. 6-4(b). These sudden changes in the contrasts in the MFM images are unintentional and strange. In the MFM measurements, the MFM tips are magnetized to detect repulsive and attractive forces between stray magnetic fields from the NWs and MFM tips. Therefore, there is a possibility of magnetization switching of the MFM tips themselves during the observations at one of the ends of NW-A and NW-C under the applied magnetic fields of 3000 G or more, as illustrated in Fig. 6-4(c).

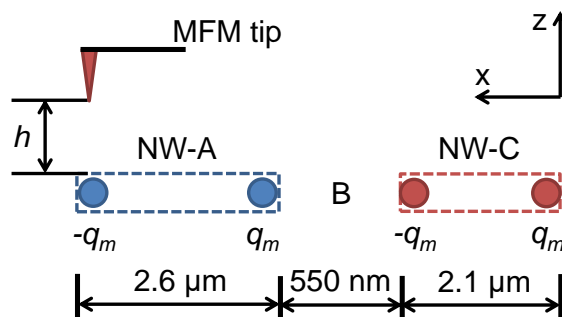


Figure 6-5. Schematic illustration of the simple magnetic dipole model, which is used to estimate the effective stray magnetic fields along the z-axis from the NW-A and NW-C at the tip height h for the MFM observations of the NWs.

The stray magnetic fields from the NWs at the tip height h during the MFM observations were roughly calculated using the simple magnetic dipole model, as illustrated in Fig. 6-5.

According to this simple model, the magnetic fields H from a magnetic charge is calculated as

$$H = \frac{q_m}{r^2} = \frac{M_s V}{l r^2} \quad (6-2)$$

where r is the height from a magnetic charge, q_m , to the MFM tip, V is the volume of NWs, which was roughly estimated from the length, width, and thickness of NWs observed in BSE images in Fig. 6-1, and l is the length of NWs. The effective stray magnetic fields parallel to the z-axis in Fig. 6-5 were calculated to be larger than 1000 Oe even at the tip height h of 30 nm during all the MFM observations in this study. The coercivity of the MFM tips used in this study is 950 Oe. (No other MFM tip with much higher coercivity is available at present.) The MFM tips could be exposed to the effective stray magnetic fields at the edges of NW-A and NW-C that are much higher than those at the tip height since the MFM tips scan the proximity of NW surfaces to obtain the surface morphology by AFM before each MFM scan during the observations. Therefore, the sudden changes in the contrasts at one of the ends of NW-A and NW-C under the applied magnetic fields of 3.0 kG or more, for example, in Fig. 6-4(b), were possibly due to the magnetization switching of MFM tips at the NW edges, although it was possible that the magnetization of NW-A and NW-C was actually switched at the applied magnetic fields of 3.0 kG or more. In our previous study related to different material systems, i.e., much smaller MnAs nanostructures, whose length and diameter were estimated to be approximately 74 and 92 nm, respectively, formed in vertical InAs NWs [37] than in the lateral MnAs NWs in this study, we have actually observed the magnetization switching in the small MnAs nanostructures in Ref. 36 since the effective stray magnetic fields parallel to the z-axis from such nanostructures dealt in Ref. 36 were calculated to be small enough to detect the magnetic switching in the nanostructures even at the tip height h of 30 nm during all the MFM observations. In the case of the applied external magnetic field of 2.0 kG, it was reasonable that no magnetization switching was observed in NW-A and NW-C since the applied magnetic field was smaller than the calculated coercivity of the

NWs in this study. This is possibly because the stray magnetic fields from the NWs at the applied external magnetic field of 2.0 kG are smaller than those at 3.0 kG or more. Therefore, no sudden changes in the contrasts at the ends of NW-A and NW-C were observed under the applied external magnetic field of 2.0 kG. In ferromagnetic materials, the magnetic properties, for example, T_c , coercivity, magnetization switching behaviors, and so on, depend on the crystal lattice strain in the materials [27–29]. However, as described above, the strain effects along any crystal orientations of the NWs, which are depicted in Fig. 6-1, were negligible in this study since the lateral MnAs NWs were possibly treated as a MnAs bulk crystal after the lattice relaxation. Even in the case of comparable MnAs nanostructures with a smaller width (or diameter) of approximately 180 nm in our previous studies, for example, in Ref. 31, it was indicated in the observed lattice image that the lattice strain could remain only in one or two monolayers of MnAs nanostructures at the interface between MnAs and AlGaAs. Therefore, it was presumed that the MnAs lattices along both <1-100> and <11-20> directions were completely relaxed in the lateral MnAs NWs since NW-A and NW-C had a width of 360 nm and a length larger than 2 μm , as shown in Fig. 6-2. As a result, no crystal lattice strain remained along the <0001> direction, c-axis, in the lattices. We believe that the analysis of magnetization switching based on the treatment of lateral MnAs NWs as a MnAs bulk crystal was reasonable in this study. The magnetization switching behaviors of lateral MnAs NWs were possibly similar to those of a MnAs bulk crystal. Although additional experiments are required to analyze various types of lateral NWs in detail, the results obtained in the current work in combination with the experimental results reported in our previous paper [16], in which the width of lateral NWs was key to controlling the number of magnetic domains in the <1-100> direction of the NWs [or the <-211> direction of the GaAs (111)B substrate], i.e., perpendicular to the NWs along the <11-20> direction [or the <0-11> direction of the substrate], suggest that magnetic domains and magnetizations are possibly tuned

by the structural control of the lateral NWs.

6.4 Conclusion

We demonstrated the structural and magnetic characterizations of lateral MnAs NWs formed by SA-MOVPE. The lateral MnAs NWs observed by BSE and secondary electron microscopy had a high aspect ratio (i.e., 2.6 μm long and 360 nm wide) and well-defined crystal facets. The external magnetic field dependence in the MFM observations of the lateral NWs revealed that single and multiple magnetic domains were formed parallel to the <11-20> direction of the lateral NWs, i.e., along the elongation direction of lateral NWs. These results obtained in this study suggest that magnetic domains are tuned by the structural control of lateral NWs. However, no magnetization switching was observed under the relatively high external magnetic field of 5.0 kG, which should be enough for the magnetization switching of the lateral NWs, possibly owing to the magnetization switching of the MFM tip itself used in this study during observations.

Bibliography

- [1] R. Horiguchi, H. Kato, K. Kabamoto, R. Kodaira, and S. Hara, Analyses of magnetization switching and magnetic domains in lateral MnAs nanowires in combination with structural characterization, *Jpn. J. Appl. Phys.* **56**, 06GH05 (2017).
- [2] S. S. P. Parkin, M. Hayashi, and L. Thomas, Magnetic domain-wall racetrack memory, *Science* **320**, 190 (2008).
- [3] M. Hayashi, L. Thomas, R. Moriya, A. Rettner, and S. S. P. Parkin, Current-Controlled Magnetic Domain-Wall Nanowire Shift Register, *Science* **320**, 209 (2008).
- [4] L. Thomas, S. H. Yang, K. S. Ryu, B. Hughes, C. Rettner, D. S. Wang, C. H. Tsai, K. H. Shen, and S. S. Parkin, Racetrack Memory: A high-performance, low-cost, non-volatile memory based on magnetic domain walls, *IEDM Tech. Dig.*, 2011, p. 535.
- [5] D. A. Allwood, G. Xiong, M. D. Cooke, C. C. Faulkner, D. Atkinson, N. Vernier, and R. P. Cowburn, Submicrometer Ferromagnetic NOT Gate and Shift Register, *Science* **296**, 2003 (2002).
- [6] M. Hayashi, L. Thomas, C. Rettner, R. Moriya, Y. B. Bazaliy, and S. S. P. Parkin, Current driven domain wall velocities exceeding the spin angular momentum transfer rate in permalloy nanowires, *Phys. Rev. Lett.* **98**, 037204 (2007).

- [7] A. Yamaguchi, T. Ono, S. Nasu, K. Miyake, K. Mibu, and T. Shinjo, Real-space observation of current-driven domain wall motion in submicron magnetic wires, *Phys. Rev. Lett.* **92**, 077205 (2004).
- [8] G. S. D. Beach, C. Knutson, C. Nistor, M. Tsoi, and J. L. Erskine, Nonlinear domain-wall velocity enhancement by spin-polarized electric current, *Phys. Rev. Lett.* **97**, 057203 (2006).
- [9] M. Tsoi, R.E. Fontana, and S. S. P. Parkin, Magnetic domain wall motion triggered by an electric current, *Appl. Phys. Lett.* **83**, 2617 (2003).
- [10] G. S. D. Beach, C. Nistor, C. Knutson, M. Tsoi, and J. L. Erskine, Dynamics of field-driven domain-wall propagation in ferromagnetic nanowires, *Nat. Mater.* **4**, 741 (2005).
- [11] J. Grollier, P. Boulenc, V. Cros, A. Hamzić, A. Vaures, A. Fert, and G. Faini, Switching a spin valve back and forth by current-induced domain wall motion, *Appl. Phys. Lett.* **83**, 509 (2003).
- [12] M. Yamanouchi, D. Chiba, F. Matsukura, and H. Ohno, Current-induced domain-wall switching in a ferromagnetic semiconductor structure, *Nature* **428**, 539 (2004).
- [13] S. Hara, D. Kawamura, H. Iguchi, J. Motohisa, and T. Fukui, Self-assembly and selective-area formation of ferromagnetic MnAs nanoclusters on lattice-mismatched semiconductor surfaces by MOVPE, *J. Cryst. Growth* **310**, 2390 (2008).

-
- [14] M. T. Elm and S. Hara, Transport properties of hybrids with ferromagnetic MnAs nanoclusters and their potential for new magnetoelectronic devices, *Adv. Mater.* **26**, 8079 (2014).
- [15] S. Sakita, S. Hara, M. T. Elm, and P. J. Klar, Selective-area growth and magnetic characterization of MnAs/AlGaAs nanoclusters on insulating Al₂O₃ layers crystallized on Si(111) substrates, *Appl. Phys. Lett.* **108**, 043108 (2016).
- [16] H. Kato, S. Sakita, and S. Hara, Selective-area growth and magnetic characterization of lateral MnAs nanowires, *J. Cryst. Growth* **414**, 151 (2015).
- [17] S. Ito, S. Hara, T. Wakatsuki, and T. Fukui, Magnetic domain characterizations of anisotropic-shaped MnAs nanoclusters position-controlled by selective-area metal-organic vapor phase epitaxy, *Appl. Phys. Lett.* **94**, 243117 (2009).
- [18] S. Hara and K. Komagata, Selective-area growth and magnetic reversals of ferromagnetic nanoclusters on semiconducting substrate for magnetic logic applications, *Phys. Status Solidi B* **252**, 1925 (2015).
- [19] M. T. Elm, P. J. Klar, S. Ito, S. Hara, and H.-A. Krug von Nidda, Effect of the cluster magnetization on the magnetotransport at low temperatures in ordered arrays of MnAs nanoclusters on (111)B GaAs, *Phys. Rev. B* **84**, 035309 (2011).
- [20] M. Fischer, M. T. Elm, S. Sakita, S. Hara, and P. J. Klar, Magnetoresistance effects and spin-

- valve like behavior of an arrangement of two MnAs nanoclusters, *Appl. Phys. Lett.* **106**, 032401 (2015).
- [21] M. Fischer, M. T. Elm, H. Kato, S. Sakita, S. Hara, and P. J. Klar, Analysis of magnetic random telegraph noise in individual arrangements of a small number of coupled MnAs nanoclusters, *Phys. Rev. B* **92**, 165306 (2015).
- [22] E. Sánchez, M. T. Deluigi, G. Castellano, Mean atomic number quantitative assessment in backscattered electron imaging, *Microsc. Microanal.* **18**, 1355 (2012).
- [23] K. Kanaya, S. Okayama, Penetration and energy-loss theory of electrons in solid targets, *J. Phys. D* **5**, 43 (1972).
- [24] T. Wakatsuki, S. Hara, S. Ito, D. Kawamura, and T. Fukui, Growth Direction Control of Ferromagnetic MnAs Grown by Selective-Area Metal–Organic Vapor Phase Epitaxy, *Jpn. J. Appl. Phys.* **48**, 04C137 (2009).
- [25] J. B. Goodenough and J. A. Kafalas, High-pressure study of the first-order phase transition in MnAs, *Phys. Rev.* **157**, 389 (1967).
- [26] F. Ishikawa, K. Koyama, K. Watanabe, and H. Wada, Field induced structural transformation in MnAs, *Jpn. J. Appl. Phys.* **42**, L918 (2003).
- [27] C. P. Bean and D. S. Rodbell, Magnetic disorder as a first-order phase transformation, *Phys.*

Rev. **126**, 104 (1962).

- [28] F. Iikawa, M. J. S. P. Brasil, C. Adriano, O. D. D. Couto, C. Giles, P. V. Santos, L. Däweritz, I. Rungger, and S. Sanvito, Lattice distortion effects on the magnetostructural phase transition of MnAs, Phys. Rev. Lett. **95**, 077203 (2005).
- [29] Q. Gan, R. A. Rao, C. B. Eom, J. L. Garrett, and M. Lee, Direct measurement of strain effects on magnetic and electrical properties of epitaxial SrRuO₃ thin films, Appl. Phys. Lett. **72**, 978 (1998).
- [30] S. Hara and T. Fukui, Hexagonal ferromagnetic MnAs nanocluster formation on GaInAs/InP (111)B layers by metal-organic vapor phase epitaxy, Appl. Phys. Lett. **89**, 113111 (2006).
- [31] M. T. Elm, C. Michel, J. Stehr, D. M. Hofmann, P. J. Klar, S. Ito, S. Hara, and H.-A. Krug von Nidda, Comparison of the magnetic properties of GaInAs/MnAs and GaAs/MnAs hybrids with random and ordered arrangements of MnAs nanoclusters, J. Appl. Phys. **107**, 013701 (2010).
- [32] K. Komagata, S. Hara, S. Ito, and T. Fukui, Ferromagnetic MnAs nanocluster composites position-controlled on GaAs (111) B substrates toward lateral magnetoresistive devices, Jpn. J. Appl. Phys. **50**, 06GH01 (2011).
- [33] E. C. Stoner and E. P. Wohlfarth, A Mechanism of Magnetic hysteresis in heterogenous alloys, Philos. Trans. R. Soc. London, Ser. A **240**, 599 (1948).

- [34] R. W. De Blois and D. S. Rodbell, Magnetic First-Order Phase Transition and Anisotropy in Single-Crystal MnAs, *J. Appl. Phys.* **34**, 1101 (1963).
- [35] R. W. De Blois and D. S. Rodbell, Magnetic first-order phase transition in single-crystal MnAs, *Phys. Rev.* **130**, 1347 (1963).
- [36] J. A. Osborn, Demagnetizing factors of the general ellipsoid, *Phys. Rev.* **67**, 351 (1945).
- [37] K. Kabamoto, R. Kodaira, and S. Hara, Magnetization in vertical MnAs/InAs heterojunction nanowires, *J. Cryst. Growth* **464**, 80 (2017).

Chapter 7

Conclusions

In this study, the structural and magnetic domain characterization and magnetization switching analysis of MnAs nanodisks (NDs) and lateral nanowires (NWs) selectively grown on Si (111) or GaAs (111)B substrates after AlGaAs buffer layer growth by selective-area metal-organic vapor phase epitaxy (SA-MOVPE) are discussed. We believe that the results on magnetization switching in MnAs nanostructures is crucial to realize the newly spintronics devices such as STS-MOSFET with the NDs on Si (111) substrates and/or our proposed planar-type magnetic logic devices consisting of elongated MnAs nanostructure composites selectively grown on GaAs (111)B substrates. Summary and conclusions are the following.

In chapter 4, we reported on SA-MOVPE and structural characterization results of magnetic MnAs NDs after the AlGaAs NP buffer growth on Si (111) substrates using multiple types of mask materials and designs, which were mask patterns (I) and (II) of SiO₂ and SiON removing (I) the mask materials outside $100 \times 100 \mu\text{m}^2$ square regions with periodical circular openings and (II) only the periodical circular openings within the $100 \times 100 \mu\text{m}^2$ square regions.. The results of structural characterizations showed that two key issues, which were the unintentional growth of MnSi alloy in Si substrates and MnAs alloy with approximately 17% of Si atoms on NDs, were typically observed in the case of Si substrates with mask pattern (I) of SiO₂. On the other hand, these two key issues are not observed in the case of Si substrates with

mask pattern (II) of SiON. These results suggested that mask pattern (II) of SiON was effective to prevent the unintentional reactions of Mn atoms with Si substrates for growing MnAs NDs with a high degree of uniformity.

In chapter 5, we characterized magnetic domain and domain wall structures of MnAs NDs on AlGaAs nano pillar buffers selectively grown on Si (111) substrates partially covered with dielectric SiO_2 thin film mask patterns for SA-MOVPE. The results on the size dependence of magnetic domain structures in MnAs NDs observed by MFM showed that a single domain was predominant in the MnAs NDs with an area of approximately $4 \times 10^4 \text{ nm}^2$ or less. It was also indicated that multiple domains, in particular, the two magnetic domain structures with a 180° domain wall were predominant in the NDs with an area of approximately $6 \times 10^4 \text{ nm}^2$ or more. In addition, in the case of NDs with multiple domains, the NDs not only with Néel wall but also with Bloch wall were possibly formed, judging from the detailed analyses of the MFM images obtained. Moreover, we characterized the applied external magnetic field, \mathbf{B} , dependence of a magnetic domain of MnAs NDs. From the results on the \mathbf{B} dependence of a magnetic domain structure in the MnAs NDs, the ratio of a single magnetic domain was minimized at $\mathbf{B} = -1.5 \text{ kG}$ in the NDs with an area of $4 \times 10^4 \text{ nm}^2$ or smaller, although the decrease to the minimum of the ratio was markedly small in the case of the NDs with an area of $4 \times 10^4 \text{ nm}^2$ or larger at $\mathbf{B} = -0.5 \text{ kG}$. In addition, the angle distribution of magnetization directions showed that the magnetization directions were mostly parallel to the ridge directions of the hexagonal NDs, i.e., distributed in steps of approximately 60 degrees corresponding to the magnetic easy axes of the hexagonal NiAs-type crystal structure. These results suggested that the magnetic domains and a coercive force can be tuned by controlling the MnAs ND size.

In chapter 6, we demonstrated the structural and magnetic characterizations of lateral MnAs NWs formed by SA-MOVPE. The lateral MnAs NWs observed by BSE and secondary electron microscopy had a high aspect ratio (i.e., 2.6 μm long and 360 nm wide) and well-defined crystal facets. The external magnetic field dependence in the MFM observations of the lateral NWs revealed that single and multiple magnetic domains were formed parallel to the <11-20> direction of the lateral NWs, i.e., along the elongation direction of lateral NWs. These results obtained in this study suggest that magnetic domains are tuned by the structural control of lateral NWs. However, no magnetization switching was observed under the relatively high external magnetic field of 5.0 kG, which should be enough for the magnetization switching of the lateral NWs, possibly owing to the magnetization switching of the MFM tip itself used in this study during observations.

List of Publications-Conferences

1. Publication related to this work

- [1] R. Horiguchi, H. Kato, K. Kabamoto, R. Kodaira, and S. Hara, “Analyses of magnetization switching and magnetic domains in lateral MnAs nanowires in combination with structural characterization”, Japan Journal of Applied Physics, Vol. 56, No. 6S1, pp. 06GH05-1-06GH05-6 (2017). (IF=1.376, TC=1)
- [2] R. Horiguchi, S. Hara, and M. Iida, “Magnetic Domain Structure and Domain Wall Analysis of Ferromagnetic MnAs Nanodisks Selectively-grown on Si (111) Substrates for Spintronic Applications”, Journal of Applied Physics, Vol. 124, No. 15, pp. 153905-1-153905-7 (2018). (IF=2.286, TC=1)
- [3] R. Horiguchi, S. Hara, M. Iida, and K. Morita, “Selective-area Growth of Magnetic MnAs Nanodisks on Si (111) Substrates using Multiple Types of Dielectric Masks”, Journal of Crystal Growth, Vol. 507, pp. 226-231 (2019). (IF=1.632, TC=0)
- [4] R. Horiguchi, S. Hara, K. Suzuki, and M. Iida, “Magnetization switching depending on magnetic fields applied to ferromagnetic MnAs nanodisks selectively-grown on Si (111)

Substrates”, AIP Advances, Vol. 10, No. 12, pp. 125003-1-125003-7 (2020). (IF=1.337, TC=0)

2. Publication relate to other works

- [1] R. Kodaira, R. Horiguchi, and S. Hara, “Magnetization characterization of MnAs nanoclusters at close range in bended MnAs/InAs heterojunction nanowires”, Journal of Crystal Growth, Vol. 507, pp. 241-245 (2019). (IF=1.632, TC=3)
- [2] P. Uredat, R. Kodaira, R. Horiguchi, S. Hara, A. Beyer, K. Volz, M. T. Elm, P. J. Klar and M. T. Elm, “Anomalous Angle-Dependent Magnetotransport Properties of Single InAs Nanowires”, Nano Letters, Vol. 20, No. 1, 618-624 (2019). (IF=11.238, TC=1)
- [3] P. Uredat, M. T. Elm, R. Horiguchi, P. J. Klar and S. Hara, “The transport properties of InAs nanowires: an introduction to MnAs/InAs heterojunction nanowires for spintronics”, Journal of Physics D: Applied Physics, Vol. 53, No. 33, 333002-1-333002-22 (2020). (IF=3.169, TC=0)

3. Presentations related to this work

International conference

- [1] R. Horiguchi, H. Kato, K. Kabamoto, R. Kodaira, and S. Hara, “Structural and Magnetic Domain Characterization of Lateral MnAs Nanowires”, the 29th International Microprocesses and Nanotechnology Conference (MNC 2016), Kyoto, Japan, November 8-11, 2016, 11B-10-3.
- [2] R. Horiguchi, M.Iida, K. Morita, and S. Hara, “Size-Dependent Magnetic Domain Structure in MnAs Nanoclusters Selectively Grown on Si (111) Substrates Covered with Different Dielectric Mask Designs”, the 2017 Material Research Society (MRS) Fall Meeting, Boston, Massachusetts, USA, November 26-December 1, 2017, EM08.06.04.
- [3] R. Horiguchi, M. Iida, K. Morita, and S. Hara, “Analyses of Magnetic Domains in MnAs Nanoclusters Grown by Selective-Area MOVPE”, the 19th International Conference on Metalorganic Vapor Phase Epitaxy (ICMOVPE-XIX), Nara, Japan, June 3-8, 2018, 5B-3.6.

Domestic conference

- [1] 堀口 竜麻, 加藤 弘晃, 植木 恒平, 小平 竜太郎, 原 真二郎, 「横型 MnAs ナノワイヤの構造評価および磁区観察」, 第 77 回応用物理学会秋季学術講演会, 新潟, 2016 年 9 月 14p-D62-8.

- [2] 堀口 竜麻, 飯田 勝也, 森田 浩平, 原 真二郎, 「Si 上に SA-MOVPE 成長した MnAs ナノクラスタにおける磁区構造のサイズ依存性」, 第 78 回応用物理学会秋季学術講演会, 福岡, 2017 年 9 月, 6p-S44-3.
- [3] 堀口 竜麻, 飯田 勝也, 森田 浩平, 原 真二郎, 「Si 上に選択成長した MnAs ナノクラスタの磁区及び磁壁評価」, 第 53 回応用物理学会北海道支部学術講演会, 北海道, 2018 年 1 月 A-18.

4. Presentations related to other works

International conference

- [1] M. T. Elm, R. Kodaira, R. Horiguchi, K. Kabamoto, P. J. Klar, and S. Hara, “Structural Characterization and Magnetotransport Properties of MnAs/InAs Hybrid Nanowires Grown by Selective-Area Metal-Organic Vapor Phase Epitaxy”, the 2016 Material Research Society (MRS) Fall Meeting, Boston, Massachusetts, USA, November 27-December 2, 2016, NM1.2.02.
- [2] P. Uredat, M. T. Elm, R. Kodaira, R. Horiguchi, P. J. Klar, and S. Hara, “Electrical Transport Property of Single MnAs/InAs Hybrid Nanowires Grown by Selective-Area Vapor Phase Epitaxy”, the 2017 Material Research Society (MRS) Fall Meeting, Boston, Massachusetts, USA, November 26-December 1, 2017, NM03. 07. 06.
- [3] M. Iida, R. Horiguchi, K. Morita, and S. Hara, “Magnetic Domain Characterizations of MnAs

Nanoclusters on Si (111) Substrate”, the 2017 International Conference on Solid State Devices and Material (SSDM 2017), Sendai, Japan, September 19-22, 2017, PS -8 -02.

- [4] R. Kodaira, R. Horiguchi, and S. Hara, “Magnetization Characterization of Two MnAs Nanoclusters at Close Range in MnAs/InAs Heterojunction Nanowires”, the 19th International Conference on Metalorganic Vapor Phase Epitaxy (ICMOVPE-XIX), Nara, Japan, June 3-8, 2018, 7C-3.6.
- [5] P. Uredat, R. Kodaira, R. Horiguchi, S. Hara, P. J. Klar, and M. T. Elm, “Determining the Carrier Mobility in Single InAs Nanowires from Magnetotransport Measurements”, the 2018 International Conference on Solid State Devices and Materials (SSDM 2018), Tokyo, Japan, September 9-13, 2018, M-6-02.
- [6] Y. Kitazawa, R.Kodaira, R. Horiguchi, W. Jevasuwan, N. Fukata, and S. Hara, “Dependence of Si Nanowire Orientation on Vapor-Liquid-Solid Growth Conditions”, The 31st International Microprocesses and Nanotechnology Conference (MNC 2018), Sapporo, Japan, November 13-16, 2018, 16P-11-111L.
- [7] K. Suzuki, R. Horiguchi, M. Iida, and S. Hara, “Domain structures Depending on Applied Magnetic Fields in MnAs Nanodisks Selectively-grown on Si (111) substrates” The 31st International Microprocesses and Nanotechnology Conference (MNC 2018), Sapporo, Japan, November 13-16, 2018, 16P-11-116L.
- [8] K. Teramoto, R. Horiguchi, Y. Adachi, M. Akabori, S. Hara, “Applied External Magnetic Fields

Dependence of Magnetic Domain Structures in Patterned CoFe Thin Films on GaAs (001) Substrates”, The 32nd International Micropocesses and Nanotechnology Conference (MNC 2019), Hiroshima, Japan, October 28-31, 2019, 31C-8-1.

- [9] K. Teramoto, R. Horiguchi, Y. Adachi, M. Akabori, S. Hara, “Thickness and Aspect Ratio Dependence of Magnetic Domain Structures in Patterned CoFe Thin Films on GaAs (001) Substrates”, the 2019 International Conference on Solid State Devices and Materials (SSDM 2019), Aichi, Japan, September 2-5, 2019, PS-8-20.
- [10] R. Horiguchi, K. Teramoto, Y. Adachi, M. Akabori, and S. Hara, “Aspect Ratio Dependence of Magnetic Switching in CoFe Nanolayers Patterned on GaAs (001) Substrates”, the 8th International Symposium on Control of Semiconductor Interfaces (ISCSI-VIII), Sendai, Japan, November 27-30, 2019, WP2-20.
- [11] W. Dai, K. Teramoto, R. Horiguchi, W. Kanetsuka, M. Akabori, and S. Hara, “Magnetic Domain Structures Controlled by Patterned CoFe Nanolayer Thickness on GaAs (001) Substrates”, the 2020 International Conference on Solid State Devices and Materials (SSDM 2020), All-Virtual Conference, September 27-30, 2020, H-4-05.
- [12] W. Dai, K. Teramoto, R. Horiguchi, W. Kanetsuka, M. Akabori, S. Hara, “Applied External Magnetic Fields Dependence of Magnetic Domain Structures in Patterned CoFe Thin Films on GaAs (001) Substrates”, The 33rd International Micropocesses and Nanotechnology Conference (MNC 2020), Online Conference, November 9-12, 2020, 2020-22-10.

Domestic conference

- [1] M. T. Elm, R. Kodaira, R. Horiguchi, K. Kabamoto, S. Hara, and P. J. Klar, “Transport Properties of Ferromagnetic-Semiconducting Hybrid Nanowires with Well-Defined MnAs Nanocluster Properties”, the 2017 German Physical Society (DPG) Spring Meeting (Dresden 2017), Dresden, Germany, March 19-24, 2017, HL69.1.
- [2] 小平 竜太郎, 堀口 竜麻, P. Uredat, M. T. Elm, P. J. Klar, 原 真二郎, 「Magnetotransport Properties of Single InAs Nanowires」, 第 78 回応用物理学会秋季学術講演会, 福岡, 2017 年 9 月, 7a-S44-6.
- [3] P. Uredat, R. Kodaira, R. Horiguchi, S. Hara, P. J. Klar, and M. T. Elm, “Magnetotransport Measurements of Single MnAs/InAs Hybrid Nanowire”, the 2018 German Physical Society (DPG) Spring Meeting (Berlin 2018), Berlin, Germany, March 11-16, 2018, HL19.3.
- [4] 小平 竜太郎, 堀口 竜麻, 原 真二郎, 「屈曲した MnAs/InAs ヘテロ接合ナノワイヤの磁気特性および構造評価」, 第 65 回応用物理学会春季学術講演会, 東京, 2018 年 3 月, 19p-P8-1.
- [5] 鈴木 洋三郎, 堀口 竜麻, 飯田 勝也, 原 真二郎, 「Si 基板上に選択成長した MnAs ナノディスクにおける磁区構造の磁場依存性」, 第 79 回応用物理学会秋季学術講演会, 愛知, 2018 年 9 月, 20p-PB2-9.

-
- [6] 北澤 佑記, 小平 竜太郎, 堀口 竜麻, 原 真二郎, 「VLS 法により成長した Si ナノワイヤの構造評価」, 第 66 回応用物理学会春季学術講演会, 東京, 2019 年 3 月, 10p-PA1-5.
- [7] 寺本 圭吾, 堀口 竜麻, 足立 裕介, 赤堀 誠志, 原 真二郎, 「GaAs (001)基板上に形成した CoFe 薄膜パターニングの磁区観察」, 第 80 回応用物理学会秋季学術講演会, 北海道, 2019 年 9 月, 19p-E317-5.
- [8] 堀口 竜麻, 寺本 圭吾, 足立 裕介, 赤堀 誠志, 原 真二郎, 「GaAs (001)基板上に形成した CoFe ナノレイヤパターニングにおけるスイッチング磁場の膜厚依存性」, 第 67 回応用物理学会春季学術講演会, 東京, 2020 年 3 月.